REPORT DOCUMENTATION PAGE

Form Approved
OMB NO. 0704-0188

1. AGENCY USE ONLY (Leave Blank)	2. REPORT DATE 25 July 2002	3. REPORT TYPE AND DATES COVERED
		Final Report 1 May 1988 – 30 April 2002

4. TITLE AND SUBTITLE
Aerodynamics of Parachute Opening

5. FUNDING NUMBERS
Grant No. DAAG55-98-1-0171

6. AUTHOR(S)
H. Johari and K.J. Desabrais

7. PERFORMING ORGANIZATION NAME(S) AND ADDRESS(ES)
Worcester Polytechnic Institute – Mechanical Engineering Department
100 Institute Road
Worcester, MA 01609

8. PERFORMING ORGANIZATION REPORT NUMBER

9. SPONSORING / MONITORING AGENCY NAME(S) AND ADDRESS(ES)

U. S. Army Research Office
P.O. Box 12211
Research Triangle Park, NC 27709-2211

10. SPONSORING / MONITORING AGENCY REPORT NUMBER

37594.6-EG

12 a. DISTRIBUTION / AVAILABILITY STATEMENT

Approved for public release; distribution unlimited.

12 b. DISTRIBUTION CODE

13. ABSTRACT (Maximum 200 words)

The velocity field in the near wake of a small-scale, flexible, flat circular parachute canopy was measured by the particle image velocimetry method. The experiments were performed in a water tunnel with the Reynolds number ranging from $3.0 - 6.0 \times 10^4$. Both a fully inflated canopy and the inflation phase were investigated. The fully inflated canopy experienced a cyclic "breathing" motion with a normalized frequency of 0.56 ± 0.03, which corresponded to the shedding of vortex rings from the canopy. The boundary layer formed on the canopy surface begins to separate near the apex region when the diameter is approximately 68% of the fully inflated diameter. Then, drag rapidly increases to its maximum value while the separation point of the boundary layer moves upstream towards the skirt. Drag declines rapidly afterwards and the separated boundary layer rolls-up into a vortex ring near the canopy skirt. The majority of the opening force was the result of the time rate of change of the impulse, which accounts for approximately 60% of the peak opening force.

14. SUBJECT TERMS
parachute inflation, canopy near wake velocity field, hydrodynamic impulse

15. NUMBER OF PAGES
130

16. PRICE CODE

17. SECURITY CLASSIFICATION OR REPORT **UNCLASSIFIED**	18. SECURITY CLASSIFICATION ON THIS PAGE **UNCLASSIFIED**	19. SECURITY CLASSIFICATION OF ABSTRACT **UNCLASSIFIED**	20. LIMITATION OF ABSTRACT **UL**

NSN 7540-01-280-5500

Standard Form 298 (Rev.2-89)
Prescribed by ANSI Std. 239-18
298-102

20030310 028
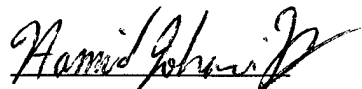
FINAL PROGRESS REPORT

AERODYNAMICS OF PARACHUTE OPENING

submitted to

by

Hamid Johari

Hamid Johari
Mechanical Engineering Department
Worcester polytechnic Institute
Worcester, MA 01609

July 2002

Summary

The velocity field in the near wake of a small-scale, flexible, flat circular parachute canopy was measured by the particle image velocimetry method. The experiments were performed in a water tunnel with the Reynolds number ranging from $3.0 - 6.0 \times 10^4$. Both a fully inflated canopy and the inflation phase were investigated. The fully inflated canopy experienced a cyclic "breathing" with a normalized frequency of 0.56 ± 0.03, which corresponded to the shedding of vortex rings from the canopy. During the early stages of the inflation, the boundary layer remains attached to the canopy while the canopy diameter increases substantially. The boundary layer begins to separate near the apex region when the diameter is approximately 68% of the fully inflated diameter. At this point, the force rapidly increases to its maximum value while the separation point of the boundary layer moves upstream towards the skirt. The force then declines rapidly and the separated boundary layer rolls-up into a vortex ring near the canopy skirt. At the same time, the canopy is drawn into an over-expanded state after which the cyclic breathing initiates. The unsteady potential force was estimated from the rate of change of the canopy volume. It is less than 10% of the peak opening force and was only significant during the early stages of inflation. The majority of the opening force was the result of the time rate of change of the impulse, which accounts for approximately 60% of the peak opening force. This result shows that the formation of the viscous wake is the primary factor in the development of the peak drag force.

Table of Contents

Nomenclature

A_i	imaged area
C_D	canopy drag coefficient
C_{Du}	uncorrected drag coefficient
C_F	force coefficient
D_m	maximum projected diameter
D_o	canopy constructed diameter
D_p	mean projected diameter during steady descent
D'_{rms}	*rms*-value of the canopy diameter oscillations
D_{t2}	canopy diameter at time $t = t_2$
D_{t3}	canopy diameter at time $t = t_3$
D_v	vent hole diameter
Δt	time separation between laser pulses
F	canopy force
$\overline{F}$	mean canopy force
F'_{rms}	*rms*-value of the canopy force
F_p	canopy force due to the unsteady potential flow
$(F_p)_{rms}$	*rms*-value of the canopy force due to the unsteady potential flow
F_ω	canopy force due to vorticity
g	gravity
H	canopy height
$\mathbf{I}$	unit tensor
k_p	proportionality constant for potential flow
K_M	blockage factor
l_s	suspension line length
m_a	apparent mass
m_i	mass of fluid enclosed by the parachute canopy
m_p	mass of parachute canopy
m_s	mass of the suspend payload
$\hat{n}$	outward normal

q_o	dynamic pressure
q_{ou}	uncorrected dynamic pressure
r	radial distance
Re_{Do}	Reynolds number based on constructed diameter ($U_\infty D_o/\nu$)
s	path of integration
S	canopy area
S_o	surface area of canopy (*i.e.* $\pi D_o^2/4$)
S_p	projected area of canopy
S_T	cross-sectional area of tunnel test section
St	Strouhal number
$\mathbf{T}$	traction tensor
t	time
t_2	time when boundary layer first separates from canopy
t_3	time when boundary layer separates from canopy skirt
t_f	filling time
t_f^*	normalized filling time ($t_f U_\infty/D_o$)
t_{max}	time at maximum diameter
t_{max}^*	normalized t_{max} ($t_{max} U_\infty/D_o$)
t_o	opening time
t_o^*	normalized opening time ($t_o U_\infty/D_o$)
U_∞	freestream velocity
$\vec{u}$	velocity vector
$\vec{u}_s$	surface velocity
u	system velocity
u_c	vortex celerity
u_r	radial velocity of fluid
u_z	axial velocity of fluid
U'_{rms}	*rms*-value of freestream velocity fluctuations
u_{ti}	tangential velocity component at an interior canopy position
u_{tr}	tangential velocity component at a reflected interior canopy position

u_{ni}	normal velocity component at an interior canopy position
u_{nr}	normal velocity component at a reflected interior canopy position
V	volume enclosed by canopy
V_{steady}	volume enclosed by canopy at steady descent
$\dot{V}$	rate of change of enclosed canopy volume (dV/dt).
$\bar{V}$	mean canopy volume in steady descent
V'	volume fluctuations in steady descent
$(\dot{V}')_{rms}$	rms-value of the time rate of change of the volume fluctuations
$\vec{x}$	position vector

Greek Symbols

α_{fb}	forebody wake correction factor
ε^{sb}	solid blockage
Γ	circulation
ρ	fluid density
$\rho_{x,y}$	correlation coefficient
τ	normalized time (t/t_o)
τ_2	normalized separation time for stage II (t_2/t_o)
τ_3	normalized separation time for stage III (t_3/t_o)
ν	kinematic viscosity
$\vec{\omega}$	vorticity ($\nabla \times \vec{u}$)
ω_θ	azimuthal component of vorticity

1. Introduction

1.1 Literature Review

The kinematics and dynamics of a parachute system incorporate many facets of the engineering field from the fluid dynamics of the canopy to the structural mechanics of the suspension lines and the devices used to attach the payload to the parachute. The flow physics around the canopy is perhaps one of the least understood components of the parachute system. For instance, the connection between the large opening force (*i.e.*, the opening shock) and the fluid kinematics that produce it has not been extensively examined. What flow field features contribute to the opening force? Does the force come primarily from the outward fluid acceleration due to the increasing canopy size (an added mass effect) or are viscous wake effects responsible? Similar questions can be posed about the dominant shedding frequency affecting the breathing of a fully inflated canopy during steady descent. The goal of this research project was to enhance the understanding of the flow physics in the near wake of a parachute canopy.

G.I. Taylor performed early experiments on the use of a parachute as a brake to shorten the landing distance of an aircraft in 1915 that expanded into a study of the shape of a parachute canopy (Taylor, 1963). Müller (1927) proposed an inflation process based on the enclosed volume of the parachute using the theory of the conservation of mass. He concluded that the parachute inflated in a constant distance for geometrically similar canopies (*i.e.* canopies that have similar geometric construction). This leads directly to the concept of an inflation time for a given speed and parachute. Since then many theories have been developed based on opening or filling times (O'Hara, 1949; French, 1963; Heinrich, 1969; Heinrich & Noreen, 1970; Heinrich, 1972; Payne, 1973). These

1

theories do not rely on the details of the flow around the canopies, merely the time it takes the canopy to inflate. Various ad hoc assumptions about the canopy shape and the inlet/outlet conditions are made.

To estimate the load and trajectory of parachute systems, Newton's second law is utilized (Heinrich, 1969),

$$m_s \frac{du}{dt} = m_s g - \frac{1}{2} \rho C_D S u^2 - u \left(\frac{dm_i}{dt} + \frac{dm_a}{dt} \right) - \left(m_p + m_i + m_a \right) \frac{du}{dt} \qquad 1.1$$

where m_s is the mass of the suspended payload, m_i is the fluid mass enclosed (included) by the canopy, m_p is the canopy mass, m_a is the apparent mass, u is the system velocity, C_D is the canopy drag coefficient, S is the canopy area, and ρ is the fluid density. The two unsteady inertia terms are the included mass and the apparent mass. Each of these unsteady inertia terms is proportional to the volume enclosed by the canopy,

$$u \frac{dm}{dt} \propto \rho u \dot{V} \qquad 1.2$$

where $\dot{V}$ is the time derivative of the enclosed volume. In the included mass, the proportionality constant is unity (by definition). The proportionality constant for the apparent mass depends on the geometry of the canopy. The apparent mass (or the virtual mass) is based on the inviscid potential flow around the canopy. The model in Eq. 1.1 then requires any viscous effects to be accounted for in the u^2 drag coefficient term. In parachute system analysis, however, it has traditionally been assumed that the drag coefficient (derived from experimental data) is constant. Any transient behavior is therefore associated with the rate of change of the unsteady inertia terms and the deceleration of the system.

A parachute can inflate under two limiting conditions, either a finite or an infinite mass condition. During a finite mass inflation, the velocity of the system decays as the parachute inflates. On the other hand, during an infinite mass inflation, the velocity does not decay significantly during the inflation; the parachute behaves as if an infinite mass is attached to the parachute. This implies that under an infinite mass inflation or while the parachute is in steady descent, the last term listed in Eq. 1.1 can be neglected since $du/dt = 0$. Then, during an infinite mass inflation, this model results in any unsteadiness to be associated with the time rate of change of the inertia terms (*i.e.* the rate of change of the enclosed canopy volume) if C_D is assumed constant.

A number of attempts have been made to estimate the apparent mass of the flow around the canopy during inflation (Ibrahim, 1967; Eaton, 1983; Yavuz, 1989). Past work on apparent mass has dealt with a rigid canopy and the unsteadiness is associated only with the deceleration of the canopy. The enclosed canopy volume does not change in these works. These models oversimplify the complex fluid dynamics and kinematics of the parachute inflation process. From a parachute designers standpoint, these simplification are justified for the prediction of the parameters such as inflation time and the maximum opening forces. The past research has primarily focused on obtaining these parameters from analytical theories combined experimental data (French, 1964; Knacke, 1992; Wolf, 1999). The existing theories provide reasonable results for well-known canopy geometries and conditions but have limited success with a generic parachute canopy. However, from an aerodynamic viewpoint, these simplifications and theories obscure the flow physics that drive the canopy inflation process.

The limitations of the inflation time theories was recognized by Müller (1927) when he acknowledged the flow around the canopy was turbulent and separated but he applied simplifying assumption to eliminate such difficulties. Studies and mathematical models for parachutes systems have been developed which acknowledge and account for the unsteady flow conditions that the canopy encounters during inflation (Wolf, 1974; McVey & Wolf, 1974; Purvis, 1982) but still do not provide much insight into the details of the flow field around the canopy itself.

In early numerical work, the canopy inflation has been modeled by replacing the canopy surface with a vortex sheet (Klimas, 1972, 1977, 1979; Reddy, 1974). In another modeling effort, a starting vortex was placed near the canopy skirt and the flow field was allowed to develop (Roberts, 1974). In more recent numerical studies, the power of massively parallel computers has been employed. A review of some of the methods used for numerically calculating the canopy inflation process and bluff body flows in general was given by Peterson *et al.* (1996). Recently, computational algorithms have been developed to solve the three-dimensional Navier-Stokes equations with fluid-structure interaction between the canopy and the surrounding fluid (Stein, 1999; Stein *et al.*, 1999; Stein *et al.*, 2000). These computational models are currently limited to only modeling a fully inflated parachute canopy. Additionally, the structural dynamics of the canopy material in the flow field has also been modeled (Accorsi *et al.*, 1999). However, almost no experimental data exists to verify the fidelity of either the structural or fluid dynamic simulations.

Few experimental studies have been performed that specifically measure flow field parameters around a parachute canopy either during inflation or once it has reached

4

a steady state condition. DeSantis (1970) measured the flow entering and in the wake of an inflating canopy using a hot-wire probe at a few cross-sectional planes. Klimas (1973) and Klimas & Rogers (1977) measured the velocity field of an inflating canopy using a helium bubble survey which provided mean iso-velocity contours around the canopy. The measurement of the pressure distribution of a fully inflated parachute canopy was conducted by Pepper & Reed (1976) in which they showed the integrated pressure provided a reasonable estimate of the drag force. The only other known measurement of the velocity field around an inflating parachute model was conducted by Lingard (1978). He was able to measure several tens of velocity vectors around an inflating small scale parachute model in both a water tow tank and a wind tunnel. The limited resolution of the measurements however precluded computations of the vorticity or the integrated measures of the flow such as circulation or impulse.

A study of the flow past a slotted bluff body model in a constant freestream was performed by Higuchi (1989) that showed the effects of the porosity on the overall wake characteristics. Studies of the wakes around rigid three-dimensional bluff bodies that at least qualitatively should behave similarly to parachutes (disks and cups) in steady and accelerating flows have been performed to understand the unsteady flow field around these bodies (Roberts, 1980; Higuchi, 1991; Higuchi *et al.*, 1996; Higuchi *et al.*, 1996; Lamberson *et al.*, 1999). The rigid nature of these bodies limit the applicability of these flows to the flow around a flexible parachute canopy.

1.2 Objectives

The objectives of this research are to investigate the fluid dynamics in the near wake of a flexible parachute canopy. A review of the available literature shows that knowledge of the flow field evolution around a canopy is limited. The primary goals of the study are:

- To measure the temporal evolution of the velocity field (and by extension the vorticity field) in the near wake of a flexible canopy both during inflation and once the canopy is fully inflated,

- To obtain simultaneous measurements of the canopy shape and drag that are synchronized with the velocity field measurements,

- To identify any features of the flow field that affect the behavior of the canopy both during the inflation of the canopy (particularly around the time of the peak opening force) and once it is fully inflated, and

- To examine whether the primary source of the drag force is the result of an unsteady potential flow (*i.e.*, an apparent mass term due to the change in the enclosed canopy volume) or the formation of a turbulent wake behind the canopy.

To accomplish these objectives, small-scale parachute canopies were constructed for testing in the WPI water tunnel facilities. The particle image velocimetry technique along with image processing routines is used to measure the evolving velocity field in the near wake region of the inflating canopy models. From these measurements, the connection between the flow field and the canopy dynamics and motion are examined.

1.3 Full-Scale Parachute Inflation

The inflation of a full-scale parachute develops in a few stages. Inflation of a 64-ft. round full-scale canopy is shown in Fig. 1.1. Initially, the cargo is released from the aircraft with the main parachute packed into a deployment bag. Attached to the deployment bag is a small parachute (usually called a drogue chute) that pulls the deployment bag off the main parachute canopy. The process of the drogue chute extracting the main parachute is shown in the first four images of Fig. 1.1. Once the deployment bag has been removed, the main parachute resembles a collapsed sock or hose. Air begins to enter the mouth or skirt area of the parachute causing the entrance region of the canopy to form into a cylindrical shape while the upper or crown region of the canopy remains in a collapsed state. The air being forced into the canopy mouth causes the canopy material to expand into a cylindrical shape along the whole length of the canopy with the crown region having a hemi-spherical shape. At this point, air begins to collect at the apex region of the canopy causing the canopy material to bulge while the skirt region remains collapsed in a cylindrical shape. The maximum diameter of the inflating canopy is in the bulging region of the canopy. The air continues to accumulate in the apex region of the canopy further increasing the size of the bulge in both axial and transverse directions.

The axial expansion of the bulge starts from the apex region of the canopy and moves towards the canopy skirt. The canopy continues to expand or inflate until it reaches its fully inflated size (the last two images in Fig. 1.1) and the maximum canopy diameter is realized at the skirt. The canopy diameter however continues to grow beyond this point into an over-expanded state (not shown in Fig. 1.1). In the over-expanded state,

7

the canopy achieves its maximum diameter and the canopy apex region becomes partially collapsed or buckled as the canopy skirt is drawn out into the over-expanded state.

After the over-expansion, the canopy size decreases to a shape similar to that seen in the last frame of Fig. 1.1. By this time, the canopy has reached its steady descent mode and the parachute system develops new oscillation modes. These modes could include a symmetric breathing of the canopy itself and a helical oscillation of the entire parachute system around a common axis. The whole inflation process occurs in a time span of a few seconds.

A graph of the opening force that a full-scale parachute experiences during the inflation is shown in Fig. 1.2. It should be noted that the force shown in Fig. 1.2 does not correspond to the images in Fig. 1.1. The force initially begins with a short sharp spike when the drogue chute pulls the canopy from the deployment bag and the suspension lines on the canopy become taunt. The force then drops until the canopy begins to inflate. The force rapidly rises to its maximum value and then it declines to its steady descent drag value. The connection between the canopy shape and size and the force depends on whether the canopy inflates in a finite or infinite mass condition (Knacke, 1992). Recall during a finite mass inflation, the velocity of the parachute system decays as the parachute inflates. In this case, the canopy achieves its fully inflated shape (but has not yet over-expanded) at a time well after the peak opening force has occurred. In an infinite mass parachute inflation, the canopy diameter first becomes equal to the mean steady state diameter at approximately the same time the peak opening force occurs. It should not be assumed that an infinite mass inflation is strictly a research topic, there are many examples of infinite mass inflations in real applications. Parachutes are often used

8

as a stabilizing component on payloads. These parachutes are opened at high speeds and help orientate the payload in a certain direction before larger parachutes are deployed which actually decelerate the payload. For example, planetary probes released from orbit often have small parachutes that deploy high in the atmosphere of the planet that act to stabilize the payload before larger parachutes are deployed lower in the atmosphere that decelerate the payload. Also, often extraction parachutes are used to pull payloads out of an aircraft. These extraction chutes open at the speed of the aircraft which remains constant and therefore the parachute inflates under an infinite mass condition.

1.4 Fluid Dynamic Forces

Lighthill (1986) has suggested that the force a body experiences in a fluid flow can be decomposed into a vortical and an inviscid (potential) component. He further hypothesized that the vortical component is proportional to the time derivative of the flow impulse over the entire wake. An *exact* expression for obtaining the instantaneous fluid force exerted on a body was developed by Noca *et al.* (1999). This expression requires knowledge of only the velocity field (and extension the vorticity field) in a finite region around the body. No knowledge of the pressure field is necessary. This is particularly useful in this research since pressure field is particularly difficult to measure in unsteady flows. The aerodynamic force on a body with an arbitrary shape, using the control volume shown in Fig. 1.3, is

$$\frac{\vec{F}}{\rho} = -\frac{1}{N-1}\frac{d}{dt}\iiint_{V_f(t)} \vec{x}\times\vec{\omega}\,dV + \frac{1}{N-1}\frac{d}{dt}\oint_{S_b(t)} \vec{x}\times(\hat{n}\times\vec{u})dS$$

$$-\oint_{S_b(t)} \hat{n}\cdot(\vec{u}-\vec{u}_s)\vec{u}dS + \oint_{S_f(t)} \hat{n}\cdot\vec{\gamma}\,dS \qquad 1.3$$

9

where

$$\vec{\gamma} = \frac{1}{2}u^2\mathbf{I} - \vec{u}\vec{u} - \frac{1}{N-1}(\vec{u} - \vec{u}_s)(\vec{x} \times \vec{\omega}) + \frac{1}{N-1}\vec{\omega}(\vec{x} \times \vec{u})$$
$$+ \frac{1}{N-1}[\vec{x} \cdot (\nabla \cdot \mathbf{T})\mathbf{I} - \vec{x}(\nabla \cdot \mathbf{T})] + \mathbf{T} \qquad , \qquad 1.4$$

and V_f is the volume of the control volume, S_b is the surface area of the body, and S_f is the surface of the control volume (Noca, 1999). In Eq. 1.3 and Eq. 1.4, the position vector is given as $\vec{x}$, the velocity in the control volume is $\vec{u}$, the vorticity is $\vec{\omega}$, the outward normal unit vector is $\hat{n}$, and N is the dimension of space ($N = 3$ for three dimensional flows and $N = 2$ for two dimensional flows). The velocity of the body surface is denoted as $\vec{u}_s$, the unit tensor is $\mathbf{I}$, and the traction tensor is $\mathbf{T}$. This relationship requires detailed knowledge of the flow at and near the body surface as well as the velocity on the body surface. An alternative form of this expression is possible when a fluidic body is considered. Again, Noca (1996) expresses it as

$$\vec{F} = -\frac{1}{2}\frac{d}{dt}\iiint_{V_f(t)}\rho\vec{x} \times \vec{\omega}\,dV + \frac{d}{dt}\iiint_{V(t)}\rho\vec{u}\,dV$$
$$-\frac{1}{2}\frac{d}{dt}\iiint_{V(t)}\rho\vec{x} \times \vec{\omega}\,dV + \oiint_{S_f(t)}\rho\hat{n} \cdot \vec{\gamma}\,dS \qquad 1.5$$

where V is the volume of the body and we have assumed a three-dimensional flow. Examination of each term on the right-side of Eq. 1.5 shows that this relation can be simplified further for its use in the present study.

The first term on the right-side of Eq. 1.5 is the time derivative of the impulse of the flow in the control volume where the impulse is defined as

$$\vec{I} \equiv -\frac{1}{2}\iiint_{V_f(t)}\rho\vec{x} \times \vec{\omega}\,dV . \qquad 1.6$$

10

This term represents the contribution of the vortical component of the wake. If we assume a cylindrical coordinate system, as shown in Fig. 1.4, the largest aerodynamic forces on the canopy will be those in the axial direction (*i.e.* the drag). Therefore, taking only the axial component of the impulse, Eq. 1.6 simplifies to

$$I_z = -\frac{1}{2} \iiint_{V_f} \rho r^2 \omega_\theta \, dr d\theta dz \qquad 1.7$$

where r is the radial distance from the centerline of the canopy and ω_θ is the azimuthal component of the vorticity. Further, if we assume incompressible and axisymmetric flow then, the axial impulse reduces to

$$I_z = -\pi\rho \iint r^2 \omega_\theta \, dr dz. \qquad 1.8$$

Therefore, the drag force associated with the impulse of the flow around the canopy (*i.e.*, the vortical force) is given by

$$F_\omega = \frac{dI_z}{dt} = -\pi\rho \frac{d}{dt} \iint r^2 \omega_\theta \, dr dz. \qquad 1.9$$

The vortical force can be altered by either changing the amount of vorticity in the flow or by moving the vorticity radially in the flow. Since the velocity field was measured in a diametrical plane, the azimuthal component of the vorticity is available from the data.

The second term on the right-side of Eq. 1.5 can be related to the unsteady potential flow around the canopy. The velocity in the integrand is the velocity of the fluid interior to the body, in this case, the velocity of the fluid inside the inflating canopy. As a limiting case, since the canopy material is nearly impermeable, the maximum velocity on the canopy interior is small, and in any case no more than the freestream velocity. Assuming the interior velocity remains approximately uniform and constant, this term can be estimated by

$$\frac{d}{dt} \iiint \rho \bar{u} dV \leq \rho U_\infty \frac{dV}{dt} = \rho U_\infty \dot{V} \qquad\qquad 1.10$$

This is reasonable since the drag of a translating, expanding sphere in an inviscid flow is proportional to the rate of change of the volume of the sphere (Karamcheti, 1980 and Panton, 1996). However, Eq. 1.10 is a limiting case since the average velocity on the interior is expected to always be significantly less than the freestream velocity. The flow should either stagnate on the interior of the canopy (Lamberson *et al.*, 1999) or at most a re-circulation region may establish itself inside the canopy. The magnitude of the maximum interior velocity is expected to be smaller than the freestream velocity. Introducing a proportionality constant, k_p, of order one to account for the limiting case analysis, the force due to the unsteady potential flow is estimated by

$$F_p = k_p \rho U_\infty \dot{V} \qquad\qquad 1.11$$

where k_p is taken to be one in our calculations.

The third term is related to the impulse of the interior flow. Since measurements of the interior flow were not possible in the experiments, no knowledge of the vorticity in this region is available. Again, this region of the flow would be a stagnation point, and no significant amount of vorticity is expected in this region. We would not expected this term to change rapidly with time and the derivative of the interior impulse is expected to be small.

Finally, the last term of Eq. 1.5, relates to the flow at the outer surface of the control volume. The control volume used in the calculation should be as large as possible to contain all the vorticity in the wake. The control volume used in the present calculations encompasses both the wake and inviscid regions. Since the viscous stresses

12

and vorticity are zero outside the wake, we expect that the contribution of this term to the total force be small when compared to the first two terms in the Eq. 1.5. Then, the primary forces the body experiences will be from the time derivative of the impulse in the wake and the potential flow component; all other terms are neglected. The aerodynamic forces that the canopy experiences can thus be estimated by

$$F = F_p + F_\omega \approx k_p\, \rho U_\infty\, \dot{V} - \pi\rho\frac{d}{dt}\iint r^2\omega_\theta\, dr dz. \qquad 1.12$$

Based on this relationship, the drag can be estimated from measurements of the velocity field in the wake of the canopy and the volume enclosed by the canopy. This estimate can then be compared to direct drag measurements and the significance of the various components can be established.
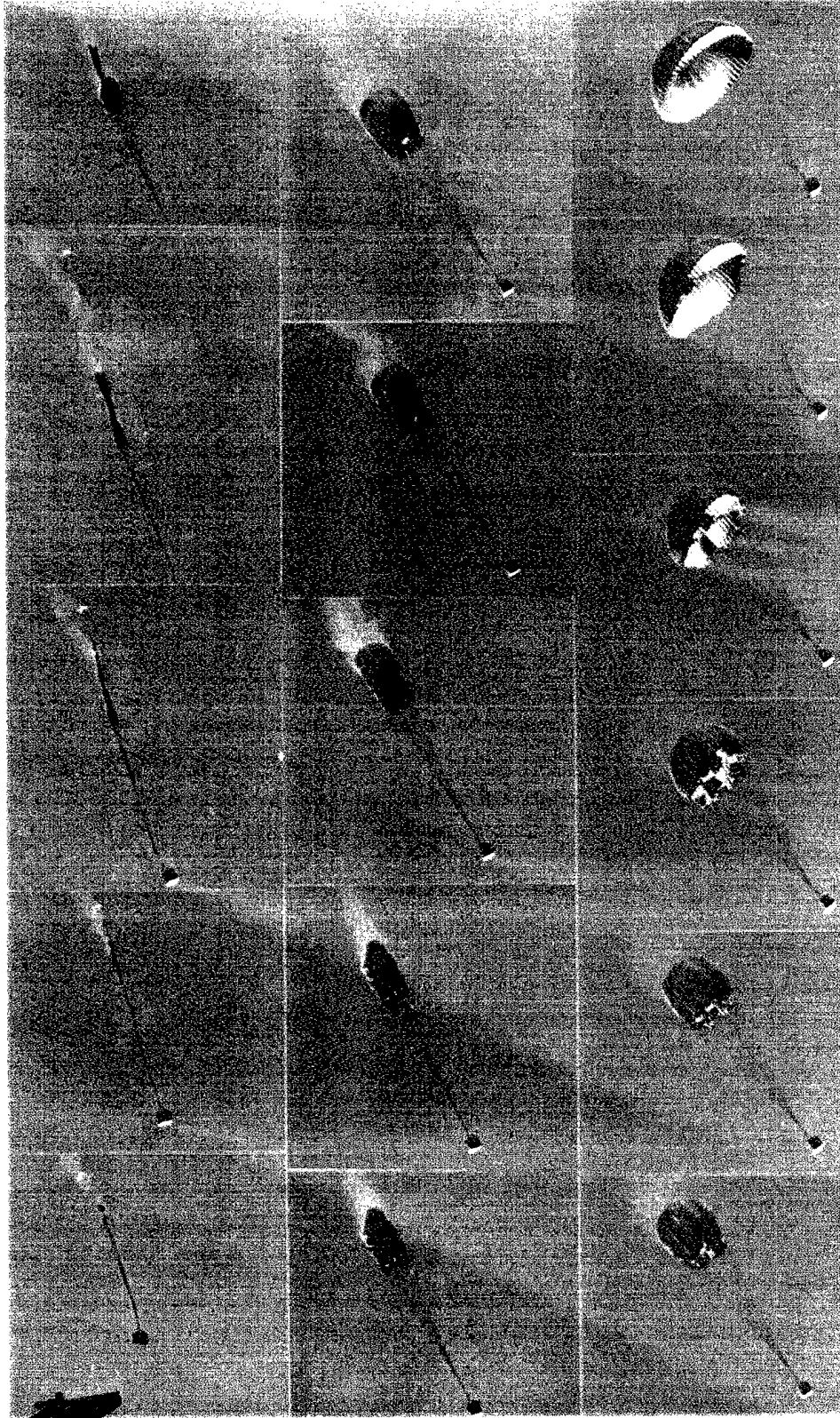
Figure 1.1. Images of a full-scale parachute inflation (Lee, 1998).
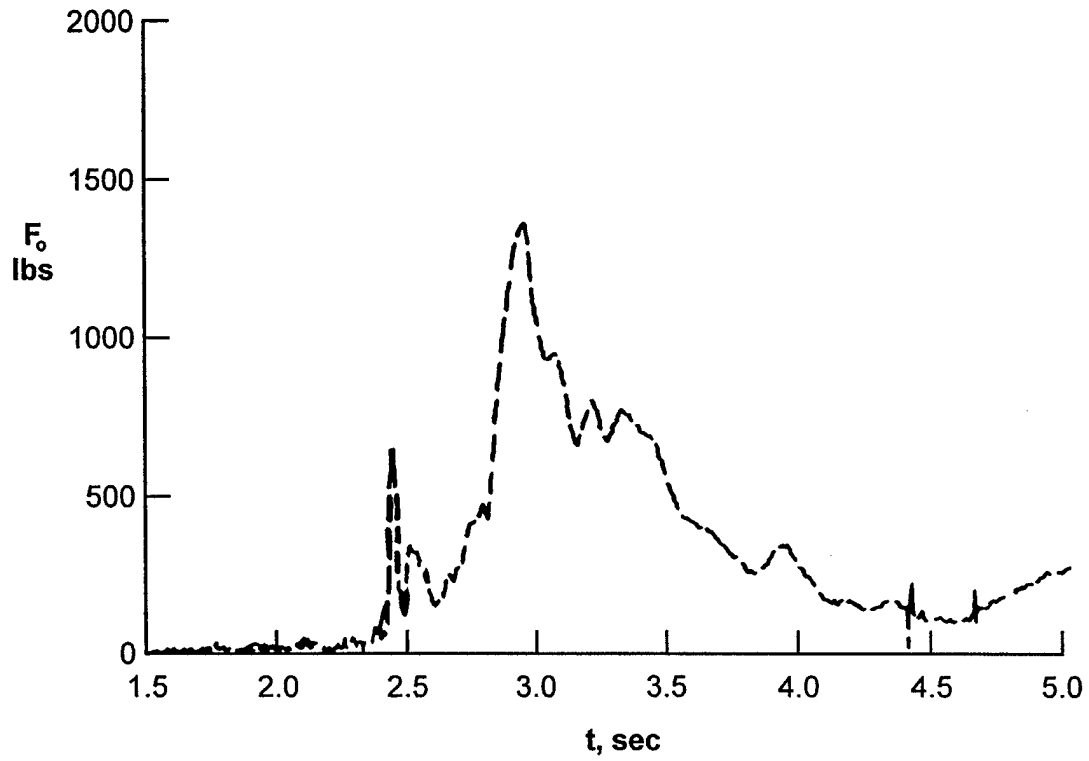
Figure 1.2. Opening force during full-scale parachute inflation (adapted from Lee, 1994).
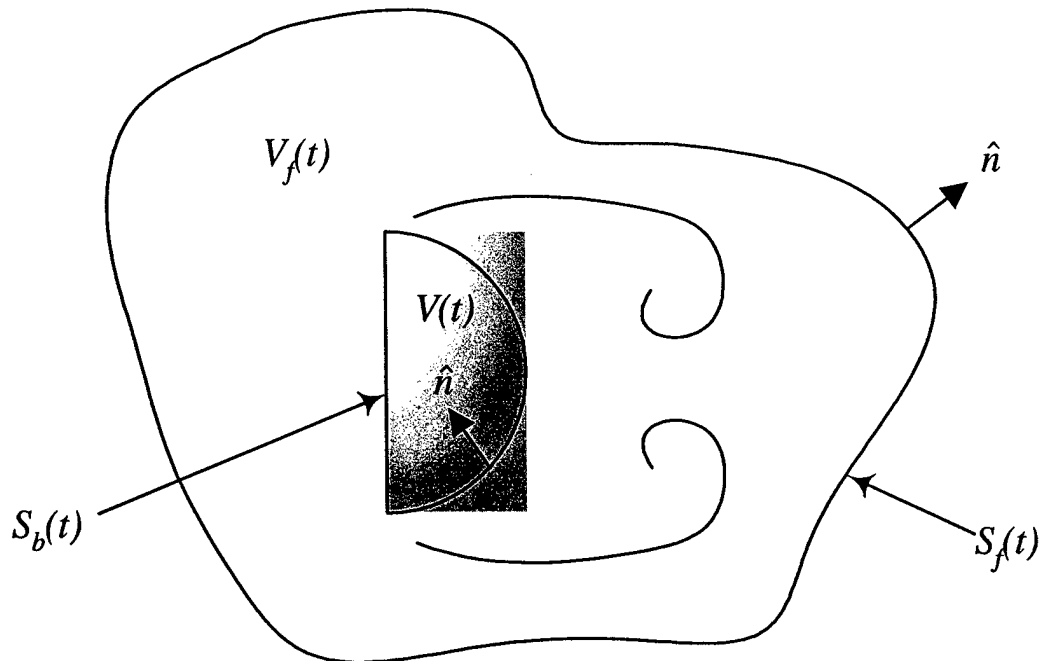
Figure 1.3. Control volume for calculation of aerodynamic forces.

15
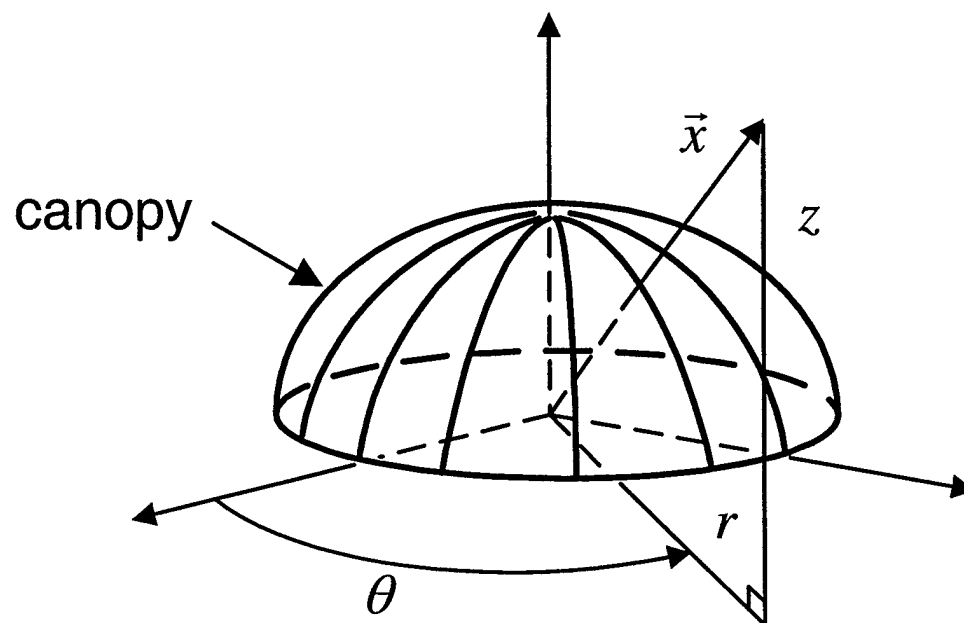
Figure 1.4. Cylindrical coordinate system used.

2. Experimental Setup

2.1 Water Tunnel Apparatus

The experiments were conducted in the WPI free-surface water tunnel facilities. A schematic of the experimental setup is shown in Fig. 2.1 and photographs of the experimental setup are shown in Fig. 2.2. The experiments were conducted in the water tunnel to aid in the measurement of the velocity field around the canopy. The velocity field measurements were made using the Particle Image Velocimetry (PIV) technique. The PIV technique is more easily implemented in water than air. Also in water, longer inflation times were achieved for the canopies tested than would be achieved if the tests were performed in a wind tunnel. The water tunnel test section has internal dimensions of 0.6 m wide by 0.6 m deep by 2.4 m long. The water tunnel was operated at the nominal speeds listed in Table 2.1. The actual speeds, U_∞, were measured using a Laser Doppler Velocimetry (LDV) system which also provided a measure of rms-value of the velocity fluctuations, U'_{rms}. These measurements were taken along the tunnel centerline approximately 0.5 m downstream of the test section entrance.

Table 2.1. Freestream velocities in water tunnel.

Nominal U_∞ (cm/s)	Actual U_∞ (cm/s)	U'_{rms}/U_∞
20	19.622	1.19%
25	24.585	1.16%
30	29.328	1.23%
35	34.452	1.05%
40	39.134	1.29%

The parachute assembly was attached to a stationary streamlined forebody in the water tunnel (see Fig. 2.3). This placed the parachute assembly in a horizontal orientation. The forebody had a diameter of 1.4 cm and a length of approximately

17

17.5 cm. By keeping the forebody streamlined and minimizing its dimensions, the wake effects were also kept to a minimum. Flow visualization was performed to confirm that the forebody wake minimally affected the parachute. The forebody was supported by 0.64 cm diameter rods in the center of the water tunnel test section and approximately 60 cm downstream of the test section entrance.

For the canopy inflation experiments, the canopy was packed into a round deployment tube downstream of the forebody that was pulled away to start the inflation process. The canopy packing process is explained in the next section. The ratio of deployment tube diameter to constructed canopy diameter, D_o, was fixed at 7%. The deployment tube was pulled away by a thin nylon string, which passed through a series of pulleys and was attached to a stepper motor (see Fig. 2.4). The stepper motor extracted the deployment tube at a time that was synchronized with the force measurement and the imaging systems. The details of the synchronization and stepper motor control are presented in Section 2.4. The tube was pulled at a speed of approximately 65 cm/s.

2.2 Canopy Specifications

The parachute models were constructed using a solid cloth, flat circular geometry. The canopies studied had constructed diameters of 15.2 cm and 30.5 cm. A diagram of the canopy geometry along with definitions of the dimensions associated with the canopy is shown in Fig. 2.5. The canopies tested had no vent hole. A Reynolds number, Re_{Do}, based on the constructed diameter is

$$Re_{Do} = \frac{U_\infty D_o}{\nu},$$
(2.1)

18

where ν is the kinematic viscosity of water ($\nu = 0.01$ cm^2/s). Table 2.2 lists the Reynolds numbers as well as the water tunnel solid blockage, ε^{sb}, for the canopies and velocities tested under steady state conditions. For blockages of 10% or less (Cockrell, 1987), corrections for the dynamic pressure were applied for the data measured in the steady state canopy experiments (Macha and Buffington, 1989). The dynamic pressure, q_o, was corrected as

$$q_o = q_{o_u} \left[1 + K_M \frac{C_{D_u} S_p}{S_T} \right] \qquad 2.2$$

where q_{ou} is the uncorrected dynamic pressure, K_M is a blockage factor derived from previous experimental data (Macha and Buffington, 1989), C_{Du} is the uncorrected drag coefficient of the canopy, S_p is the projected area of the canopy diameter, and S_T is the cross-sectional area of the tunnel test section. No corrections were applied to the canopy inflation experiments primarily due to the low blockage that occurs during most of the inflation process.

Table 2.2. Reynolds number and solid blockage.

U_∞ (cm/s)	D_o (cm)	$Re_{Do} \times 10^{-4}$	ε^{sb}
20	15.2	2.98	2.5%
25	15.2	3.73	2.5%
30	15.2	4.45	2.5%
35	15.2	5.23	2.5%
40	15.2	5.94	2.5%
20	30.5	5.96	9.9%

Full-scale canopies have dimensions on the order of 10-30 m, thus the canopies in this study are on a very small geometric scale which naturally leads to the question of Reynolds number and scale effects. Typically full scale canopies descend at a speed of 5-

19

10 m/s which would result in a Reynolds number on the order of 10^6-10^7. These values are very difficult to achieve in any laboratory setting especially in a water tunnel. Knacke (1992) shows that Reynolds number has little effect on the drag of a canopy over the range of Reynolds number 10^5-10^6. The present research was limited to the Reynolds number range listed in Table 2.2 due to the limitations of the experimental facilities. Scale effects are an important characteristic of parachute modeling. Heinrich and Hektner (1971) and Lee (1989) showed that the canopy flexibility is an important characteristic. The overall performance of the canopy is affected by the stiffness of the canopy. However, given the proper scaling parameters, the scale effects can be accounted for in the inflation characteristics (Johari and Desabrais, 2001).

The significant scale difference also introduces technical difficulties in the construction of the canopy models. New methods were needed for constructing the canopy models. Traditional full-scale parachute canopies are constructed by sewing individual panels or "gores" together to form an approximate circular geometry (Knacke, 1992). Constructing the canopy models in this method would result in the models having larger than necessary stiffness due to the sewing seams along the edge of each gore. In order to minimize the stiffness effects at these small scales, it was decided that the canopy should be made from one solid piece of material instead of individual gores being sewn together. The parachutes were constructed from standard 1.1 oz/yd^2 rip-stop nylon and manufactured by cutting the material around a flat circular template at the appropriate diameter. The edge of the nylon material was seared, preventing it from fraying. An image of the canopy edge between two suspension lines in shown in Fig. 2.6.

20

The permeability of the canopy material is characterized by the mean flow across the canopy material. This flow velocity through the material is a function of the pressure differential and the material pore size. An estimate of the pressure differential can be made based on the dynamic pressure. A full size parachute descents at ~ 6 m/s in air ($\rho = 1.2$ kg/m^3) which results in a dynamic pressure of ~ 22 Pa. The small scale models were placed in a freestream of 20 cm/s in water ($\rho = 1000$ kg/m^3) which results in a dynamic pressure of ~ 20 Pa. This shows that the scale models in water operate at similar dynamic pressures regimes as full scale canopies where the permeability characteristics of full scale canopies is well known. It is therefore expected that the small scale model permeability characteristic will be similar to those of the full scale canopies. However, it should be noted that the viscosity of air and water differ by two orders of magnitude which may affect the permeability characteristics of the material.

The suspension lines were made from 100 μm diameter nylon thread. The length of the suspension lines, l_s, was approximately equal to the constructed diameter of the parachute canopy, *i.e.* $l_s \cong D_o$. It was decided that the number of suspension lines on each parachute assembly should be 24. This number was based on early preliminary experiments in which only 8 or 12 suspension lines were used. The low number of suspension lines caused significant bulging or "ballooning" of the canopy between the suspension lines. By increasing the suspension line count to 24, the inflated canopy shape qualitatively matched those observed on full-scale parachutes. Full-scale parachutes typically have 16-28 suspensions lines (Knacke, 1992).

The suspension lines were attached to the canopy by creating a small loop at the end of the suspension line that was passed through a hole near the edge of the canopy

21

skirt (see Fig. 2.6). The loop in the suspension line was created using a bowline knot (Bigon and Regazzoni, 1982). The hole in the canopy was seared again to reduce the potential for fraying. The other ends of the suspension lines were attached to a parachute mount. The mount was designed to allow for the adjustments of the length of each suspension line separately (see Fig. 2.3). This ensured that all the suspension lines were of equal length. The parachute mount was attached to the end of the forebody, which was also the end of a load cell used to measure the force the canopy experienced.

Based on the measured force, the maximum opening force was approximately 6 N. This results in a stress of approximately 32 MPa (4600 psi) in each suspension line. This results in an estimated elongation of the suspension lines (based on stress-strain curves for nylon published in Bixby et $al.$, 1978) of ~0.03% (0.05 mm) which is negligible. It is therefore reasonable to assume the suspension lines are inelastic.

Flat circular canopy geometries are notorious for large off-axis oscillations when fully inflated. In order to minimize this motion, a thin (0.5 mm diameter) flexible nylon retention line was attached to the forebody and passed through the apex of the canopy. The end of the retention line was held rigidly far downstream of the canopy. The retention line applied the necessary force to restrain the canopy wandering but should not adversely affect other aeroelastic effects. At the apex of the canopies, a small (~5 mm diameter) hard grommet (see Fig. 2.7) was secured to the canopy material to allow the retention line to pass through the material without substantially damaging the canopy.

The packing of the canopy into the deployment tube for the inflation experiments consisted of drawing the canopy into a roughly cylindrical shape by hand with the water tunnel turned off. The canopy was then pushed into the deployment tube until the canopy

was fully encased by the tube with only the suspension lines visible. The packed canopy (with the deployment tube) was then pulled to a position where the suspension lines were taunt. The water tunnel was then turned on and the freestream velocity was established in the test section after which the deployment tube was extracted to begin the inflation process. This packing process resulted in inconsistent folding of the canopy material. The small scale of the canopies prevented development of a method to fold the canopy in a repeatable and prescribed manner. However, a set of experiments showed that the packing method utilized here resulted in an overall inflation process that was symmetric and statistically repeatable.

2.3 Imaging System

The experiments were recorded using a CCD camera to observe the development of the canopy geometry and the flow field surrounding the canopy. Sample images obtained from the experiments are shown in Fig. 2.8. The camera was mounted at a right angle to the parachute assembly. Also, the camera was mounted on its side so that in the images, the parachute assembly had a vertical orientation with the fluid flow from the bottom to the top of the image. The camera used (a Pulnix model no. TM-1040) was a progressive scan 8-bit monochrome CCD camera with a $1k \times 1k$ pixel resolution and a 30 Hz frame rate. A 24 mm lens was mounted on the camera with the f-number and the shutter speed set depending on the experiments to be recorded. The images were digitally transferred (in real-time) from the camera to the system memory of a PC through a video capture card (μTech model no. MV-1000/1100). The computer had 512 MB of RAM which allowed for approximately 450 frames (or ~15 s) to be recorded at the

23

maximum camera resolution. Each recorded frame was stored on a PC hard disk.

The imaging of the experiments can be separated into two groups, one group in which only the canopy geometry was imaged and another group where the velocity field around the canopy was imaged. Each case required significantly different lighting requirements. For the former case, the water tunnel test section was backlit by a floodlight through a white diffuser screen mounted on the back of the water tunnel wall. This arrangement allowed for a clean white background behind the dark gray image of the canopy which creates a clear contrast between the background and foreground for use in image processing (see Fig. 2.8a). The f-number of the lens was set to a half-click less than the 5.6 setting and the shutter speed of the camera was set to 1/250 s. An image processing routine was developed to extract the temporal evolution of the maximum projected diameter, D_m, the canopy height, H, and an estimate of the volume enclosed by the canopy, V, from each sequence of images. The uncertainty in the maximum projected diameter and the canopy height was ± 5 pixels $\approx 0.005 \, D_o$ and the volume has an uncertainty of 15% estimated from the uncertainty of the diameter and height.

For the case of imaging the canopy and the velocity field around the canopy, the overall lighting requirements were dictated by the requirements of the Particle Image Velocimetry (PIV) system. In this case, the laser used in the PIV system provided the illumination for the region of interest in the water tunnel. The overall details of the PIV system are presented below; details of the laser orientation are presented here. The PIV system uses a laser sheet to illuminate the flow field. The sheet originates in the upper right corner of the images towards the lower left corner and is parallel to the centerline of the canopy. The intersection of the laser sheet with the canopy caused part of the upper

24

surface of the canopy to be brightly lit, providing a sharp contrast between the canopy edge and the dark background. However, the laser light did not completely penetrate through the material of the canopy which caused a shadow to be formed where the canopy blocked the laser sheet. The shadow can be seen directly below and in the lower left corner of the image in Fig. 2.8b. The f-number of the lens was set to 2.5 and no external shutter was used. The CCD was readout at a time of 1/60 s. The geometry of the canopy was extracted manually from these images. A simple closed polygon was manually selected to estimate the shape of the canopy at each instant of time throughout the sequence. An example of this is shown in Fig. 2.9. Also, the maximum projected diameter was manually measured from these image sequences. The uncertainty in the maximum projected diameter, measured by this method, was ± 10 pixels $\approx 0.01 D_o$.

2.4 Force Measurements

The force, F, measurements were made with a strain gage based load cell mounted in the stationary forebody (see Fig. 2.3). The load cell was mounted such that only forces directly applied to the canopy through the suspension lines were measured. The output voltage of the load cell was passed through a custom designed low noise amplifier. The amplifier provided a gain of 200. The output voltage of the amplifier was measured by a 12-bit A/D data acquisition system (Data Translation model no. DT2805). The data were sampled at a rate of 150 Hz without any gain at the data acquisition card. The uncertainty of the force measurement system was 0.4% at full scale of the load cell or 0.027 N. This corresponds to approximately 10% of the smallest steady state drag force measured. The load cell was calibrated using static loads with the load cell

generator connected to the stepper motor controller set the speed at which the stepper motor rotated.

2.5 PIV System

The velocity field in the near wake of the canopy was measured using a PIV system. The particulars of the PIV method are described by Willert & Gharib (1991) and Raffel *et al.* (1998). A dual pulsed Nd:YAG laser was utilized in the experiments. The laser pulses were synchronized with the CCD camera frame rate, and the time separation, Δt, between successive pulses was established by a counter/timer board in a PC. The time separation between pulses was set depending on the freestream velocity. Table 2.3 lists the pulse separations used at each speed as well as the area imaged, A_i, for each canopy.

Table 2.3. Laser pulse separation and imaging areas.

U_∞ (cm/s)	D_o (cm)	Δt (ms)	A_i (cm^2)
20	15.2	6.00	20.0 × 20.0
30	15.2	4.56	20.0 × 20.0
40	15.2	3.00	20.0 × 20.0
20	30.5	6.00	23.9 × 23.9

Each laser pulse had a duration of 5 ns and an energy output of approximately 15 mJ. The laser was pulsed at a frequency of 30 Hz that generated velocity fields at a rate of 15 Hz, due to the frame straddling method used in the PIV measurements. The laser pulses were directed through a negative cylindrical lens (focal length of - 6.35 mm) to create a laser sheet for illumination of the flow field directly behind the canopy. The laser sheet had a thickness of 4-5 mm and was oriented parallel with the freestream velocity. The flow field was seeded with neutrally buoyant silver-coated particles that

27

had a mean particle diameter of 45 µm. Figures 2.8b and 2.9 provide good examples of the seeding density in the flow fields.

The PIV processing algorithm used interrogation windows of 32×32 pixels with an overlap step of 8 pixels. This produces a discrete array of approximately 13700 velocity vectors per field. The spatial resolution of the velocity vectors was 1.7 mm for the experiments with the 15 cm canopy and 2.0 mm with the 30 cm canopy. The vector processing algorithm is outlined in Willert & Gharib (1991). The area of the velocity field measured was approximately 1.5 diameters downstream of the canopy apex (refer to Table 2.3). The origin of the coordinate system was defined as the bottom of the field of view along the centerline of the canopy. The uncertainty of the velocity vector is approximately 3%; this is comparable to estimates made by Willert & Gharib (1991).

The existence of a boundary in the images of the flow field (*i.e.* the canopy) causes the velocity vectors near the boundary to be calculated improperly. This is due to a deficiency of particles in the interrogation windows that contain a large portion of the imaged boundary with only a small region of the flow field itself imaged. A moving boundary only compounds the issue since the PIV processing algorithm may estimate a particle displacement that was corrupted by the motion of the boundary. In the images, the moving canopy appears as a continuously varying gray-scale region that changes appearance in the image pair that is used to calculate the displacement vectors. The processing algorithm calculates a corrupted displacement vector in and near the canopy region due to the changing pixel values of the canopy region in the image pair. In order to minimize this corruption effect, the pixel gray-scale level in the canopy region was set to black (the background color) in both images in the pair. Therefore, the only pixel

motion seen in each interrogation window was that associated with the motion of the imaged particles. The region of the image where the canopy was located was selected by the process described in Section 2.3. It should also be stated that the flow field in the interior of the canopy is not measured.

The azimuthal vorticity, ω_θ, of the flow field was calculated from the velocity field using a method suggested in Raffel *et al.* (1998). The method estimates the average vorticity at a grid point in the field by evaluating the circulation around the eight neighboring points and dividing by the area enclosed by the eight points. The uncertainty of the vorticity calculations is 8%.

The circulation, Γ, around any closed path can be found from the velocity and/or vorticity fields. The circulation of the boundary layer formed on the canopy surface was estimated by integrating the velocity along a contour of constant vorticity.

The impulse of the flow was calculated using a discrete form of Eq. 1.8. The region used in the integration was a rectangular area that enclosed all the vorticity in the plane to the right of the canopy centerline (*i.e.* $r \geq 0$). The edges of the integration region were located five vector grid points from the sides of the full vector field. A sample of the integration path is shown in Fig. 2.11.
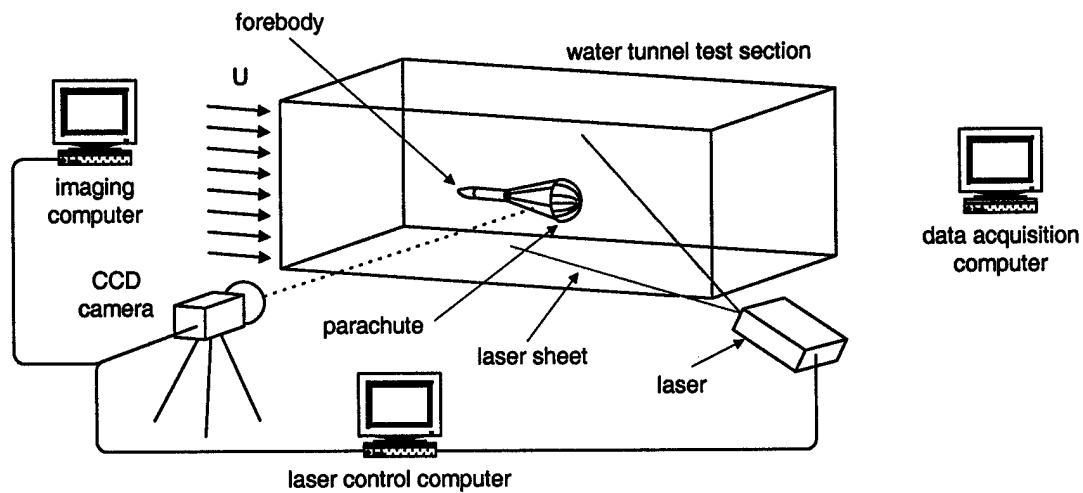
Figure 2.1. Schematic of experimental setup.

a)   b)
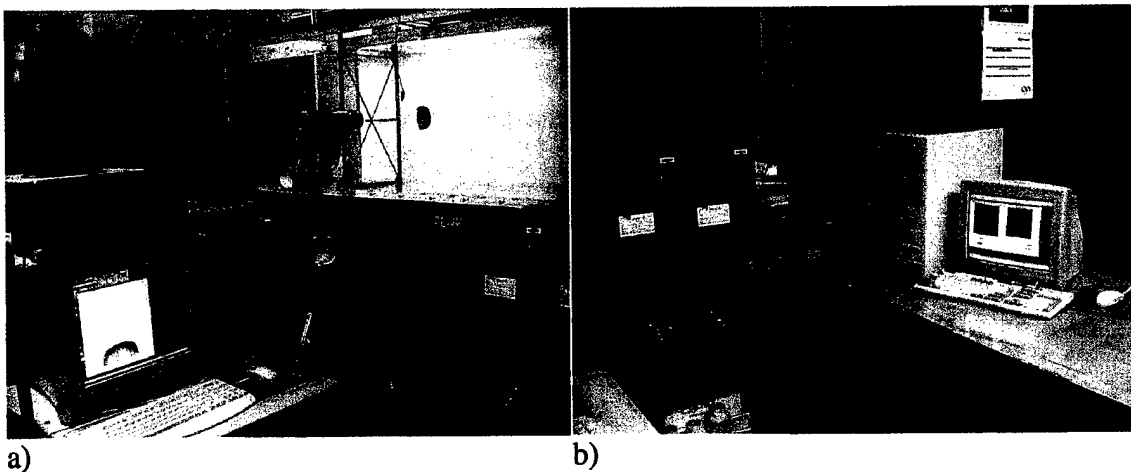
Figure 2.2. Photographs of experimental setup, a) imaging computer, camera, and parachute model in water tunnel; b) data acquisition computer and lasers used in PIV system.
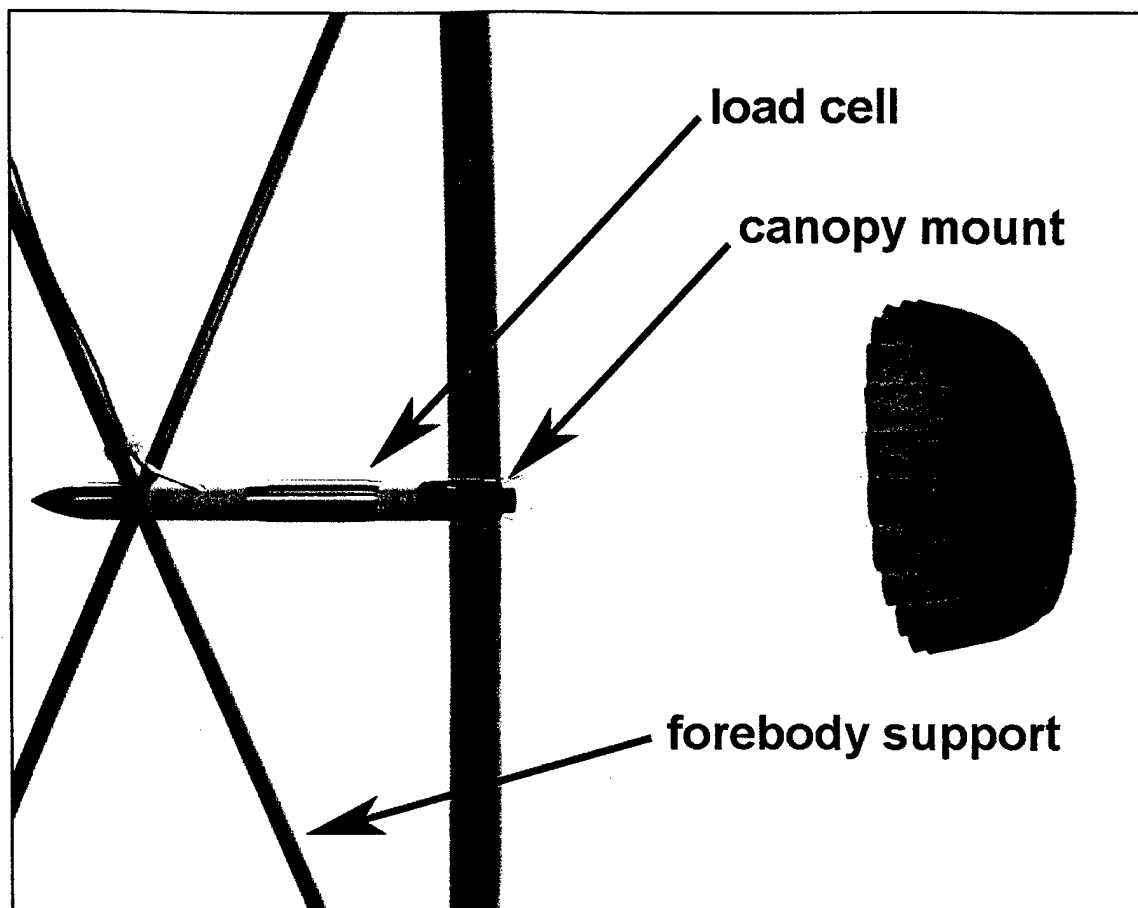
a)
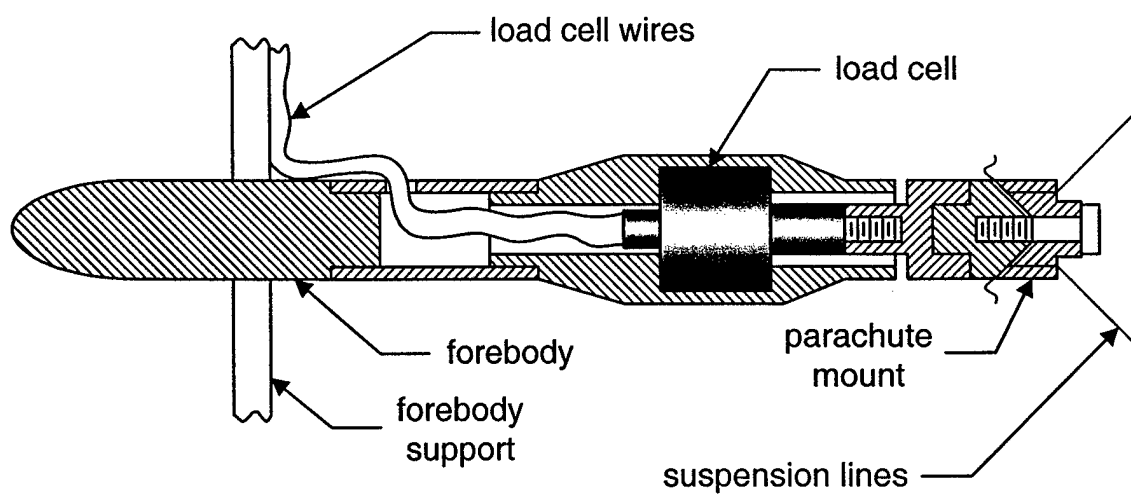
b)

Figure 2.3. Details of forebody, a) image of forebody and an inflated canopy; b) cross-sectional view of forebody, load cell, and parachute mount.
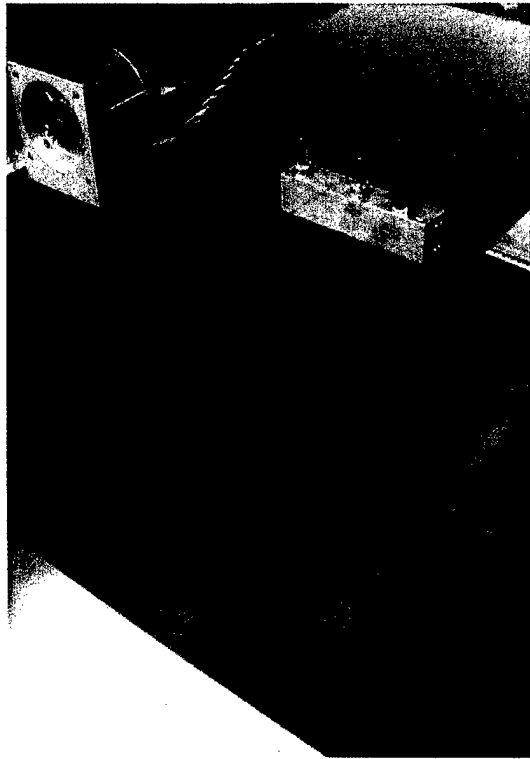
Figure 2.4. Image of deployment tube pulley system and stepper motor.
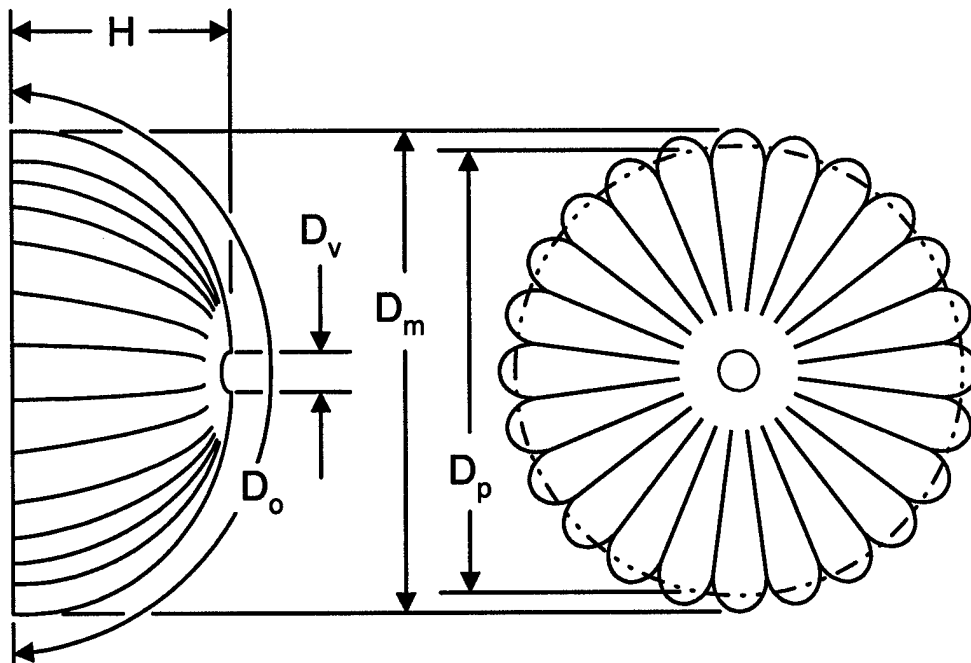
Figure 2.5. Schematic of parachute geometry and associated dimensions.
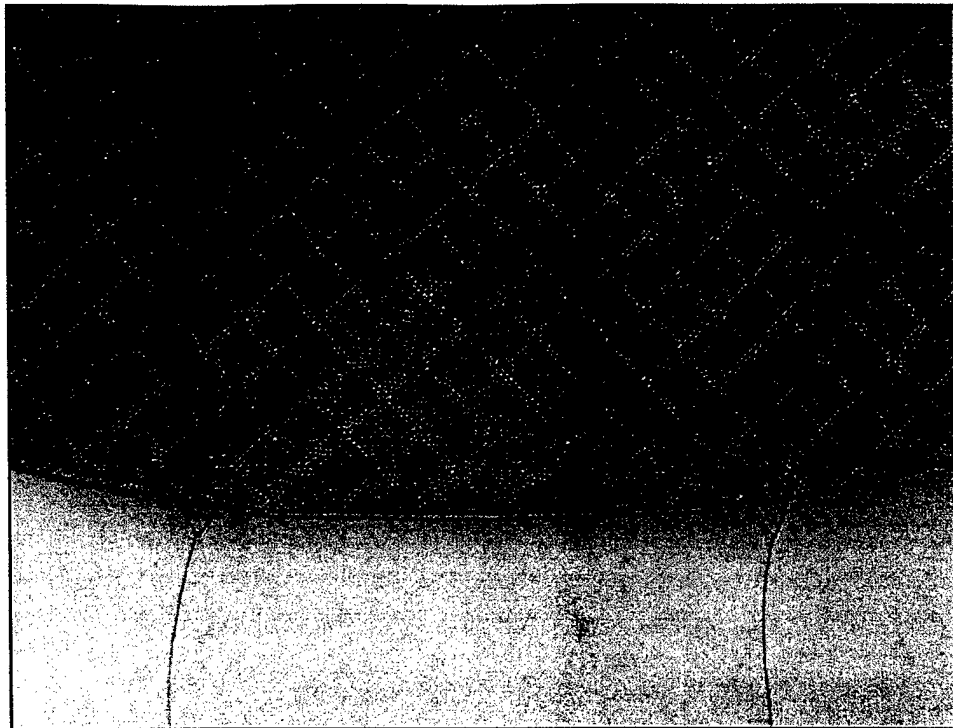
Figure 2.6. Image of the canopy edge and suspension line attachment.

Figure 2.7. Close-up image of hard grommet at apex of canopy.

33
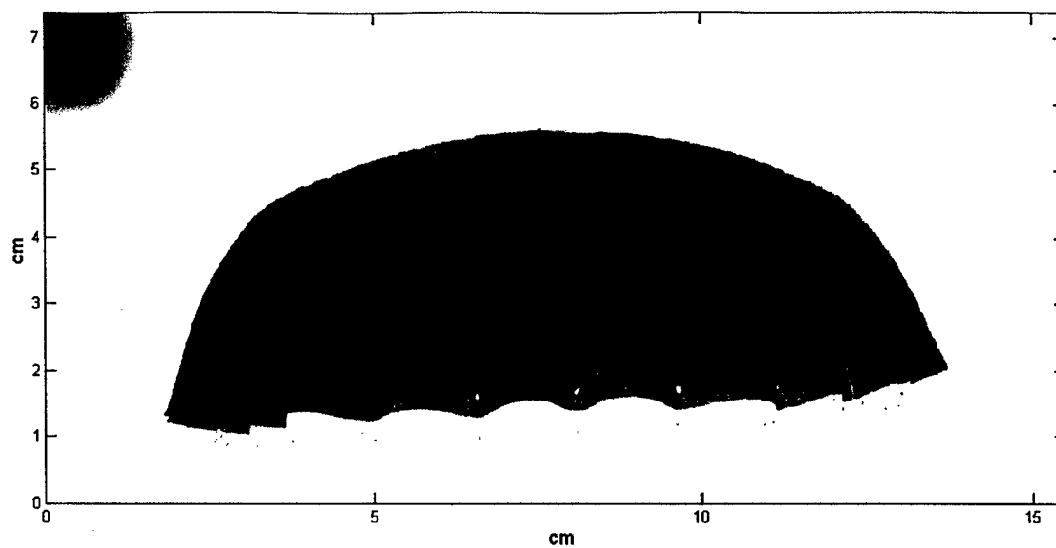
a)
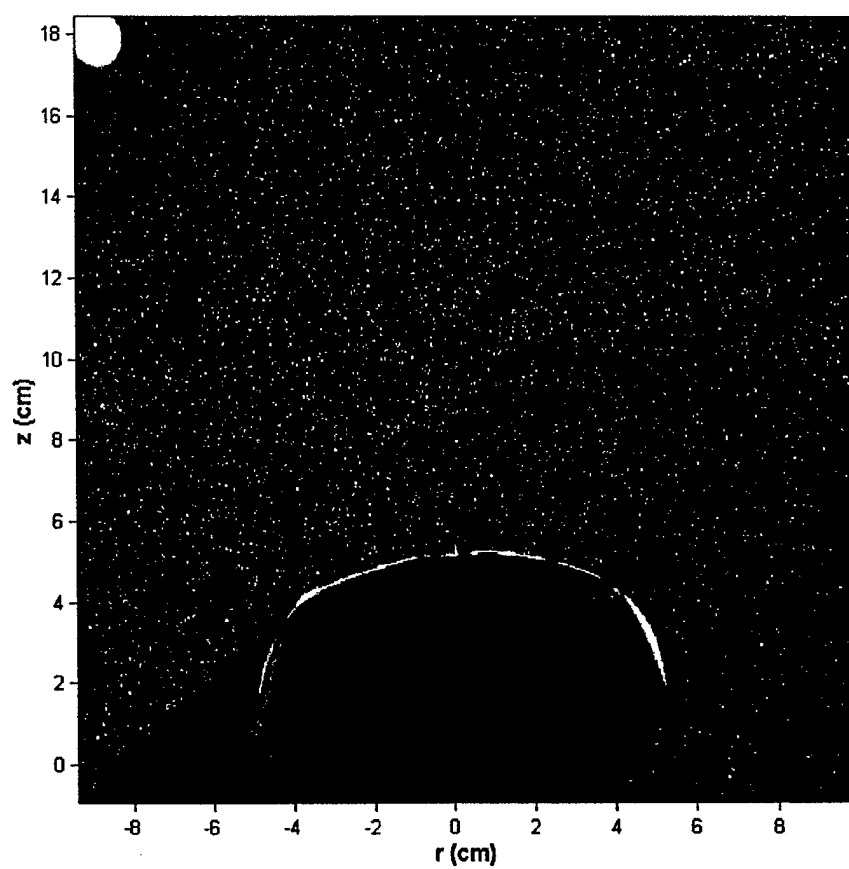
b)

Figure 2.8. Sample images from a) a geometry experiment and b) a velocity field experiment.

34
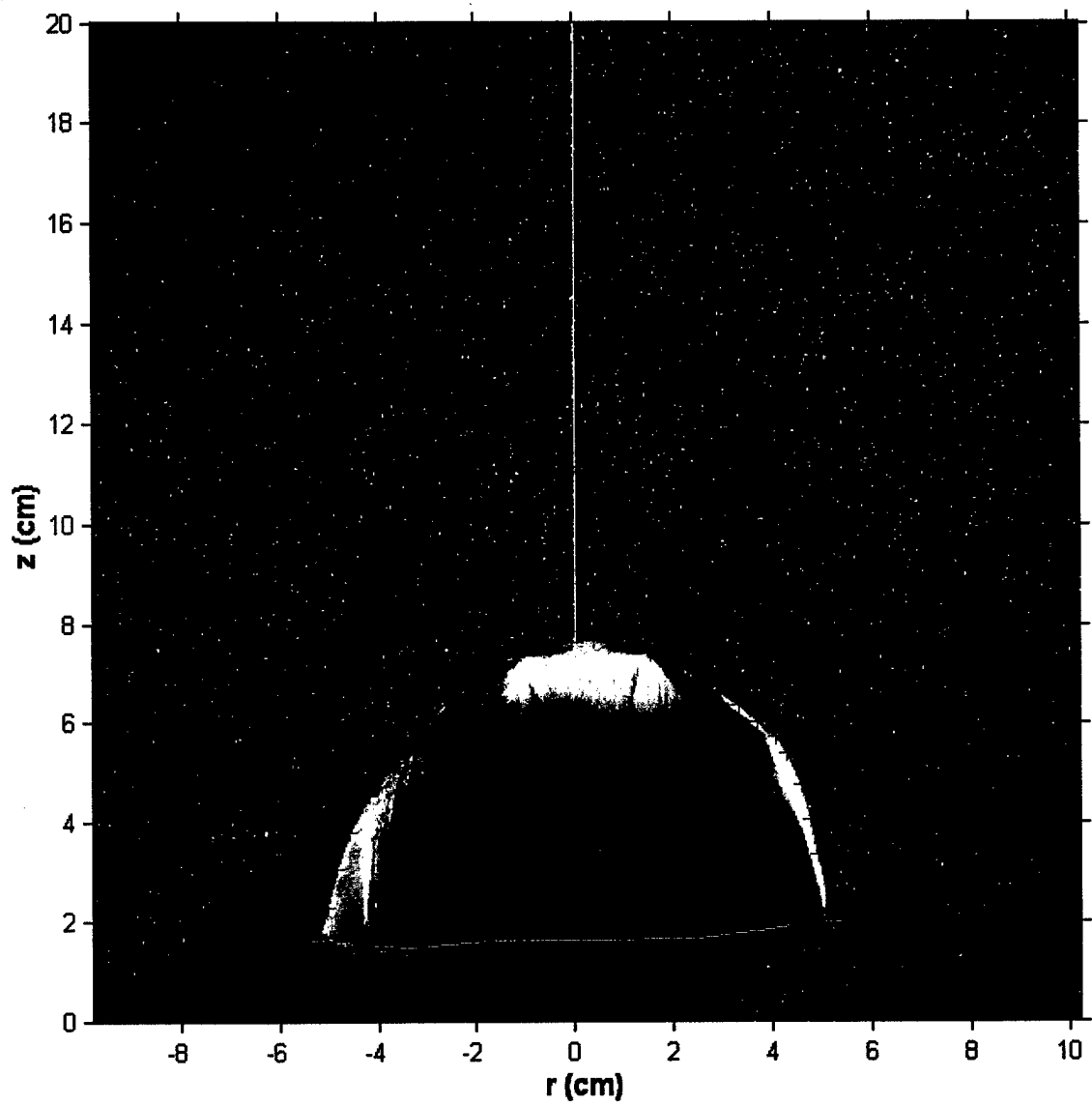
Figure 2.9. Sample image of canopy contour selected from original image.
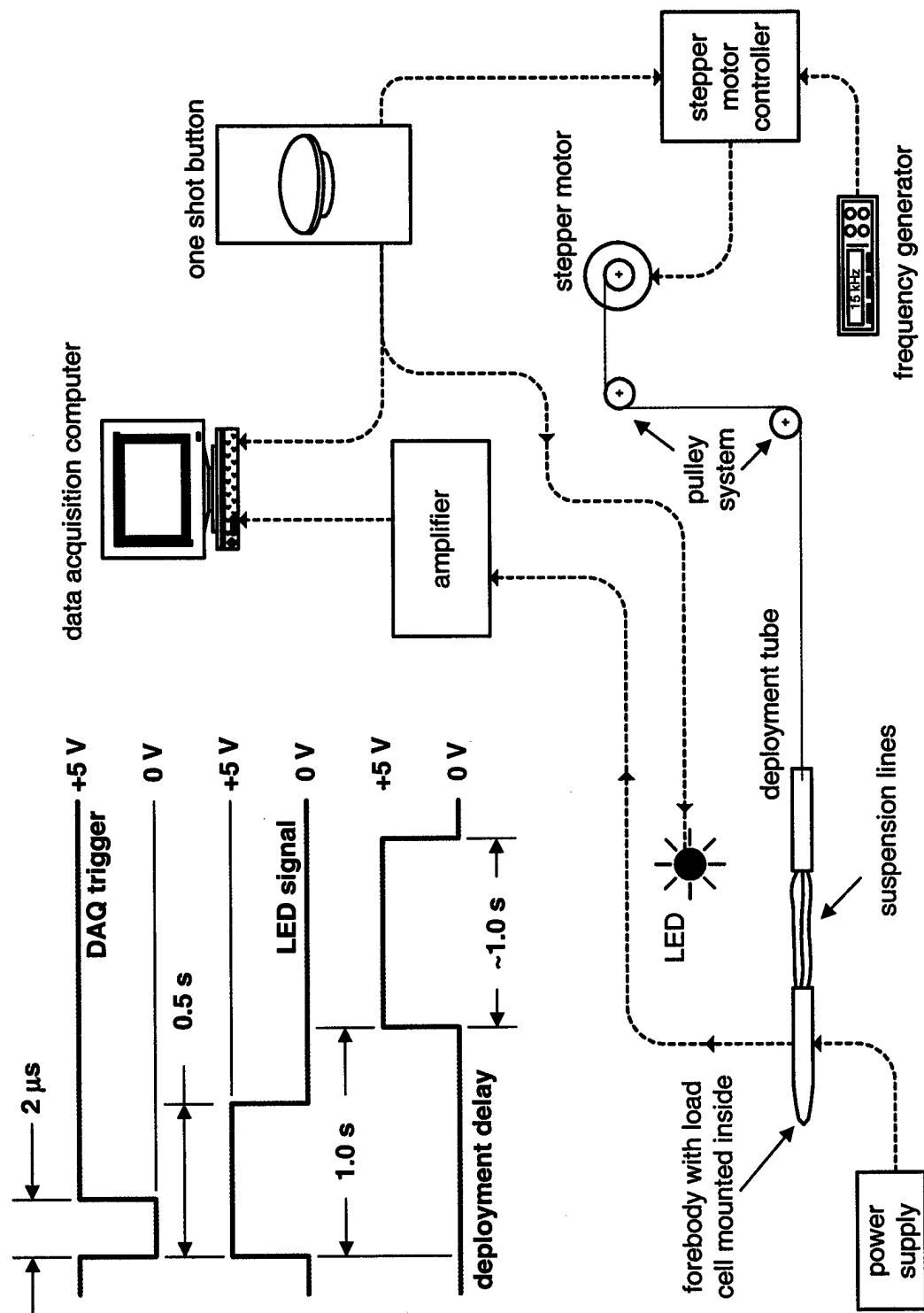
Figure 2.10. Schematic of the measurement synchronization system.

36
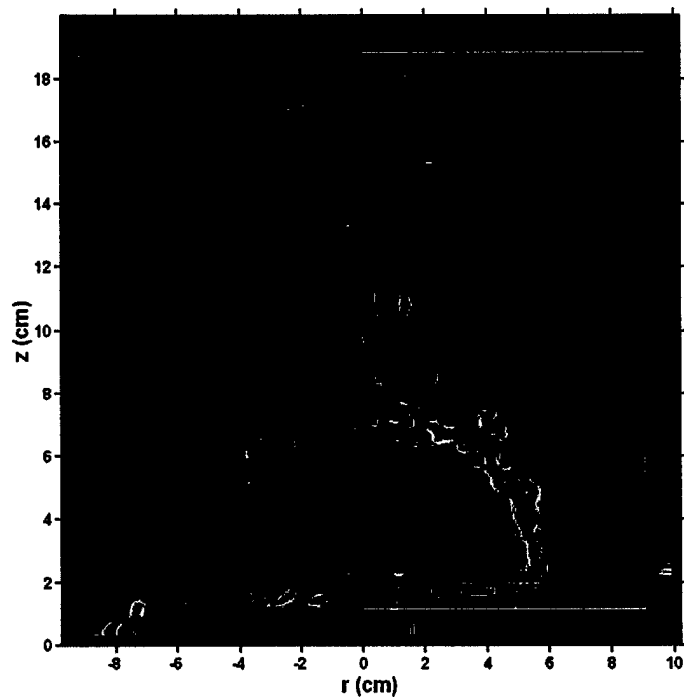
Figure 2.11. Sample region in which impulse was calculated from the vorticity field. The white line represents the enclosed region and the colored lines are vorticity contours.

3. Canopy in Steady Flow

3.1 Mean Canopy Diameter

A canopy in steady flow (*i.e.* steady descent) exhibits a "breathing" phenomenon in which the diameter of the canopy grows and shrinks. This quasi-periodic motion of the canopy was observed for all canopy sizes examined and quantified through the measurement of the maximum projected diameter, D_m. This behavior is also observed in full-scale parachute canopies. A typical time history of the maximum diameter and the force from the experiments is shown in Fig. 3.1. The mean behavior of the canopy diameter and force will be examined initially.

Since the edge of the canopy is not a smooth surface but has a scalloped geometry (see Fig. 2.5), the mean projected diameter, D_p, was estimated by from the side-view of the images through

$$D_p \approx 0.935 \cdot D_m \qquad\qquad 3.1$$

at each Reynolds number. The projected diameter is the equivalent diameter of a circle with the same area. Defining the projected diameter in this manner allows for a direct comparison with fundamental wake studies of disks and spheres.

The mean projected diameter was calculated from the temporal measurements of the maximum diameter and is shown in Fig. 3.2 for the range of Reynolds numbers and canopy sizes studied. The mean projected diameter remained constant over this range of Reynolds numbers $(Re_{Do} = 3.0\text{-}6.0 \times 10^4)$ at $D_p/D_o \approx 0.71$. Full-scale, solid cloth canopies maintain mean projected diameters of $D_p/D_o \approx 0.67\text{-}0.70$ (Knacke, 1992), which shows good correspondence with our scale model results. The *rms*-value of the amplitude of the oscillation is $D'_{rms}/D_p = 2.5\text{-}5.0\%$.

38

The automated image processing routines used to extract the canopy diameter also measured the mean canopy height, H. Normalizing the mean canopy height with the mean projected diameter shows that this ratio is constant at $H / D_p \approx 0.41$ over the range of Reynolds numbers examined (see Fig. 3.2). A sense of how the height varies with the diameter can be ascertained by calculating the correlation coefficient, (Taylor, 1997)

$$\rho_{x,y} \equiv \frac{\frac{1}{n} \sum_{i=1}^{n} (x_i - \mu_x)(y_i - \mu_y)}{\sigma_x \cdot \sigma_y} \qquad 3.2$$

where x and y represent the two variables to be correlated (in this case H and D_p), μ is the mean values of each variable, σ is the standard deviation of the variables, and the range of the correlation coefficient is $-1 \leq \rho_{x,y} \leq +1$. If $\rho_{x,y} = 0$, then the variables are uncorrelated while a correlation coefficient of +1 means they are perfectly correlated. Conversely, if $\rho_{x,y} = -1$, the variables are perfectly anti-correlated (*i.e.* when one variable increases the other variable decreases). The correlation coefficient between the canopy diameter and height is negative in Fig. 3.3; the canopy height shrinks while the diameter increases and vice versa. This behavior is expected since the stresses in the canopy fabric restrict the expansion of the canopy in each direction. The correlation of the diameter and height is reduced at higher Reynolds numbers. The correlation coefficient reduces from –0.9 to –0.5 as the Reynolds number increases from 3.0×10^4 to 6.0×10^4. Visual observations of the canopy indicate that an additional oscillation mode becomes apparent at the higher Reynolds numbers. An asymmetric oscillation of the canopy fabric traverses from one side of the canopy to the other. It appears as a moving wave through the canopy fabric. This mode reduces the correlation between the diameter and height.

39

3.2 Mean Drag Force

The mean force experienced by the canopy model was calculated from the temporal measurements of the force provided by the load cell. A force coefficient, C_F, was defined by

$$C_F = \frac{F}{q_o S_o} \qquad\qquad 3.3$$

where q_o is the dynamic pressure (corrected for blockage effects in the water tunnel) and S_o is the constructed surface area of the canopy. The mean C_F values are plotted in Fig. 3.4 as a function of the Reynolds number. A Reynolds number dependence is clearly seen as well as a geometric dependence. The drag coefficient for full-scale canopies with similar geometries (flat circular canopies with low material permeability) is in the range of 0.75-0.8 but these canopies generally operate at Reynolds numbers two orders of magnitude larger than those seen in these experiments. The larger canopy ($D_o = 30$ cm) has a drag coefficient that is approximately equal to that seen in full scale canopies even at this lower value of the Reynolds number. The discrepancy between the two canopies suggests that a transition might occur in the drag near this Reynolds number range.

Calculating the correlation coefficient between the diameter and the force shows the connection between the drag force and the reaction of the canopy geometry to it. The correlation coefficient is plotted in Fig. 3.5. A mild anti-correlation (*i.e.* a negative correlation) exists between the force and the diameter at lower Reynolds numbers. This suggests that as the canopy diameter shrinks from its maximum value, the force is increasing. It will be shown in a later section that the periodic nature of the diameter and the force is caused by the shedding of a vortex from the canopy. Therefore, it is

40

suggested that the peak force in a single cycle may be related to the shedding of the vortex ring from the canopy. However, almost no correlation exists at the higher Reynolds number. At these higher Reynolds numbers, the shedding of the vortices becomes less organized resulting in a reduction of the correlation between the canopy diameter (which is closely related to the vortex shedding) and the force.

As discussed in Section 1.4, the force the canopy experiences from the fluid can be related to two primary sources, namely a force associated with the unsteady potential flow and a force associated with the vorticity containing portion of the wake. The unsteady potential force component will be examined next.

The unsteady potential flow comes about due to the oscillations of the canopy geometry (*i.e.* the diameter and height) and the associated changes in the enclosed fluid volume in the canopy. This is true as long as the canopy is not decelerating (*du/dt* = 0). For the case of a fully inflated canopy, it is expected that the acceleration of the canopy would be small since the canopy is descending at a nearly constant speed. Therefore, the potential flow force should only be a function of the enclosed volume. It was shown in Eq. 1.11 that the unsteady potential flow generates a force proportional to the rate of change of the canopy volume,

$$F_p = k_p \rho U_\infty \dot{V} \qquad\qquad 3.4$$

where k_p is a proportionality constant and $\dot{V}$ is the time rate of change of the canopy volume. Since the volume of the canopy is cyclic in nature, the volume can be further decomposed into a mean volume, $\overline{V}$, and a fluctuating portion, V',

$$V = \overline{V} + V' \qquad\qquad 3.5$$

41

Due to the periodic nature of the geometry oscillations, the mean volume is a constant. Therefore, any force generated by this unsteady behavior comes strictly from the fluctuating portion of the volume; more specifically, the time derivative of the fluctuating volume. The time derivative of the volume fluctuations are both positive and negative in amplitude with a zero mean value. So in order to quantify the contribution that unsteady potential force has on the canopy dynamics, the *rms*-value of the time derivative of the volume fluctuations was calculated, $(\dot{V}')_{rms}$. Therefore, the fluctuating force due to the unsteady potential flow was calculated as

$$(F_p)_{rms} = k_p \rho U_\infty (\dot{V}')_{rms}.$$ 3.6

The volume of the canopy was estimated from the cross-sectional area and shape of the canopy in the images (see Section 2.3). The time derivative of the volume was calculated by using a central differencing scheme from which the *rms*-value of the fluctuations was determined. The unsteady potential force as a function of the Reynolds number is plotted in Fig. 3.6 assuming a value of unity for the proportionality constant ($kp = 1$) in Eq. 3.6. As is evident in Fig. 3.6, the unsteady potential flow amounts to 10-20% of the measured force fluctuations, F'_{rms}, and only ~ 10% at the higher Re. These results show that the majority of the fluctuating force exerted on the canopy is caused by the viscous wake.

3.3 Near Wake Characteristics

The breathing of the canopy is a result of the interactions with the flow field in the near wake of the canopy, provided that canopy is flexible enough to respond to the flow. The velocity and vorticity fields show that the breathing corresponds with the shedding of vortical structures from the canopy. Figure 3.7 shows the vorticity field in the near wake

42

over one shedding cycle. It is clear that the flow is separated at the canopy skirt. When the canopy reaches its minimum diameter (Fig. 3.7a), a distorted vortex ring is seen to have just shed from the canopy. This vortex is convected downstream into the turbulent wake and becomes more disorganized and distorted as the vortex decays. At the canopy skirt, a shear layer rolls-up into another vortex ring over the next few image sequences (Fig. 3.7b-d). While this vortex ring is forming, the canopy diameter also increases until the canopy reaches its maximum diameter (Fig. 3.7d). The process of forming the vortex generates a low pressure region near the canopy skirt which draws the canopy out to its maximum diameter. With the new vortex ring formed, the shear layer from the canopy skirt feeds the vortex with additional vorticity until the vortex separates from the shear layer and canopy and is convected downstream (Fig. 3.7e-f). The convection of the vortex ring also removes the low pressure region at the canopy skirt and moves it farther downstream of the canopy which results in the canopy diameter shrinking back to its minimum diameter (Fig. 3.7f).

A phase averaged vorticity field was calculated by locking into the canopy breathing frequency. A sample of the phase averaged data is shown in Fig. 3.8 for a 15 cm canopy at a freestream velocity of 20 cm/s. It is clear from these images that a vortical structure is seen to shed from the canopy and is conveyed downstream with the shedding cycle repeating at a frequency of 1 Hz. A qualitative verification of the shedding frequency can be made by observing that vortex ring is located in the same downstream position in both Figs. 3.8a and 3.8h which have a time separation of 1 s.

A parachute canopy in steady flow also exhibits behavior in some aspects analogous to those traditionally seen with rigid bluff bodies (such as disks or spheres).

43

The time-averaged velocity and vorticity field in the wake of the canopy, averaged over a 1000 (~67 s) instantaneous measurements of the fields (Fig. 3.9), shows a momentum deficit exists in the wake which is characteristic of turbulent three-dimensional wakes of axisymmetric bluff bodies. The profile of the axial velocity, u_z, and the radial velocity, u_r, at three different downstream locations is shown in Fig. 3.10a and the vorticity is shown in Fig. 3.10b. The variation of the time-averaged axial velocity across the wake of the canopy is clearly seen, with reverse flow along the centerline of the wake. This velocity profile results in a momentum deficit in the wake that contributes to the drag of the canopy. The radial velocity indicates entrainment of the freestream velocity in the shear layers into the wake region from both sides of the canopy at the two farthest downstream locations. The majority of the vorticity is confined to the shear layers near the canopy skirt and decays rapidly. These characteristics are seen in rigid bluff bodies, however, the flexible nature of the canopy introduces some unique features.

3.4 Breathing Frequency

The periodic nature of the canopy motions (see Fig. 3.1) suggests that a spectral analysis of the data would allow for the identification of the dominant breathing frequencies. The spectral content of the data was uncovered by the application of the Fast Fourier Transform (FFT). The plots in Fig. 3.11 show the maximum canopy diameter and the frequency content of the diameter measurement for a 15 cm canopy at a freestream velocity of 30 cm/s. The spectrum shows a single dominant frequency at $f = 1.5$ Hz. We define a non-dimensional breathing frequency based on the mean projected diameter and the freestream velocity as

$$\frac{f \cdot D_p}{U_\infty}.$$
3.7

Observations of the spectrum for all the different canopies and range of freestream velocities, show that a single dominant frequency exists. The non-dimensional frequency remains very nearly constant at a value of 0.56 ± 0.03 across the Reynolds numbers and geometries examined (see Fig. 3.12). This is the dominant canopy breathing frequency described in section 3.3. The breathing (or the aeroelasticitic response) of the canopy is contingent upon the canopy material being flexible enough to respond to the flow field. If the canopy were rigid, the canopy would not breathe and the shedding characteristics would be probably different. The canopy breathing results in the flow separation point (the canopy skirt) moving in the flow field.

The spectral analysis of the force measurements made with the load cell generates a complex spectrum (as shown in Fig. 3.13). However, a frequency corresponding to the dominant frequency observed in the diameter measurements was also seen in the frequency spectrum of the force (Fig. 3.14). Non-dimensionalizing this frequency also results in a 0.56 ± 0.03 value. As will be shown below, this frequency corresponds to the periodic shedding of vortices at the edge of the canopy skirt.

The PIV measurements create an array of regularly spaced velocity vectors throughout the flow field. By extracting or "probing" these measured velocity vectors at various points in the wake, a means for relating the fluid mechanics of the canopy wake to the canopy geometry and force can be established. Table 3.1 lists the probe locations utilized in the velocity fields. At these points, the radial velocity, u_r, was extracted. A sample of the radial velocity at points A for the 15.2 cm canopy is shown in Fig. 3.15.

45

Table 3.1. Velocity probe locations.

D_o (cm)	Location	r/D_p	z/D_p
15.2	A	±0.69	0.25
15.2	B	±0.81	1.0
15.2	C	0.81	1.59
30.5	A	0.69	0.25
30.5	B	0.97	0.97

The large fluctuation in the radial velocities appear to be quasi-periodic. A sample of the spectral analysis of the radial velocities is shown in Fig. 3.16. By defining a Strouhal number as,

$$St \equiv \frac{f \cdot D_p}{U_\infty} \qquad\qquad 3.8$$

a dominant frequency at $St = 0.54 \pm 0.04$ occurs across the range of Reynolds numbers examined, Fig. 3.17. However, another frequency seems to appear around a Strouhal number of $0.3 - 0.4$ at points further downstream of the canopy (Figs 3.16b-c). Neither of these frequencies have been observed in the past studies of disks or spheres (Balligand & Higuchi, 1993; Berger *et al.*, 1990; Fuchs *et al.*, 1979). Three dominant frequencies are classically associated with a stationary disk. The primary frequency is associated with a helical mode for the vortex structure. This mode has a Strouhal number of 0.134 but has been observed beyond ~3-4 diameters downstream (Berger *et al.*, 1990). Our studies focused on a region 1.5 diameters downstream but we see evidence that this mode started to form in our experiments (Fig. 3.16c) at the farthest downstream locations. Another mode of the disk has a Strouhal number of 0.05 which corresponds to the axisymmetric oscillation of the recirculation region immediately behind the disk. We see no evidence of this from our velocity probe data. And finally, a high frequency shear layer instability

46

was also seen in the disk studies of Berger *et al.* (1990) at $St = 1.62$. Again, we did not find any evidence of these structures. This is possibly due to the spatial resolution of our velocity field being too small.

A qualitative observation of the vortex formation in the PIV data fields shows that vortex rings form symmetrically around the canopy at lower Reynolds numbers. Once the vortex is shed from the canopy and is conveyed downstream, the symmetry of the vortex begins to degrade. The vortex ring becomes twisted and disorganized in the wake of the canopy. The initial symmetry can be quantified by analyzing the radial velocity of the wake flow in the immediate vicinity of the canopy and at positions farther downstream. Calculating the correlation coefficient, between the two symmetric probe points listed in Table 3.1 quantifies the symmetry of the vortex. The results of the correlation coefficient calculations (Fig. 3.18) suggests that the vortex is initially symmetric immediately downstream of the canopy (points **A**) at the lower Reynolds number. As the vortex is conveyed farther downstream (points **B**), the correlation coefficient is reduced indicating that the vortex is becoming disorganized. This behavior confirms our qualitative observations of the wake behavior. At a Reynolds number of 6.0×10^4, the behavior of the vortex is different. Qualitative observations of the vortex shedding, shows that the vortex formation occurs symmetrically but once shed from the canopy, the vortex quickly becomes distorted. This is reflected in the fact that almost no correlation exists between the symmetric probe points at either location.

The vortex core location was measured in the vorticity field by locating the center of the vortex. The position of a series of shed vortex rings is plotted in Fig. 3.19. The position of the vortex ring was measured separately on each side of the canopy. The

47

vortex ring is confined to a region on the outer extreme of the canopy initially at which point the vortex ring diameter slightly grows and becomes more disorganized as the vortex ring moves farther downstream. The growth is evident by the increase in the width of the mean vortex position at the locations further downstream. And the disorganization is apparent by observing the increased scatter of the vortex position again at the locations farther downstream.

A sample of the axial vortex position is shown in Fig. 3.20. The plot shows the periodic shedding of a vortex. A saw tooth pattern in the vortex downstream position is seen. This comes about since an individual vortex was only tracked until a new vortex formed near the canopy skirt at which point the new vortex was tracked. The linear portion of the saw tooth pattern shows that the vortex is conveyed downstream at a nearly constant celerity. The celerity of the vortex was calculated from the average slope of the linear portions of the position plot. The average celerity utilized the slope calculated from both sides of the canopy and from all shedding cycles. The celerity of the vortex rings (normalized by the freestream velocity) over the range of Reynolds numbers examined is plotted in Fig. 3.21 where the error bars represent the standard deviation of the measurements. The normalized celerity remains constant at a value of $u_c/U_\infty = 0.41 \pm 0.02$ across the range of geometries and Reynolds numbers studied.

A spectral analysis of the vortex downstream position was performed and a sample of that analysis is shown in Fig. 3.22. Again a dominant frequency was identified that corresponded to the vortex shedding frequency. The Strouhal number from this analysis is plotted in Fig. 3.23 with a mean value of $St = 0.54 \pm 0.04$ which corresponds very well with our previous results. Calculating the correlation coefficient between the

48

vortex location on the right and left sides of the canopy shows how symmetric the vortex is shed from the canopy. The correlation coefficient is plotted in Fig. 3.24. The vortex is initially shed symmetrically from the canopy at the lower Reynolds number but as the Reynolds number increases the symmetry of the shedding vortex decreases. This behavior was also seen in the velocity probe measurements shown in Fig. 3.18.

In closing, it has been shown that the breathing phenomena a canopy experiences while in steady descent is associated with vortex shedding. The shedding frequency corresponds to a Strouhal number of $St = 0.54 \pm 0.04$ while the non-dimensional breathing frequency of the canopy is 0.56 ± 0.03. Also, it was shown that the unsteady potential flow contributes about 10% of the fluctuating drag at the higher Reynolds numbers in our study.
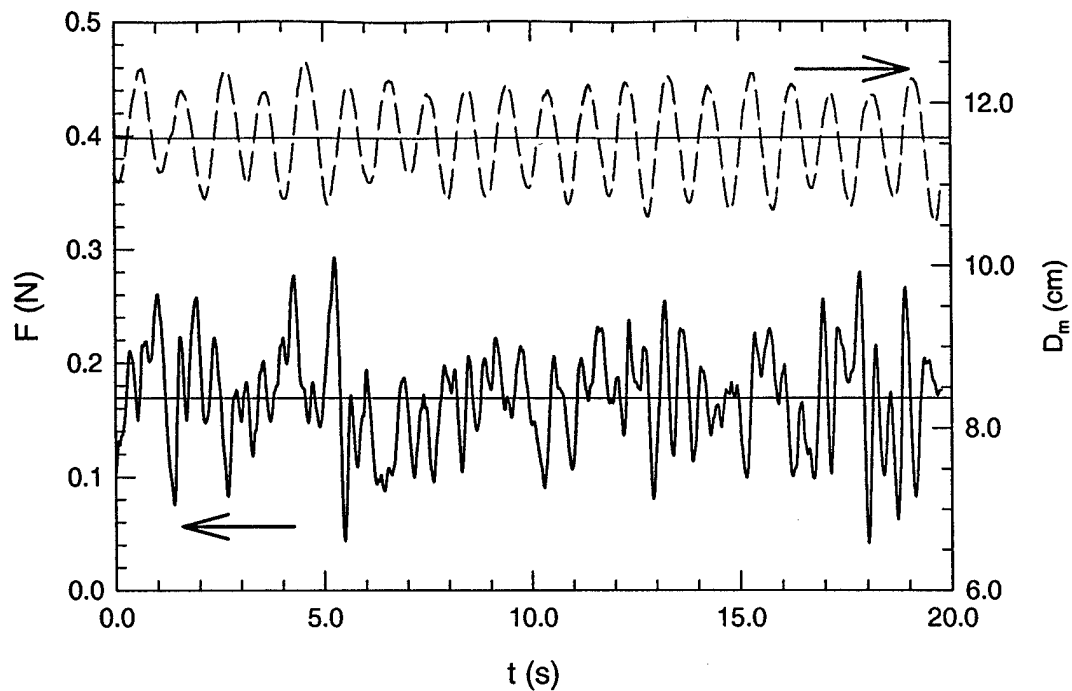
Figure 3.1. Maximum diameter and force measurements for a D_o = 15.2 cm canopy with U_∞ = 20 cm/s.
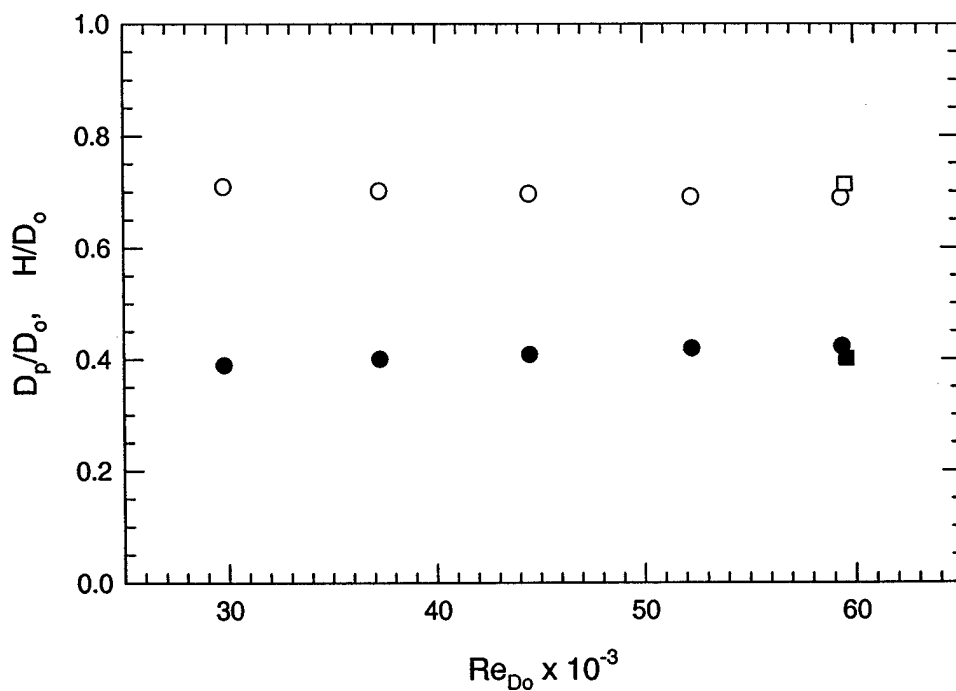
Figure 3.2. Normalized mean canopy projected diameter (hollow symbols) and mean canopy height (solid symbols). The round symbols represent the 15 cm canopy and the square symbol represents the 30 cm canopy.

50
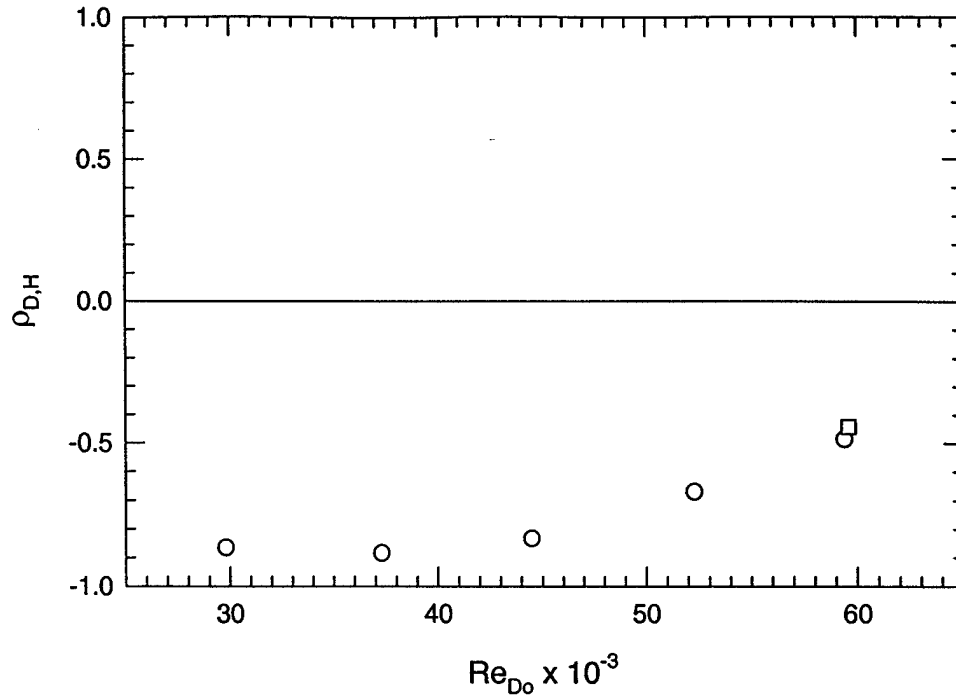
Figure 3.3. Correlation coefficient between the canopy diameter and height. The round symbols represent the 15 cm canopy and the square symbol represents the 30 cm canopy.
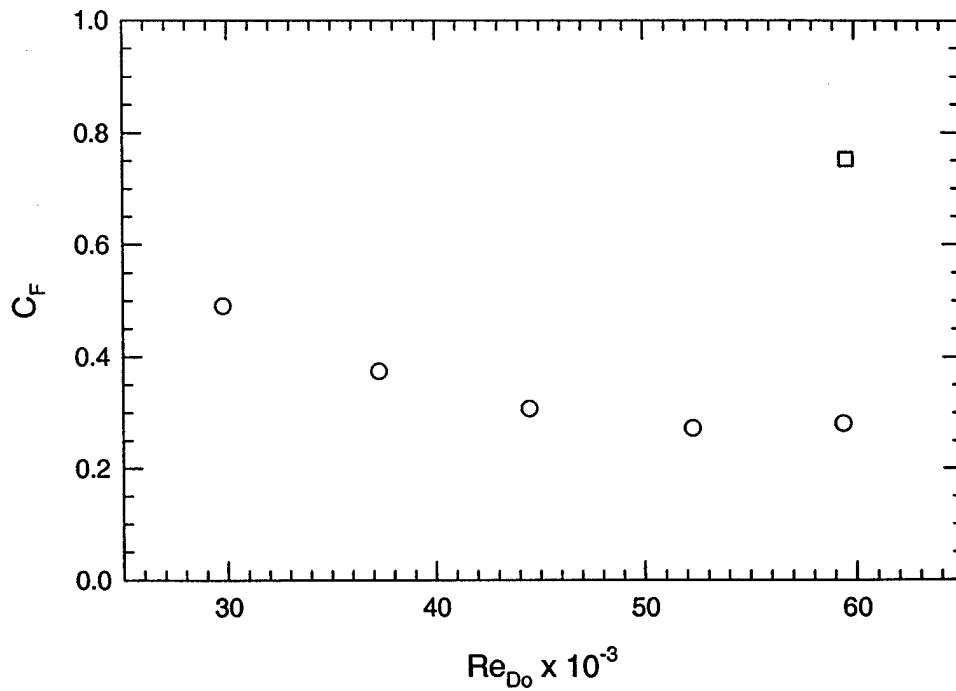
Figure 3.4. Force coefficient for canopy. The round symbols represent the 15 cm canopy and the square symbol represents the 30 cm canopy.
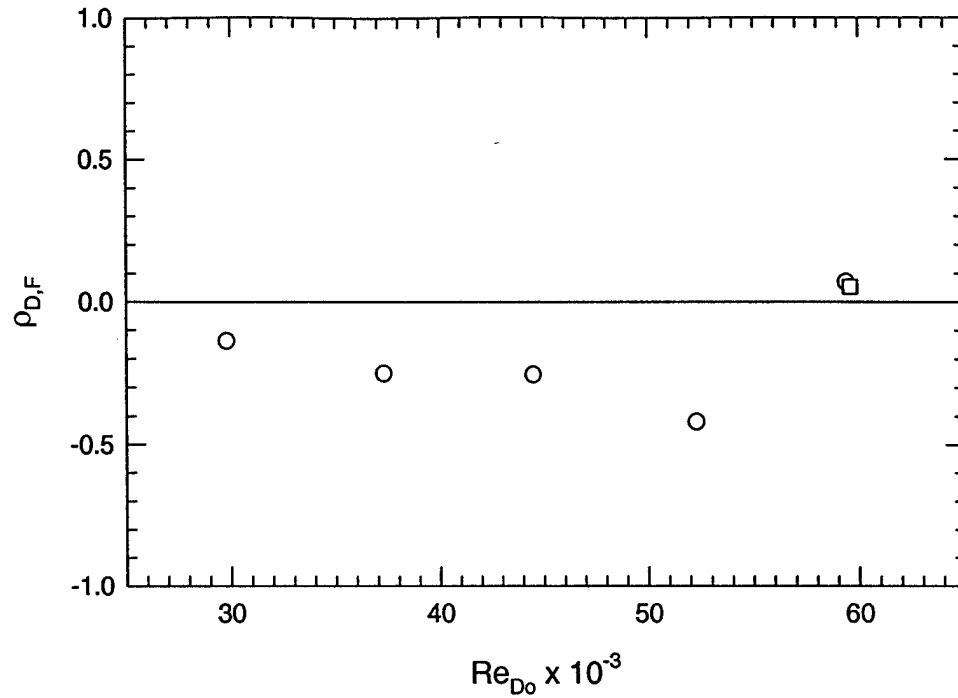
Figure 3.5. Correlation coefficient between the canopy diameter and force. The round symbols represent the 15 cm canopy and the square symbol represents the 30 cm canopy.
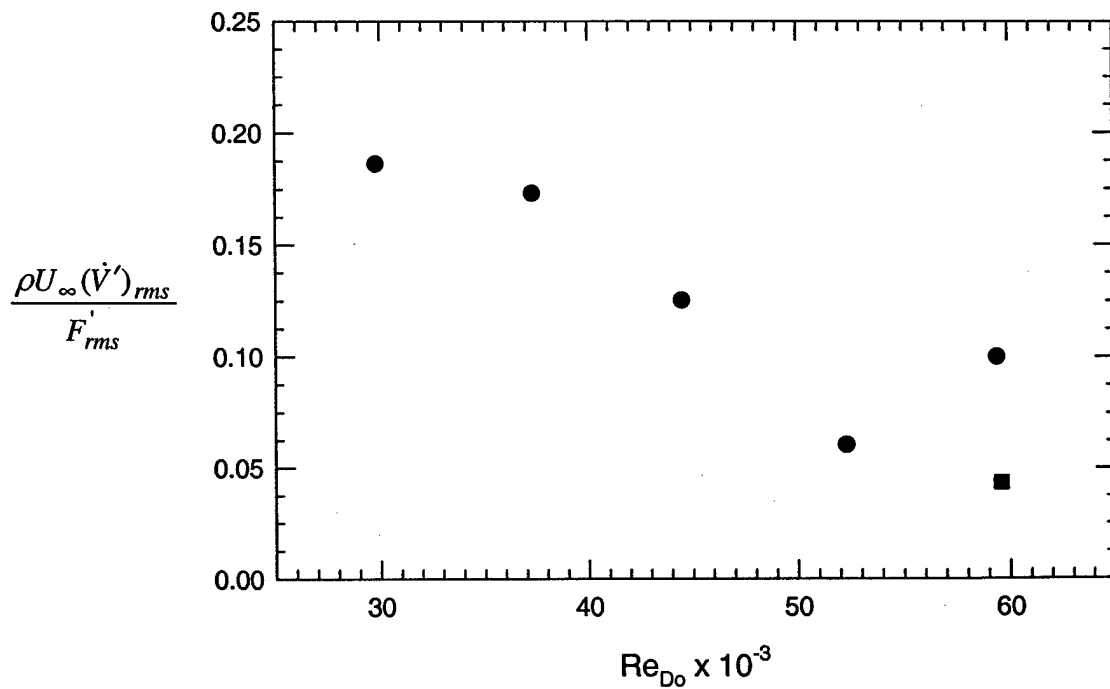

Figure 3.6. Fluctuating component of the unsteady potential flow. The round symbols represent the 15 cm canopy and the square symbol represents the 30 cm canopy.
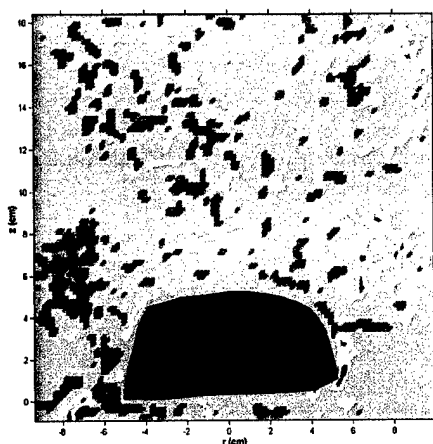
a) $t = 0$ ms (minimum canopy diameter)   b) $t = 200$ ms
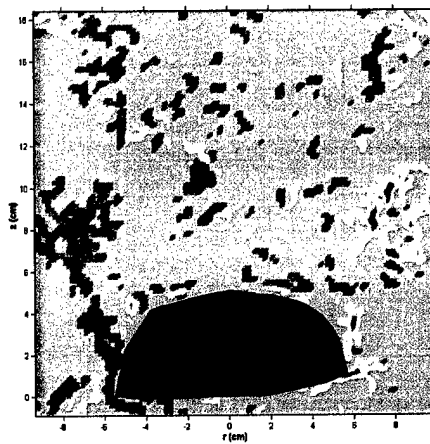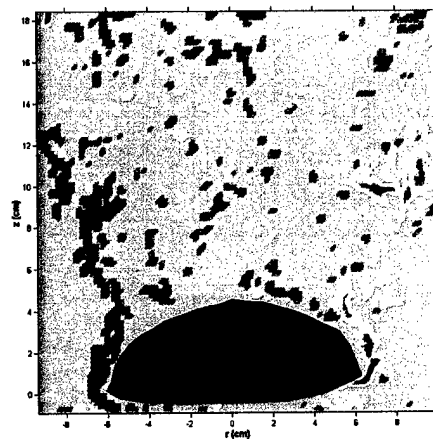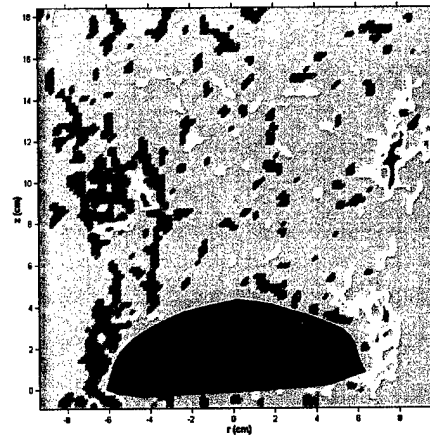
c) $t = 400$ ms   d) $t = 533$ ms (maximum canopy diameter)
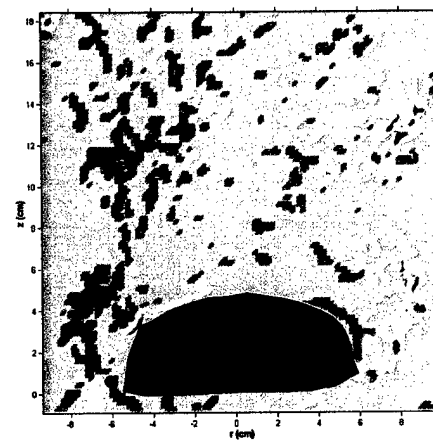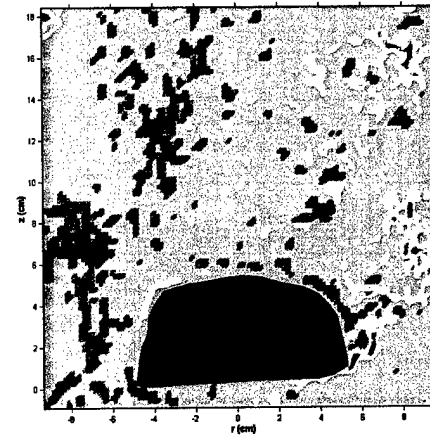
e) $t = 800$ ms   f) $t = 1067$ ms (minimum canopy diameter)

Figure 3.7. Vorticity field showing vortex formation during canopy breathing (image of canopy has been superimposed over the vorticity field).

53
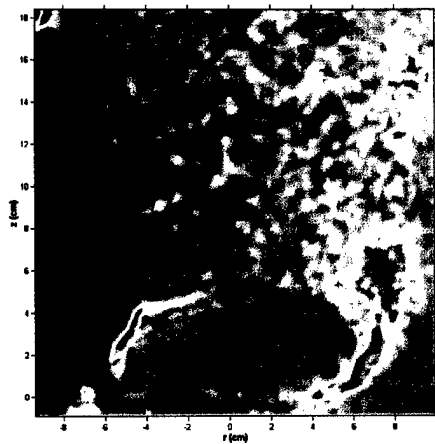
a) $t = 0.00$ s
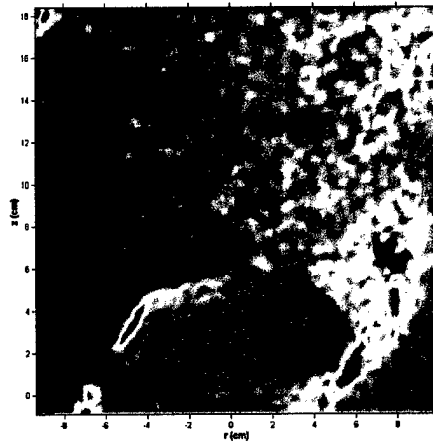
b) $t = 0.13$ s
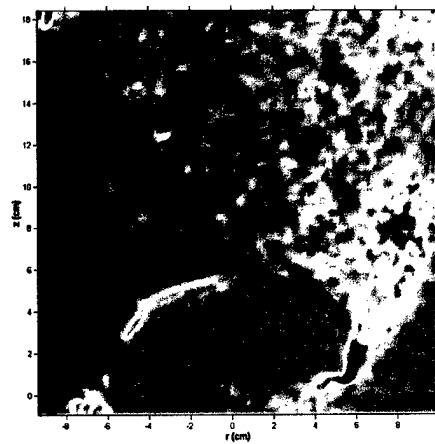
c) $t = 0.27$ s
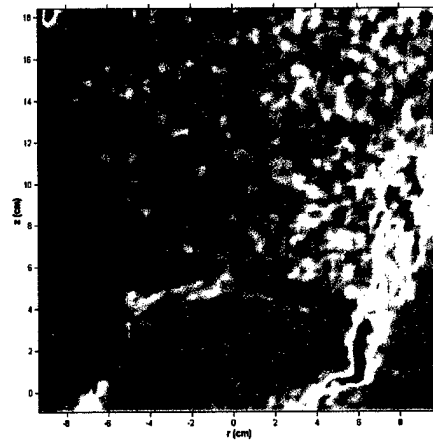
d) $t = 0.40$ s
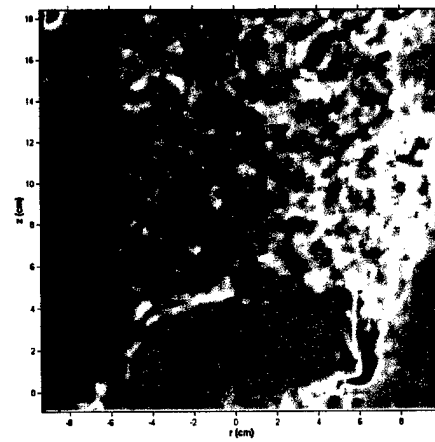
e) $t = 0.53$ s
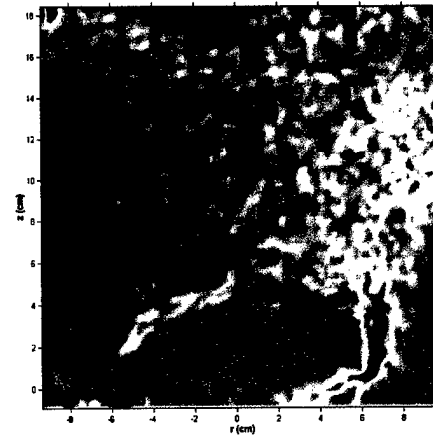
f) $t = 0.67$ s

Figure 3.8. Phased average vorticity field for a 15 cm canopy at 20 cm/s.

54
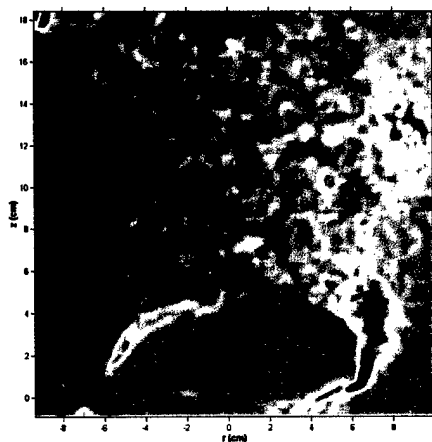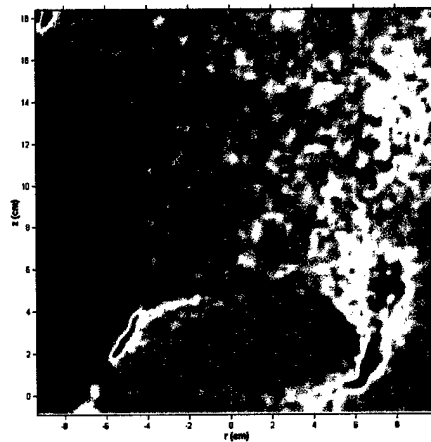
g) $t = 0.80$ s   h) $t = 0.93$ s

Figure 3.8. continued.
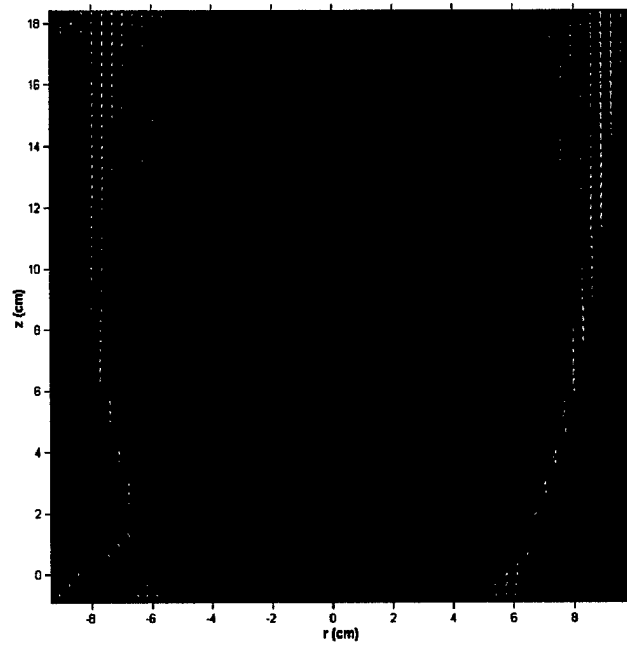
a)
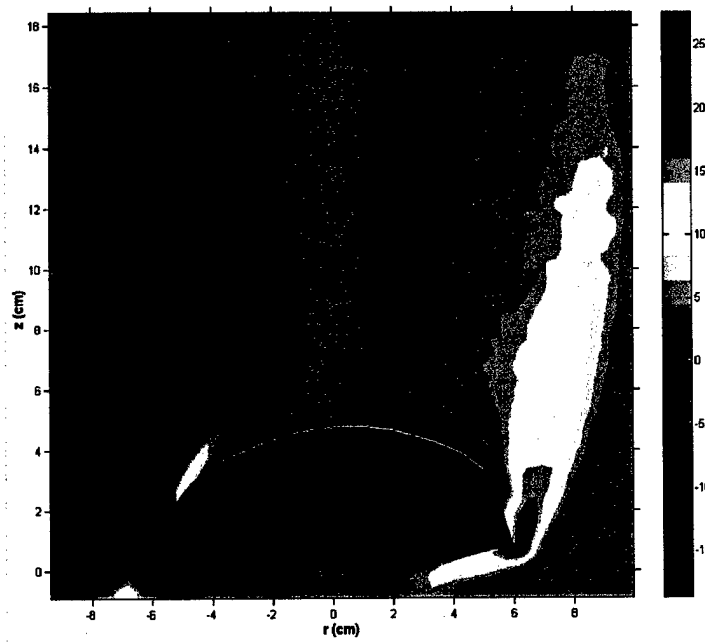
b)

Figure 3.9. a) Mean velocity field and b) mean vorticity field in the wake of a canopy in steady flow, $D_o = 15.2$ cm and $Re_{Do} = 3.0 \times 10^4$. An image of the canopy at its mean diameter has been super-imposed over the velocity field.
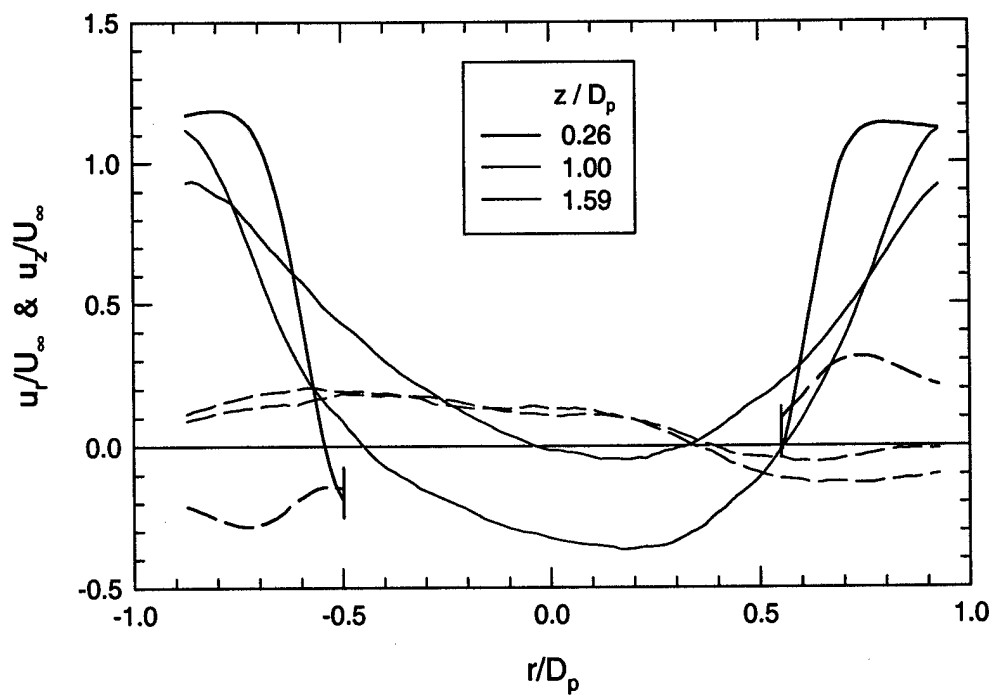
a)
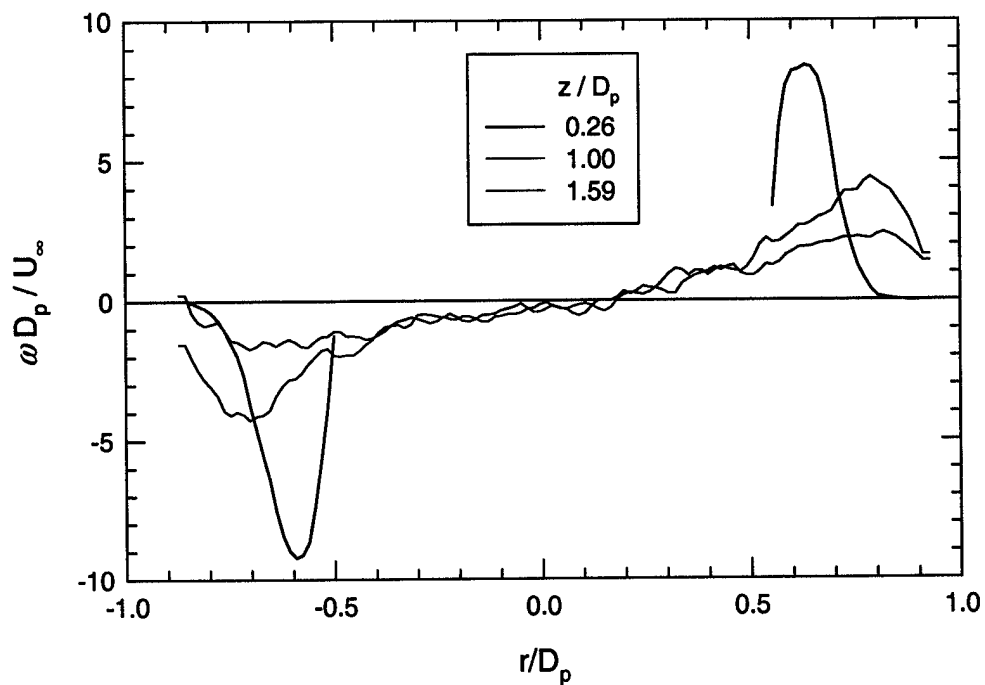
b)

Figure 3.10. a) Mean axial (solid lines) and radial (dotted lines) velocity profiles and b) mean vorticity profiles at three downstream locations.
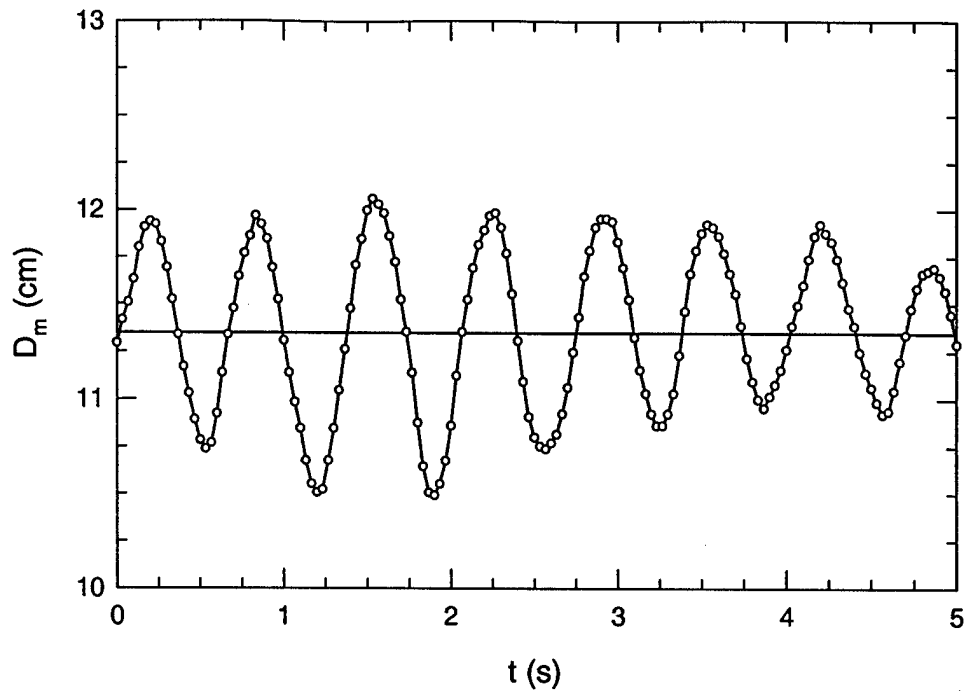
a)
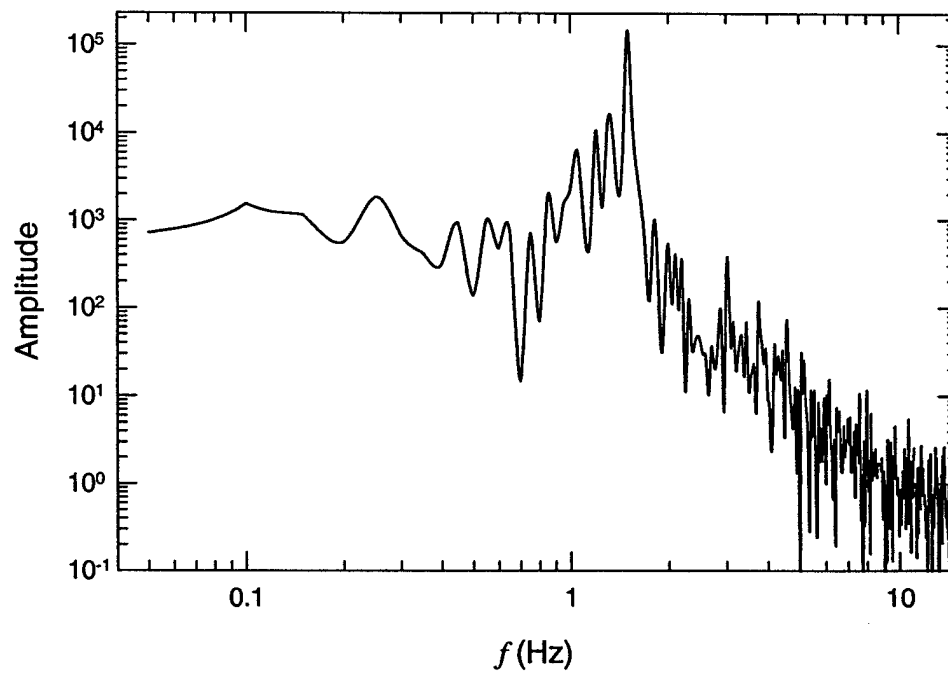
b)

Figure 3.11. a) The maximum projected canopy diameter and b) spectral content of the diameter fluctuations for a 15 cm canopy at a freestream velocity of 30 cm/s.
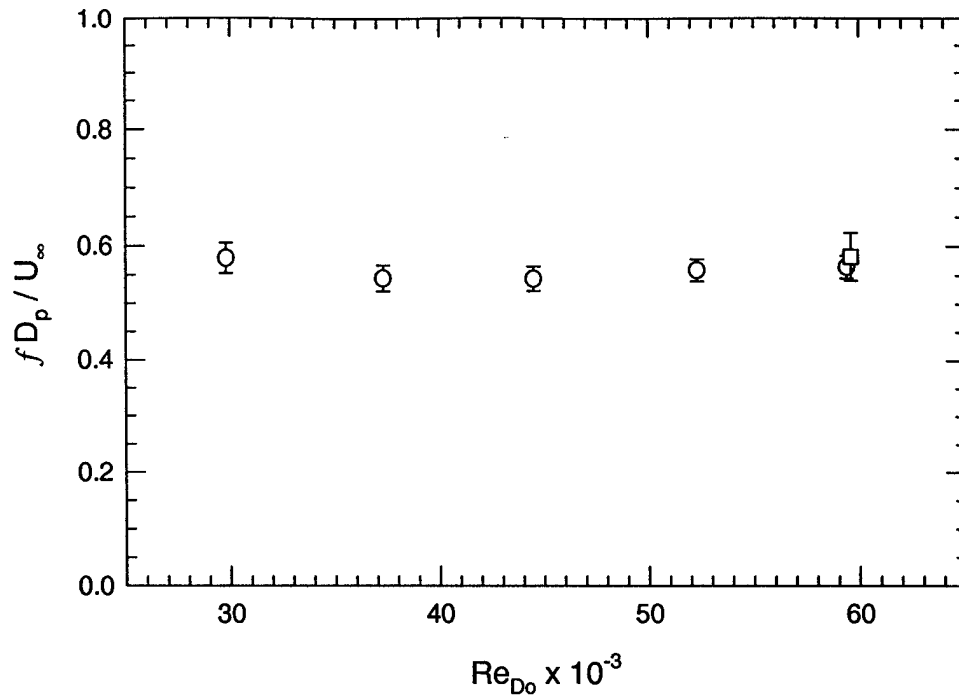
Figure 3.12. Dominant frequency of the canopy motions as a function of Reynolds number. The round symbols represent the 15 cm canopy and the square symbol represents the 30 cm canopy.
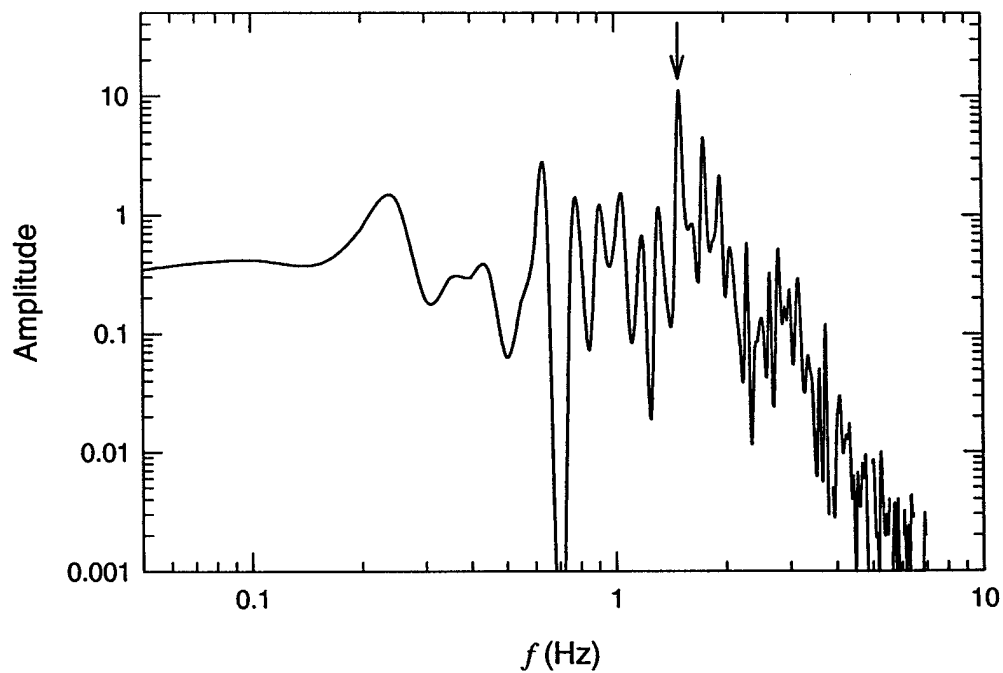
Figure 3.13. The spectral content of the darg force for a 15 cm canopy at 30 cm/s.

59
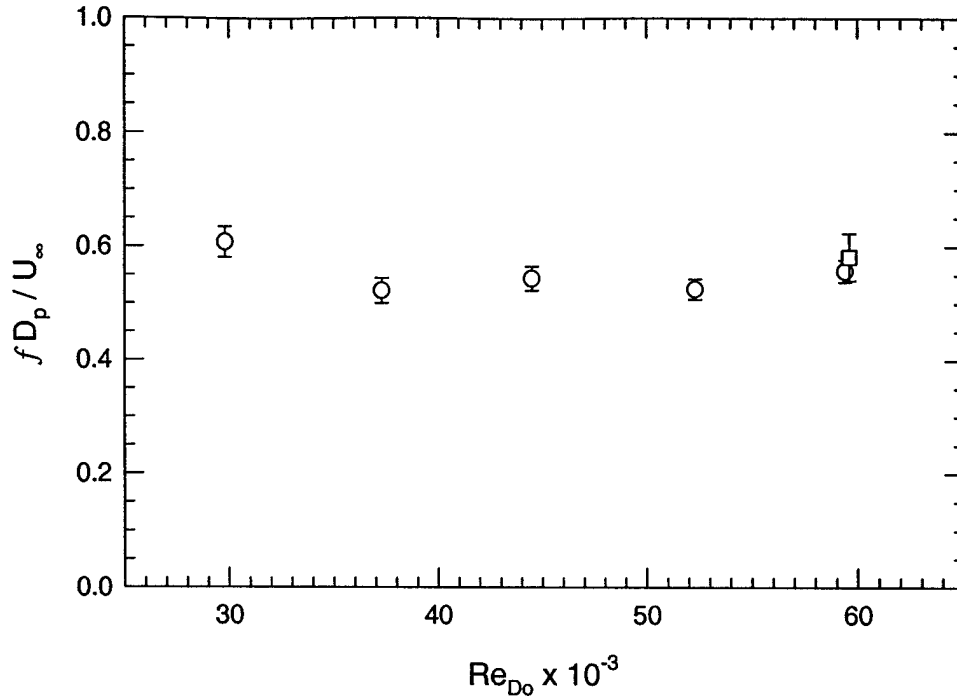
Figure 3.14. Frequency in the force measurements corresponding to the dominant frequency in the diameter measurements. The round symbols represent the 15 cm canopy and the square symbol represents the 30 cm canopy.
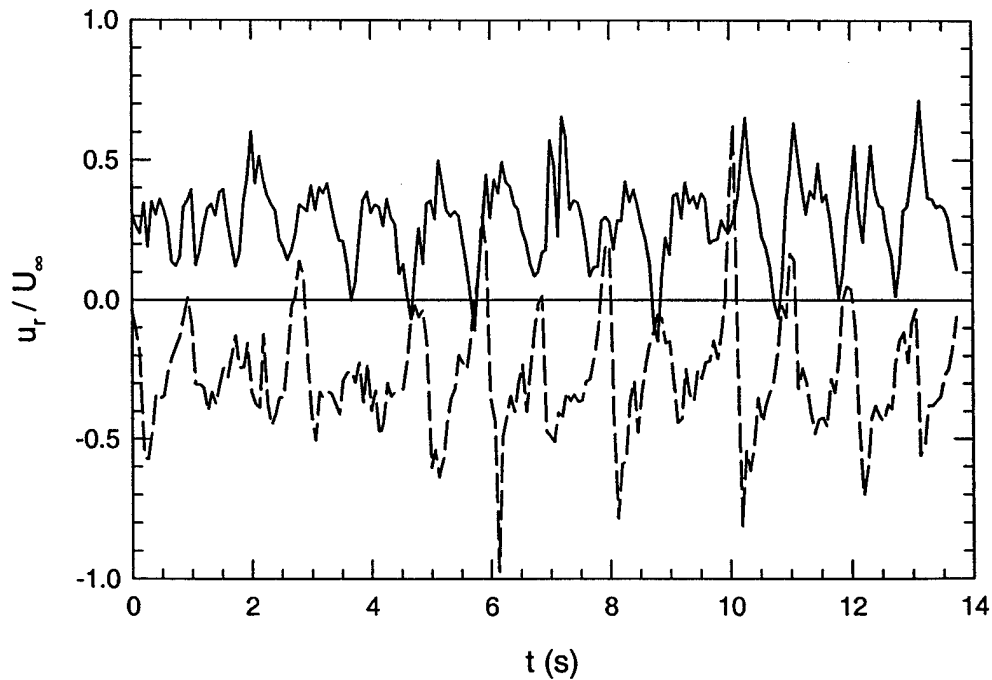
Figure 3.15. Radial velocities at points **A** (z/D_p = 0.25; r/D_p = 0.69 for the solid line and r/D_p = -0.69 for the dashed line) for the 15.2 cm canopy at Re_{Do} = 3.0 × 10⁴.
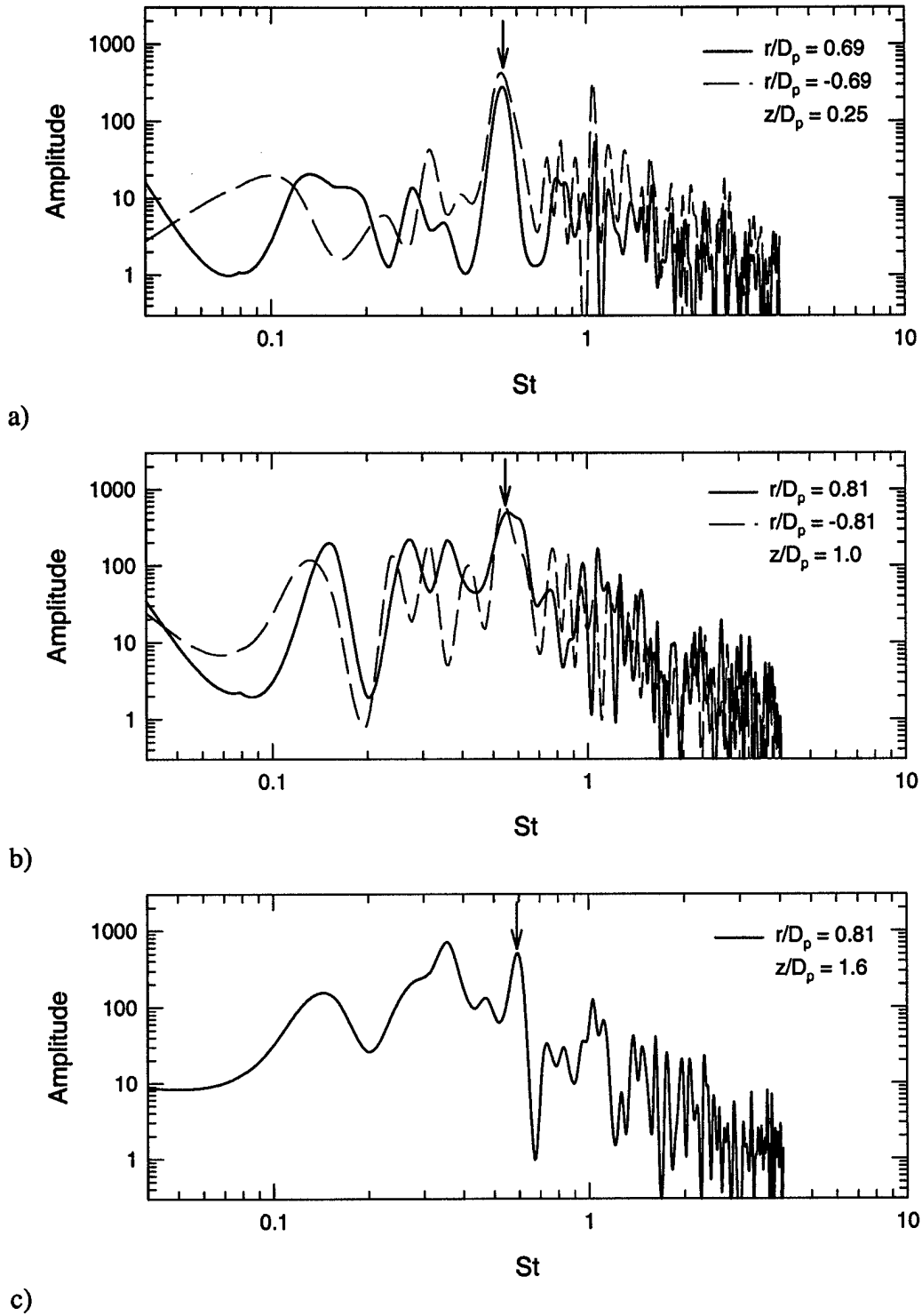
Figure 3.16. Frequency spectrum of radial velocity at a) points **A**, b) points **B**, and c) point **C** for the 15 cm canopy at $Re_{Do} = 3.0 \times 10^4$.
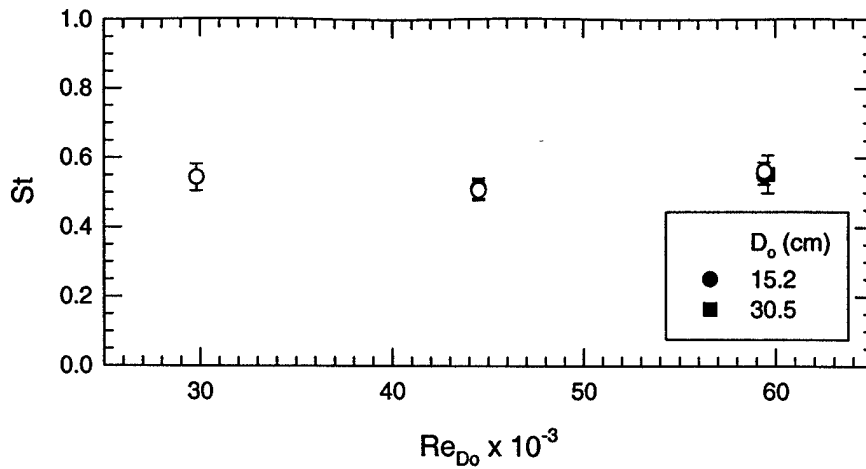
a)
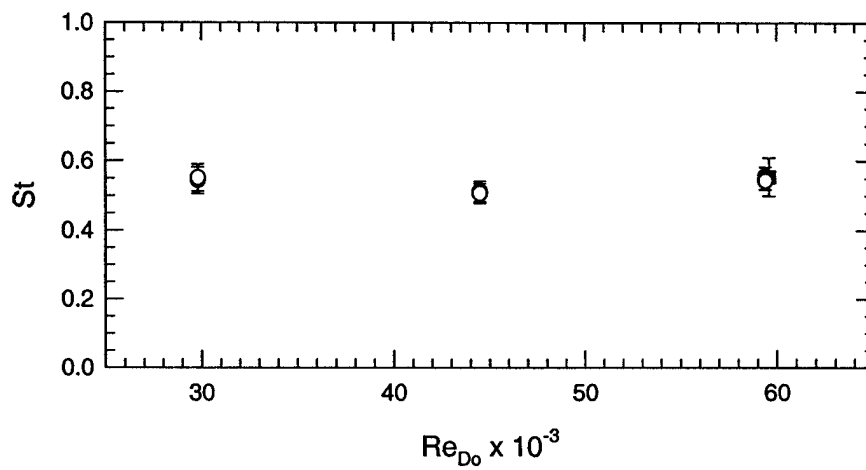
b)
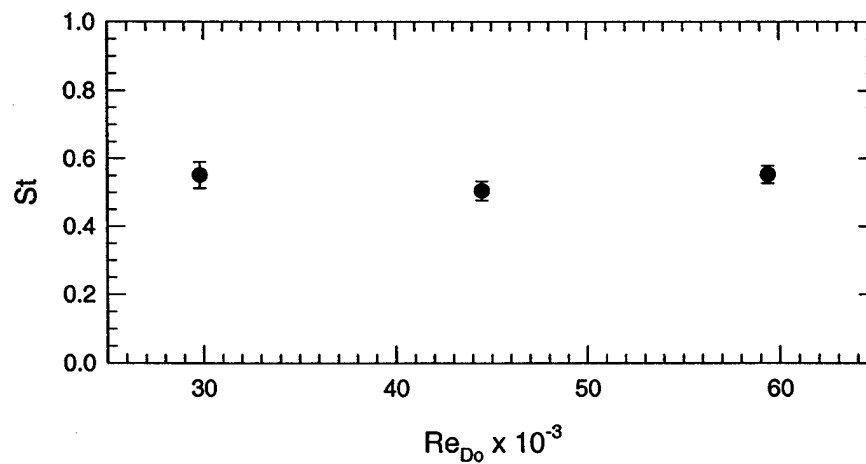
c)

Figure 3.17. Strouhal number of the radial velocity at a) points **A**, b) points **B**, c) points **C** listed in Table 3.1. The solid symbols represent the positive radial distances and the hollow symbols represent the negative radial distances.
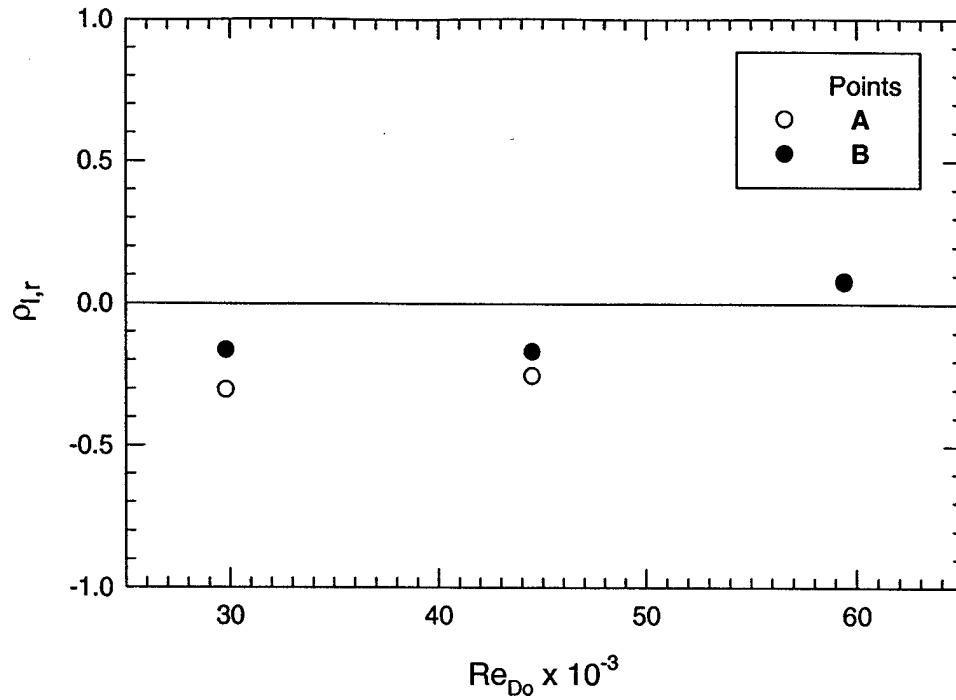
Figure 3.18. Correlation between symmetric radial velocity probe points for the 15.2 cm canopy.
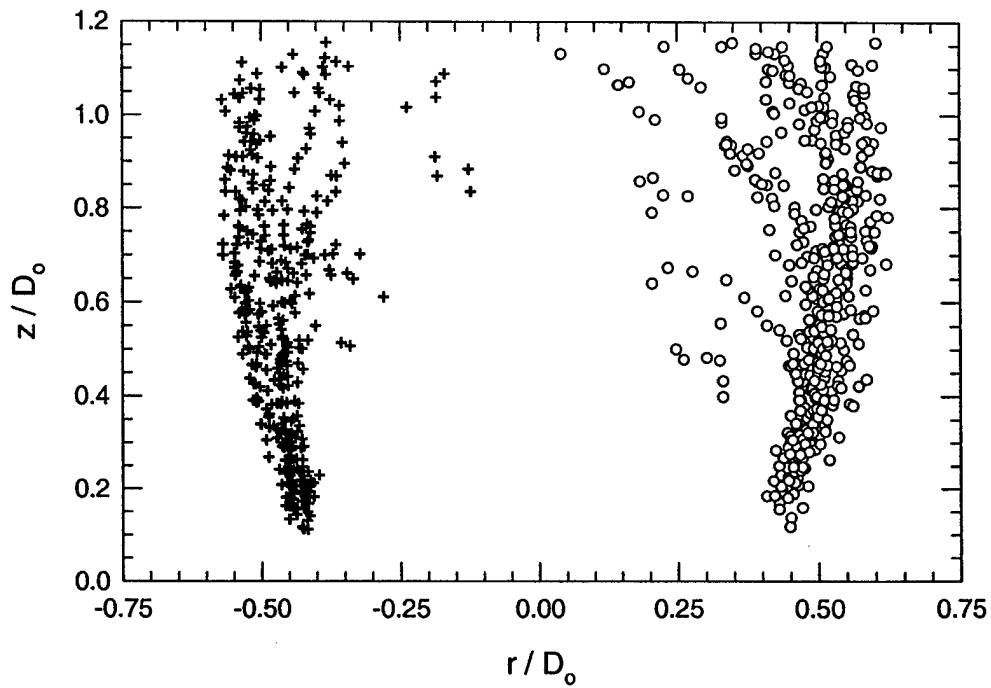
Figure 3.19. The vortex ring location over 14 shedding cycles. The round symbol is the location of the vortex on the right side of the canopy and the "+" symbol is the location on the left side of the canopy.
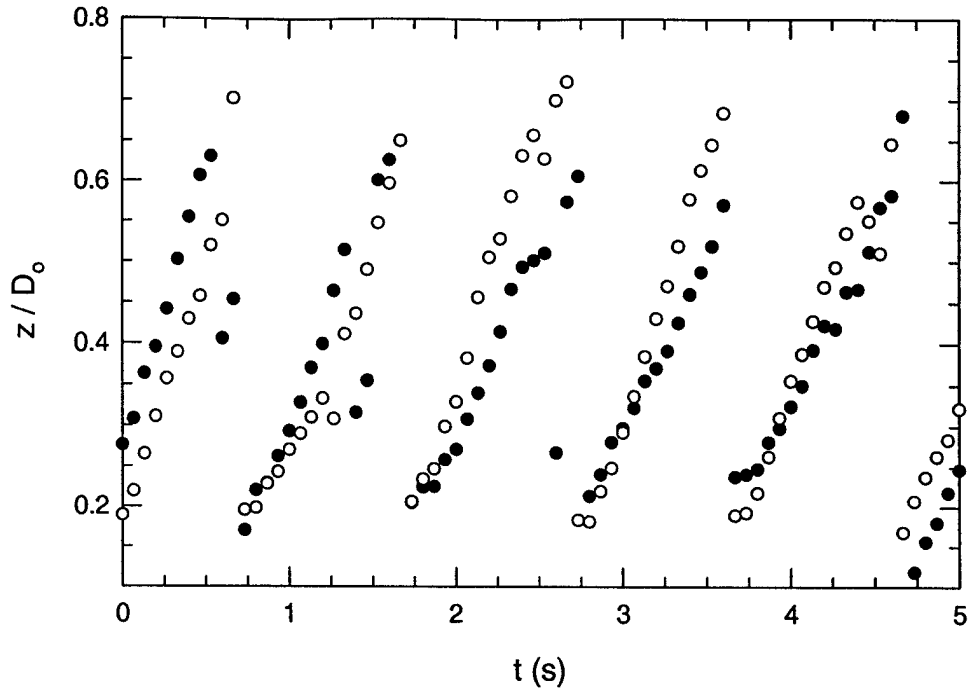
Figure 3.20. Downstream location of the vortex core. The filled symbol represents the vortex shed from the right side of the canopy and the hollow symbol represents the vortex shed from the left side of the canopy.
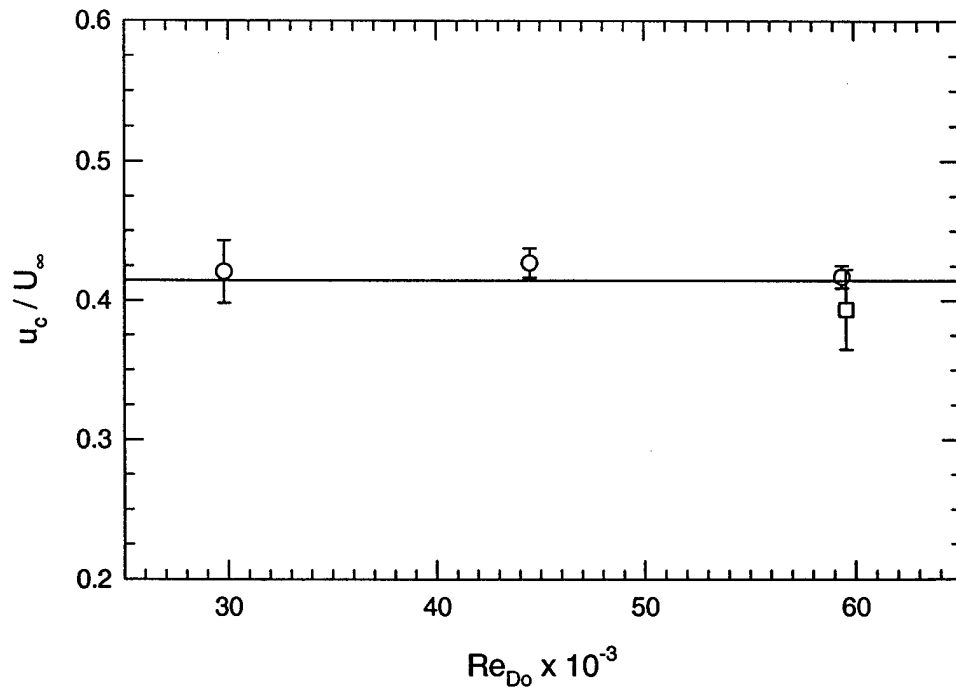
Figure 3.21. Celerity of the shed vortex over the range of Reynolds numbers examined. The round symbol represents the 15 cm canopy and the square symbol represents the 30 cm canopy.
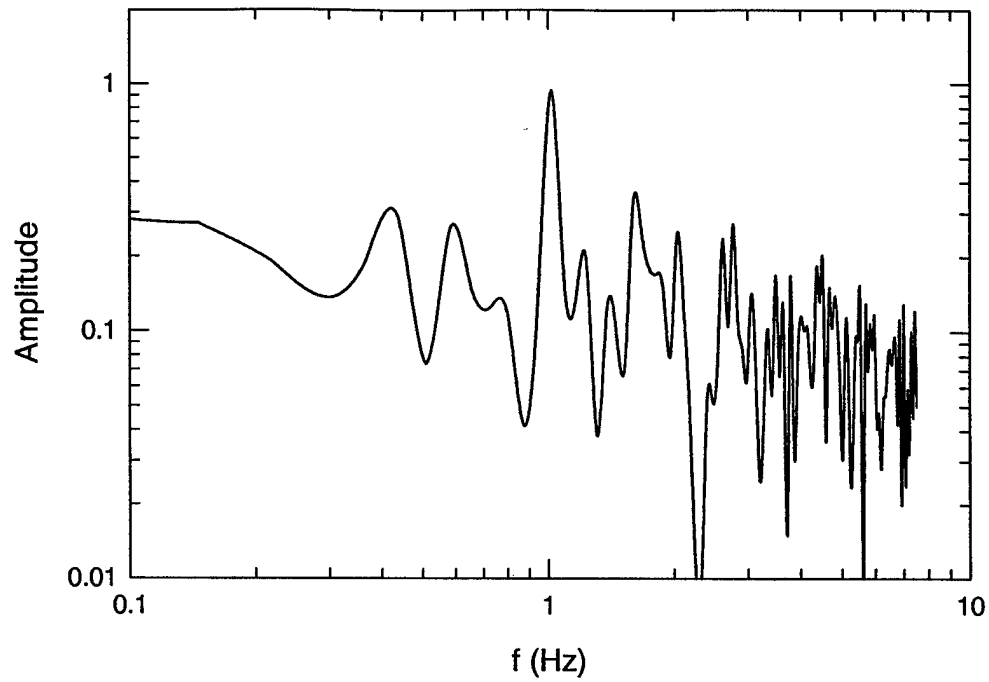
a)
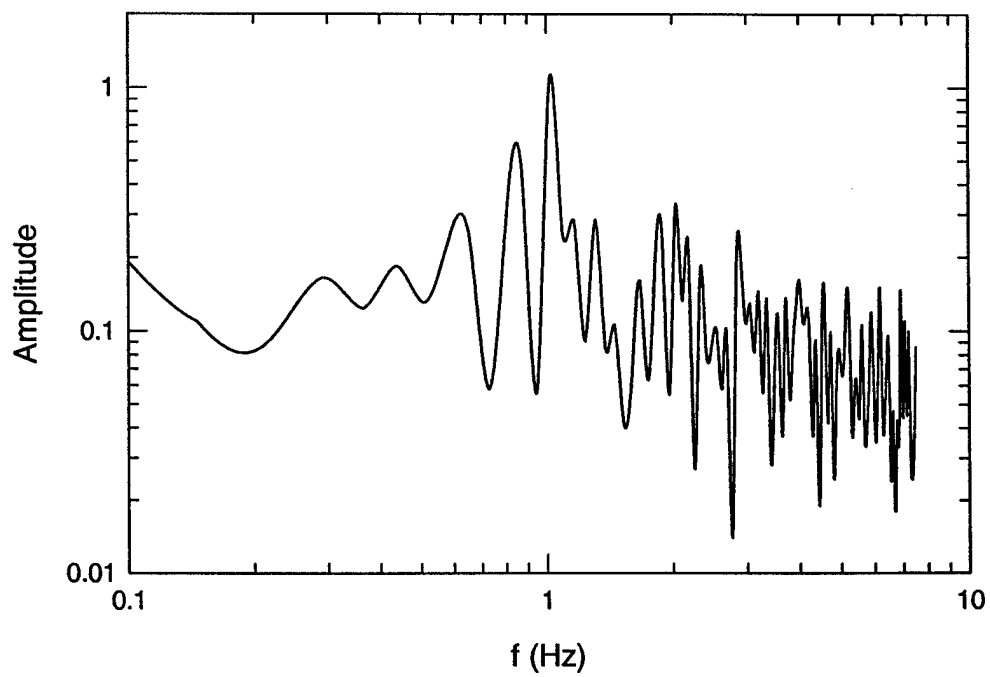
b)

Figure 3.22. The shedding frequency spectrum measured from the vortex tracking data; a) right side and b) left side of canopy.
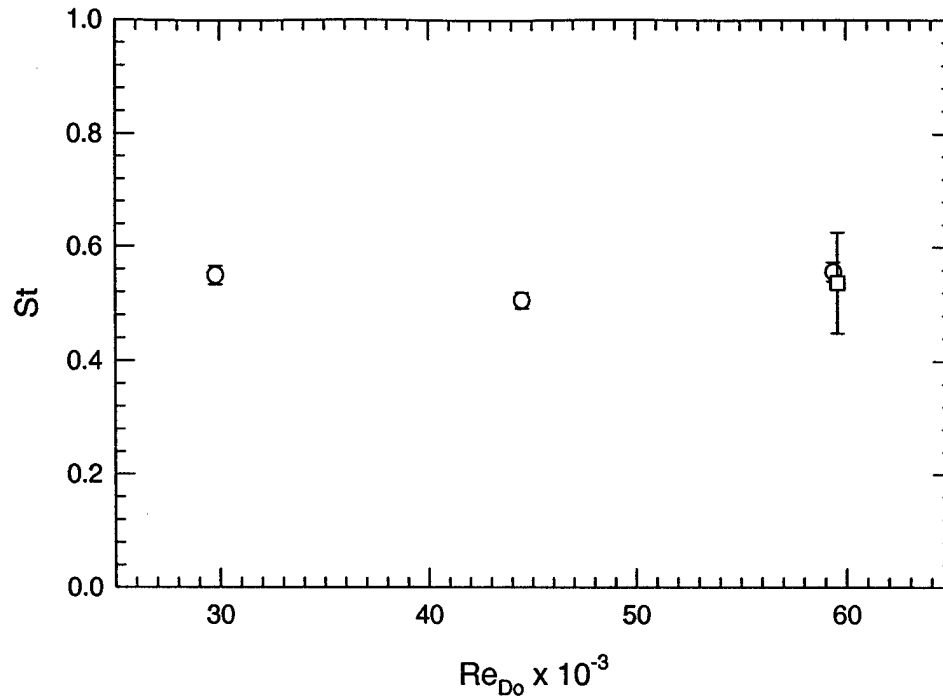
Figure 3.23. Vortex shedding Strouhal number based on the vortex tracking. The round symbols represent the 15 cm canopy and the square symbol represents the 30 cm canopy.
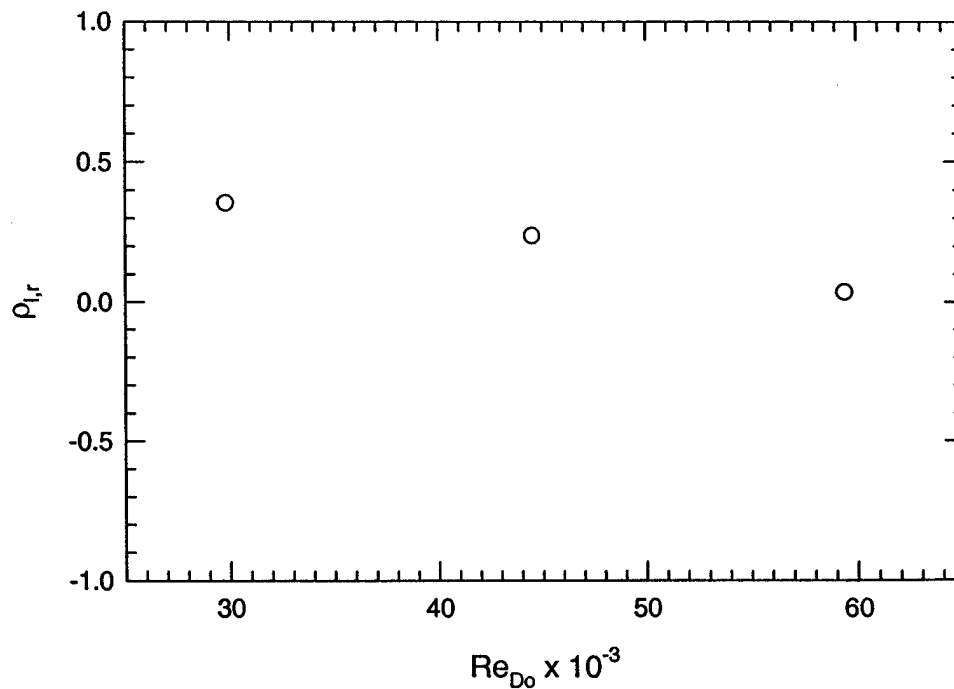

Figure 3.24. The correlation coefficient between the vortex location on the right and left side of the canopy.

66

4. Inflation of a Parachute Canopy

4.1 Canopy Dynamics

The canopy inflation was conducted under the infinite-mass condition where the freestream velocity remained constant during inflation. Images of a representative canopy inflation at Reynolds number of 3.0×10^4 is shown in Fig. 4.1 where $D_o = 15.2$ cm. The canopy diameter and drag are plotted in Fig. 4.2, where the labeled points correspond with the images in Fig. 4.1. Initially the canopy was packed into the deployment tube and the canopy was positioned such that the suspension lines were taut. At time $t = 0.0$ s, the deployment tube was pulled away (Fig. 4.1a) as indicated by the small bump in the force at that time. Once the deployment tube had cleared the canopy, it initially has a cylindrical shape (Fig. 4.1b) which then transitions into a conical geometry (Fig. 4.1c). Over this time period, the canopy diameter has grown to half its fully inflated diameter yet the drag has increased minimally. The fluid then proceeds to fill the canopy from the skirt towards the top of the canopy creating a nearly hemi-spherical canopy (Fig. 4.1d). At this point, the drag has begun to increase towards its maximum value. With the upper regions of the canopy filled, the inflation of the canopy proceeded towards the skirt until the canopy diameter reached its steady state diameter (Fig. 4.1e). The maximum drag occurs after the canopy has become hemi-spherical but before it achieves its maximum diameter. The peak drag occurs over a small time duration in relation to the overall inflation time. The canopy then over-expands beyond its steady state diameter, achieving its maximum diameter in Fig. 4.1f. The drag rapidly declines after achieving its maximum value. The canopy diameter continues to increase towards its peak value while the drag declines. The drag goes through a few oscillation in its amplitude before it

approaches a mean value observed in steady flow. Similarly, after the maximum projected diameter was achieved, the canopy diameter shrinks and the canopy geometry begins to approach the value for steady flow. During the inflation process, the canopy inflated nearly symmetrically and remained centered on the main axis. Only when the canopy had reached the over-expanded state did the canopy require the retention line (see Sec. 2.2) to restrain the off-axis motion.

A characteristic of the small-scale canopy models that differ from larger scale models and full-scale parachutes should be noted. The initial conical shape that the small scale parachute exhibited is different from that of larger parachutes. Larger parachutes typically form a more cylindrical shape during this stage of inflation (see Fig. 1.1). The conical shape is attributed to the material stiffness since at these small scales, the material stiffness (reduced flexibility) becomes more apparent (Heinrich & Hektner, 1971). Also, the maximum diameter of the small-scale models typically occurs at the canopy skirt throughout the entire inflation process. While for full-scale parachutes, the maximum diameter is not necessarily at the canopy skirt. Again, the stiffness of the small-scale models affects the canopy flexibility.

The inflation of canopies at a higher Reynolds number with two different canopy diameters was also carried out. The 15.2 cm canopy was tested at a freestream velocity of 40 cm/s resulting in a Reynolds number of 5.9×10^4, and the 30.5 cm canopy was tested at a freestream velocity of 20 cm/s ($Re_{D_o} = 6.0 \times 10^4$). The tests at the larger Reynolds number showed an inflation process that more closely resembles larger canopy models or full scale canopies. The largest parachute model ($D_o = 30.5$ cm) most closely exhibited this behavior. This inflation sequence is shown in the images of Fig. 4.3 with

the corresponding force and diameter traces in Fig. 4.4. The first two images (Figs. 4.3a-b) shows a canopy in a conical form, typical for small-scale parachutes during early inflation. The shape of the canopy then starts to transition into a more rounded shape (Figs. 4.3c-d). Through these phases, the maximum diameter occurs at the canopy skirt. However, beginning with the fourth image (Fig. 4.3d), the canopy geometry resembles the shape of a full scale parachute where the maximum diameter occurs not at the skirt but closer to the top of the canopy while the skirt remains in a semi-collapsed state; the canopy forms a "mushroom" shape. The canopy then proceeds to fill, achieving its steady state diameter (Figs. 4.3f) and over-expanding to its maximum diameter (Figs. 4.3g). The size of the large canopy allows for greater flexibility of the canopy, and with the higher fluid inertia at the higher Reynolds number, the canopy more closely resembles the inflation of a full-scale parachute.

Three specific times can be defined from the canopy drag and diameter measurements to characterize the canopy inflation. These characteristic times are the opening time, t_o, the filling time, t_f, and the maximum diameter time, t_{max}. In each of these definitions, the initial time (i.e. $t = 0$) is defined to be the time when the deployment tube is first pulled away. Based on this, the *opening time*, t_o, is defined as the time when the peak opening force is attained during the canopy inflation. The *filling time*, t_f, is the first time when the diameter of the canopy first reaches its mean steady state diameter (Knacke, 1992). For an infinite mass inflation, experience has shown that the opening and filling times are approximately equal $(t_o \approx t_f)$ while for a finite mass inflation the opening time is less than the filling time, $t_o < t_f$ (Knacke, 1992). And, t_{max} is defined as the time when the canopy diameter achieves its maximum diameter during the inflation.

69

The maximum diameter time occurs after the filling time, during the over-expansion of the canopy. The opening time will be used as the benchmark for comparison with other defined times; the force measurements were sampled at a higher rate than the other measures. A comparison of these characteristic times is shown in Fig. 4.5. The average values of these characteristic times are listed in Table 4.1, along with *rms*-values (the standard deviation) of the measurements.

Table 4.1. Characteristic times of canopy inflation.

D_o (cm)	Re_{Do}	t_o (s)	t_f (s)	t_{max} (s)	t_o*	t_f*	t_{max}*
15.2	3.0×10^4	1.47 ± 0.12	1.51 ± 0.19	1.78 ± 0.19	1.89	1.94	2.29
15.2	5.9×10^4	0.85 ± 0.17	0.81 ± 0.16	0.93 ± 0.15	2.18	2.07	2.40
30.5	6.0×10^4	2.71 ± 0.11	2.67 ± 0.12	3.22 ± 0.18	1.74	1.72	2.07

The uncertainty in these measures is directly related to the sampling frequency of the force and the image acquisition. The force was sampled at 150 Hz resulting in the uncertainty for each opening time of ±3.3 ms (half the sampling period) while the images were acquired at 30 Hz which results in an uncertainty of ±16.7 ms for the filling and maximum diameter times. Since for each condition the experiments were performed multiple times, a variation in the measurement of the these times occurred. This results in a standard deviation of the times of 0.1-0.2 s, which is considerably higher than the uncertainty in each individual measurement. Therefore, the standard deviation was used to quantify the uncertainty of the characteristic times. The higher values for the standard deviations was a direct result of the inconsistencies in packing and folding of the canopy in the deployment tube.

It has been shown that the filling distance, the product of the freestream velocity and the filling time, should remain constant for a given parachute canopy (Knacke, 1992).

70

This filling distance can be normalized with the constructed diameter to create a non-dimensional filling time,

$$t_f* = \frac{t_f U_\infty}{D_o}.$$

4.1

Similar non-dimensional opening (t_o*) and maximum diameter ($t_{max}*$) times can be defined using the convective time scale of D_o/U_∞. The normalized characteristic times are plotted in Fig. 4.6 and also listed in Table 4.1. The plots show that the characteristic times remain nearly constant at least within the uncertainty of the measurements. The mean normalized filling time (over all Reynolds numbers and geometries) is 1.9 which is on the order of filling times found on full size parachutes and model tests at finite mass conditions. Heinrich & Noreen (1970) report normalized filling times on the order of 3.5 for a 3 ft. scale model with flat circular geometry. Lee (1989) states for finite mass ¼-scale flat circular canopies, the normalized filling times have a range of 2.25 – 3, and for full scale canopies the filling times are approximately 4. Additionally, Knacke (1992) reports normalized filling times of 2.9 for low porosity canopies. The lower normalized filling time achieved in this study is due to the higher stiffness of the canopy (Johari & Desabrais, 2001).

An average opening force trace was created by shifting each individual force measurement trial (at a given Reynolds number and scale) in time such that the peak opening forces were aligned and then an ensemble average of the force traces was performed. The resulting average force was normalized as a force coefficient, C_F, using Eq. 3.3 and the time was normalized using the opening time as,

71

$$\tau = \frac{t}{t_o}. \qquad\qquad 4.2$$

The normalized opening force is plotted in Fig. 4.7 for the three cases studied. All the inflations show similar trends in that during inflation the force remains quite small initially. At $\tau \sim 0.6$-0.7, the drag begins to rise until at $\tau \approx 0.9$ it exhibits a rapid increase to its maximum value at $\tau = 1.0$ (by definition) after which the force decreases sharply where it begins to transition to that seen in steady flow. The largest forces are confined to a short time duration centered around the peak value. Furthermore, the mechanisms causing this localized peak force are also confined to a small interval in time. This suggests that the canopy dynamics and the transient flow features are key to understanding the inflation process as a whole.

The peak opening force coefficient is listed in Table 4.2. The values obtained in this study compare well to values obtained in inflation experiments conducted with similar scaled canopies (also listed in Table 4.2).

Table 4.2. Peak force and canopy diameter values.

D_o (cm)	Re_{D_o}	$(C_F)_{max}$	$(D_m/D_o)_{max}$	fluid medium	reference
15.2	3.0×10^4	3.5	0.89	water	-
15.2	5.9×10^4	2.9	0.86	water	-
30.5	6.0×10^4	3.6	0.86	water	-
40	7.2×10^4	3.4	0.80	water	Lingard, 1978
80	4.8×10^5	2.0	0.75	air	Lingard, 1978

The canopy diameter measurements can also be ensemble averaged in a similar fashion as the force measurements. For comparison with the averaged force measurements, the diameter measurements were shifted in time such that the alignment

72

point was again the time when the peak opening force occurred. The diameter measurements were sampled at a rate considerably less than the force measurements (*i.e.* 30 Hz as opposed to 150 Hz). Therefore, its was necessary to identify the image frame where the peak force occurred in each run. These points were then used as the alignment points and an ensemble average was calculated for the three cases studied. The results of these calculations are shown in Fig. 4.8, where the diameter has been normalized with the constructed diameter, D_o, and the time has been normalized with the opening time. Heinrich (1969) and Heinrich & Noreen (1968) have experimentally shown that the normalized canopy diameter varies linearly with the normalized time initially, and then transitions to a quadratic. Their experiments were performed with a 91 cm parachute model tested in a wind tunnel, under both infinite and finite-mass conditions. In that experiment, the diameter varied with the square root of the normalized time squared for a normalized time greater than one. Heinrich (1969) noted that the results obtained for the finite mass case could be applied to the infinite mass case at least over the range $0 \leq \tau \leq 1.0$ excluding the amplitude of the peak maximum projected diameter. Since all the canopies examined in this study are geometrically similar and the averaged diameter data seems to collapses on to a single curve (see Fig. 4.8), a function of the form suggested by Heinrich and Noreen (1968) was fitted to the averaged canopy data. The results of the least-squares curve fitting is shown in Fig. 4.8 and Eq. 4.3.

$$\frac{D_m}{D_o} = \begin{cases} 0.032 + 0.626\tau & \text{for } 0.2 < \tau < 0.8 \\ 1.96 - 4.21\tau + 3.04\tau^2 & \text{for } 0.8 \leq \tau \leq 1.0 \\ 0.541 + \sqrt{0.100 - (\tau - 1.197)^2} & \text{for } 1.0 < \tau \leq 1.3 \end{cases} \qquad 4.3$$

The Heinrich & Noreen (1968) relation is also plotted in Fig. 4.8. The numerical coefficients in Eq. 4.3 are different than those given by Heinrich & Noreen; however, the functional form of the relations are validated by the quality of the curve fit to the data. Berndt & DeWeese (1966) imaged the inflation of full-scale canopies and derived an empirical relationship for the canopy diameter. This relationship is also plotted in Fig. 4.8. It is evident that there are deviations between full-scale and small-scale models. Heinrich & Noreen (1968) also observed this and stated,

> "It is possible that the relatively higher stiffness of the parachute model
> causes this deviation during the early phase and it would probably be
> necessary to investigate this region in more detail when an attempt is made
> to utilize the results of the model experiments for calculation of filling
> processes of large parachutes."

It should be noted that in the Berndt & DeWeese (1966) and the Heinrich & Noreen (1968) studies, the time was normalized with the filling time instead of the opening time. Since the opening time is approximately equal to the filling time for an infinite mass inflation, this would at most cause a change in the coefficients.

The results obtained in the current study achieved a higher normalized diameter than that obtained by Heinrich & Noreen (1968). This behavior is exhibited by larger slopes of the curves and the higher peak projected diameters achieved. The peak maximum normalized projected diameters, $(D_m/D_o)_{max}$, achieved are shown in Table 4.2. Heinrich (1969) reports a maximum projected diameter ratio of $(D_m/D_o)_{max} \approx 0.7$ for an infinite mass inflation of a 91 cm model in a wind tunnel at $Re \sim 10^6$ and Lingard (1978) reports values of $(D_m/D_o)_{max} \approx 0.75\text{-}0.80$ for a constant velocity inflation in air and water

(see Table 4.2). It is expected that the higher stiffness of the small canopy models resulted in the higher values of the maximum projected diameters.

The volume, V, enclosed by the canopy was estimated from the images of the canopy inflation assuming that the canopy was axisymmetric during the inflation. The details of the volume estimation method are given in Section 2.3. A sample of the transient enclosed volume for the 15 cm canopy at $Re_{Do} = 3.0 \times 10^4$ is shown in Fig. 4.9. An average enclosed volume was calculated by alignment of the peak force, using the same method explained in the averaging of the canopy diameter. The average enclosed canopy volume is shown in Fig. 4.10, where the enclosed volume was normalized by the mean enclosed volume, V_{steady}, when the canopy is under steady flow conditions. All the inflations show a continual increase in the volume enclosed by the canopy until just after the time that the peak opening force occurs ($\tau = 1.0$). The canopy then over-expands and rapidly approaches the steady state volume. From the enclosed canopy volume, estimates of the unsteady potential flow are possible using the expressions employed in Section 3.2. Details of these calculations are presented in Section 4.4.

4.2 Flow Field Evolution

The canopy geometry and the forces that the canopy experiences during inflation are directly related to the evolution of the flow field surrounding the canopy. The velocity field in a plane was measured in the near wake of the canopy and the azimuthal vorticity field in that plane was calculated. From observations of these fields during the inflation process, it was possible to characterize the inflation process into three distinct stages, with each stage specified by the state of the boundary layer on the canopy. The

stages are as follows: I. the initial canopy inflation where the boundary layer stays completely attached to the canopy; II. the point at which boundary layer separates from the canopy surface near the apex and the separation point moves upstream along the canopy surface; and III. the point where the boundary layer separates completely from the canopy at its skirt.

A sample of the development of the vorticity field around the 15 cm canopy at a Reynolds number of 3.0×10^4 is shown in Fig. 4.11. The thick green line in each of the plots is an approximation of the canopy outline in the measurement plane. The measured force and diameter for this specific inflation is plotted in Fig. 4.12 with the labeled points corresponding to the images in Fig. 4.11.

Initially the canopy was packed into the deployment tube and the canopy was positioned such that the suspension lines were taut. At time $t = 0$ s, the deployment tube is pulled away. Once the deployment tube clears the canopy, the canopy begins inflating immediately into a conical, umbrella shape, (Figs. 4.11a-b) with the projected frontal area increasing. During this initial inflation stage, the force has remained essentially constant (Fig. 4.12). The vorticity fields show that the boundary layer along the canopy surface is fully attached to the canopy with the possible exception of the area very near the canopy apex where minor vortex shedding is observed. At this point in time (Fig. 4.12 c-d), the force starts to increase. Over this same interval (c-d), the canopy diameter has grown by approximately 50%, yet the general characteristics of the vorticity field have remained unchanged. The boundary layer was still attached to the canopy surface (Figs. 4.11c-d). This sequence represents stage I of the inflation process.

The essence of the flow field begins to change into another stage from this point forward. The canopy geometry has begun to transform from a conical to a more hemispherical shape (Figs. 4.11d-e). The boundary layer starts to separate from the surface of the canopy near the apex (Figs. 4.11e-f). This initiates the beginning of stage II of the inflation process. The separated region of the boundary layer becomes highly disorganized while the rest of the boundary layer remains attached to the canopy surface farther upstream (the region closer to the canopy skirt). The point where the vorticity contours separate from the canopy surface (Figs. 4.11f-i) begins to travel upstream towards the canopy skirt while the canopy diameter progresses through its steady state shape, the filling time (Figs. 4.11g-h), and then to an over-expanded state. With the upstream movement of the separation point, the force passes through its maximum value (Fig. 4.12, point h) and then decreases sharply. Following the time when the maximum force occurs, the boundary layer separates completely from the canopy lip (Fig. 4.11i) and rolls-up into a vortex ring near the skirt. This initiates stage III of the inflation process. The separated flow can be confirmed by the existence of opposite signed vorticity between the canopy surface and the separated boundary layer (Figs. 4.11 i-j). The vortex ring formed by the roll-up of the vorticityhas been named the unloading vortex since it occurs during the rapid reduction of the force or the "unloading" of the canopy. Subsequent to the separation of the boundary layer from the canopy skirt, the maximum diameter was achieved (Figs. 4.11j).

The separated boundary layer becomes similar to a conventional shear layer attached at the canopy skirt. The shear layer remains separated at the canopy edge; the formation of the vortex is completed in Figs. 4.11k-n. This vortex ring eventually

separates from the feeding shear layer and is conveyed downstream, initiating the process of wake formation behind the canopy. The canopy diameter and force also begin to change to the characteristics of a canopy in steady flow (Figs. 4.12k-n).

Similar flow field characteristics were observed at the other two conditions examined in the study. An inflation of a 30 cm canopy at $Re_{Do} = 6.0 \times 10^4$ is shown in Fig. 4.13, with the corresponding force and diameter measurements in Fig. 4.14. The same trends can be identified in the inflation where the force only rises minimally during stage I of the inflation where the boundary layer remains attached to the canopy surface (Figs. 4.13a-d). Then, the boundary layer separates (the beginning of stage II) from the surface (Fig. 4.13d) near the apex region while the remainder of the boundary layer stays attached to the canopy. The separated portion of the boundary layer became highly disorganized and the separation point travels towards the canopy skirt (Figs. 4.13d-k) during which time the peak opening force occurred (Fig. 4.13i-j). The separation point reached the canopy skirt (stage III, Fig. 4.13k) and the unloading vortex began to form. The maximum diameter was achieved (Fig. 4.13l) shortly after the time the peak opening force occurs. The unloading vortex was fed vorticity from the separated boundary layer until it separates from the canopy and was conveyed downstream (Figs 4.13l-n).

The general characteristics of each stage of the inflation process can be summarized as follows. During stage I of the inflation, the boundary layer remains attached to the canopy surface as the volume enclosed by the canopy increases as a result of the increase in the diameter of the canopy. The shape of the canopy during this stage of inflation is conical, at least on the small-scale model canopies studied. The boundary layer sheds only small weak vortices near the apex, forming a narrow wake region

78

confined to an area directly behind the canopy. However, over the majority of the canopy surface, the boundary layer remains attached. A rigid, static bluff body with a similar shape in a constant freestream would not be able to sustain an attached boundary layer. The flow would separate from the rigid body at the lip. The motion of the canopy surface, due to its flexible nature, allows the boundary layer to remain attached to the canopy. While the boundary layer remains attached to the canopy, the drag rises minutely even as the canopy diameter substantially grows at a steady rate.

The stage II initiates with the local separation of the boundary layer from the apex region of the canopy surface. The separated ends of the boundary layer become disorganized and cause the wake of the canopy to grow. The separation location along the canopy surface moves from the apex region towards the canopy skirt. This causes the wake region to become comparable with the canopy diameter. During this stage, the force rapidly rises to its peak value with an almost equally sever decline in the force afterward. The shape of the canopy also transforms from conical to hemi-spherical. The canopy diameter continues to grow during this stage.

The final inflation stage begins with the separation of the boundary layer from the canopy skirt. A large unloading vortex ring is formed at the outer edges of the canopy from the fully separated boundary layer. The canopy diameter is drawn out to its maximum value during the ring formation process. The vortex formation creates a low pressure region at the canopy edge, causing the canopy diameter to increase to its maximum diameter. The separated boundary layer should be more properly called a shear layer at this point since it is now similar to the shear layers seen in typical bluff body flows. The complete shedding of the unloading vortex ring initiates the

79

development of the wake associated with the fully inflated canopies in steady flow. The shear layer continually sheds vortices in a periodic manner from this point forward. The canopy begins the cyclic breathing phenomena described in Chapter 3.

The beginning of each inflation stage can be defined with a time, for example stage II inflation starts at $t \equiv t_2$ and similarly stage III begins at $t \equiv t_3$. These times are listed in Table 4.3 for the condition studied.

Table 4.3. Boundary layer separation times.

D_o (cm)	Re_{Do}	t_2 (s)	t_3 (s)	τ_2	τ_3
15.2	3.0×10^4	1.08 ± 0.19	1.52 ± 0.21	0.79	1.10
15.2	5.9×10^4	0.59 ± 0.11	0.88 ± 0.17	0.71	1.05
30.5	6.0×10^4	2.33 ± 0.43	3.63 ± 0.54	0.66	1.02

The uncertainty in these times is ± 0.033 s for 15 cm canopy and ± 0.067 s for the 30 cm canopy which is half the sampling period of the velocity field measurements for the 15 cm canopy and a full period for the 30 cm canopy. However, these values are significantly less than the standard deviations of the measurements so the standard deviations were used as an estimate for the uncertainty in the separation times. The selection of the separation times is based on the vorticity contours since in the strictest sense the point of separation is defined as the point where the wall shear stress becomes zero. However due to the spatial as well as the temporal resolution of the velocity field measurements made in these experiments, it was not possible to apply this criteria for selecting the point in time when the boundary layer separated from the canopy surface.

Normalizing the separation times with the opening time shows the relationship between the peak opening force and the flow field behavior. The normalized separation

times, $\tau_2 \equiv t_2/t_o$ and $\tau_3 \equiv t_3/t_o$, are plotted in Fig. 4.15 and listed in Table 4.3. A weak Reynolds number dependence is apparent from the data but it is quite clear that the onset of the boundary layer separation happens prior to the opening shock. The formation of the unloading vortex begins after the boundary layer has completely separated from the canopy skirt in stage III. Therefore, since the ring formation begins after the opening shock has already occurred, the unloading vortex is not the cause of the opening shock. The opening shock takes place during stage II. It is clear that the boundary layer separation process is responsible for the opening shock.

The diameter of the canopy, D_{t2} and D_{t3}, at the onset of the two stages is listed in Table 4.4. The mean steady state diameter, D_p, was used to normalize these diameters. The uncertainty values listed is based on the standard deviation of the measurements which was higher than any uncertainty in the measurement of the canopy diameter or the data rate. The boundary layer first separates once the canopy reaches approximately two-thirds of its mean steady state diameter. It should be reminded that this separation point is not at the canopy skirt but near the canopy apex. For a rigid bluff body with a shape similar to the canopy at time t_2, the flow would separate at the lip. The boundary layer only separates from the canopy skirt when the canopy diameter has over-expanded to ~10% of its steady state value. This shows that the dynamic nature of the flexible canopy is a key characteristic of the overall flow field behavior.

Table 4.4. Boundary layer separation diameters.

D_o (cm)	Re_{Do}	D_{t2} (cm)	D_{t3} (cm)	D_{t2} / D_p	D_{t3} / D_p
15.2	3.0×10^4	8.3 ± 1.9	13.1 ± 0.5	0.71	1.14
15.2	5.9×10^4	7.3 ± 0.9	12.6 ± 0.7	0.65	1.12
30.5	6.0×10^4	15.8 ± 2.7	25.1 ± 1.1	0.68	1.08

4.3 Integral Measures of the Wake

The circulation, Γ, of the boundary/shear layer was calculated from the velocity field using the definition of the circulation, namely,

$$\Gamma \equiv \oint_s \vec{u} \cdot d\vec{s} \qquad\qquad 4.4$$

where $\vec{u}$ is the velocity along the path s. The integration path selected was along an iso-vorticity contour. The iso-vorticity contours used in the calculation is listed in Table 4.5.

Table 4.5. Vorticity level of integration path.

D_o (cm)	U_∞ (cm/s)	Re_{Do}	$\vec{\omega}$ contour-level (s^{-1})
15.2	20	3.0×10^4	5.0
15.2	40	5.9×10^4	15.0
30.5	20	6.0×10^4	5.0

An example of the development of the circulation for the 15 cm canopy at $Re_{Do} = 3.0 \times 10^4$ is shown in Fig. 4.16. An ensemble average of the circulation was calculated by time shifting the individual temporal circulation plots such that the time the peak force occurred were aligned (the same method described in Section 4.1). The average temporal evolution of the circulation for each condition tested is plotted in Fig. 4.17. The solid line is a 5-point moving window average of the data and the vertical dotted lines represent the separation and opening times as labeled.

Initially, the circulation is at a nearly constant level up until the time of boundary layer separation at $t = t_2$. The circulation then begins to increase in value as the boundary layer separation point moves along the canopy surface, increasing the amount of vorticity in the flow field. The separated boundary layer produces large amounts of vorticity. Once the boundary layer completely separates from the canopy at the skirt ($t = t_3$), the circulation begins to level out. This is the point where the unloading vortex is taking

shape. The amount of vorticity contained in the unloading vortex will continue to increase as long as it remains attached to the shear layer. However, once it separates from the shear layer, the vorticity contained will remain constant. Decay of circulation is expected as time evolves. The method used to calculate the circulation only examines a single signed vorticity above the values listed in Table 4.5 so the plots in Fig. 4.17 will level out to a constant value after $t \sim t_3$. Only the unloading vortex was tracked for its circulation and not the shear layer that occurs after the unloading vortex is shed from the canopy. So even though additional vorticity is being introduced into the flow field from the shear layer, the circulation values plotted in Fig. 4.17 only reflects the circulation of the unloading vortex.

Normalizing the circulation with the freestream velocity and constructed diameter ($\Gamma/(U_\infty D_o)$) shows that, during stage II of inflation ($t_2 \leq t \leq t_3$), the evolution of the circulation in the separating boundary layer remains the same for the three cases studied. The normalized circulation is plotted in Fig. 4.18. The normalized circulation of the unloading vortex levels out to a value of approximately unity after the canopy inflation is complete (i.e. $t \geq t_3$). The time it takes for the vortex circulation to approach this value is $t \cdot U_\infty/D_p \approx 3\text{-}4$. This normalized vortex formation time is on the same order as that seen for the formation of impulsively started vortex ring. Gharib et al. (1998) showed that the vortex ring formation time of an impulsively started jet was in the range 3.6-4.5.

In Section 1.4, it was shown that the rate of change of the fluid impulse provides an estimate of the fluid force on the canopy due to the wake vorticity. During the inflation of the canopy, the vorticity is primarily confined to the boundary layer on the canopy surface and the unloading vortex that results from the separation of the flow. The

83

impulse for each inflation was calculated using Eq. 1.8 where the integration volume was assumed axisymmetric, and only a rectangular region which enclosed the vorticity from the centerline of the canopy radially outward and axially from the canopy skirt in a downstream direction was utilized (see Section 2.5 for a more complete description). In order to minimize the noise introduced to the impulse calculations from the background vorticity, any vorticity values less than those listed in Table 4.5 were set to zero during the calculation. An example of the result of the impulse calculation is shown in Fig. 4.19.

An ensemble average of the impulse was performed at each test condition, using the method of time shifting described earlier. The results of this analysis is shown in Fig. 4.20 where the solid line is a 5-point moving window average of the data and the vertical dotted lines represent the separation and opening times as labeled. The averaged data show that initially the flow impulse has a minimum value with only a small increase during the stage I. Once the flow begins to separate at the onset of stage II, the impulse starts to rapidly increase. After the flow has completely separated at $t = t_3$, the impulse appears to increase linearly with time. The impulse was normalized as follows:

$$\frac{I_z}{q_o S_o t_o}.$$
4.5

The normalized average impulse is shown in Fig. 4.21. This normalization shows that the impulse increase is similar for the three cases studied. From the impulse calculation, estimates of the vortical force are made.

4.4 Composition of Fluid Dynamic Forces

A relationship for calculating the force that the canopy experiences based only on measurements of the flow field was derived in Section 1.4. The force the canopy

84

experiences from the flow field is attributable to two primary sources; the unsteady potential flow associated with the change in the volume of the canopy (the apparent mass) and that associated with the production of vorticity in the wake (the rate of impulse production).

The unsteady potential flow around the canopy produces a force which is related to the enclosed volume of the canopy. It was shown in Eq. 1.11 that the potential force is proportional to the time rate of change of the enclosed volume,

$$F_p = k_p \rho U_\infty \dot{V}.$$

4.6

This is true as long as the canopy is not decelerating. For the cases examined in this study, the freestream velocity was maintained at a constant value. The enclosed volume of the canopy was estimated from the images of the canopy as described in Section 4.1. From these measurements, the derivative of the volume was estimated using a central differencing scheme and assuming the proportionality constant k_p to be unity. The potential flow force increase is shown in Fig. 4.22. The potential force grows in a nearly linear fashion from an initially zero value until just prior to the opening time when the potential force reaches its maximum value. After achieving its peak value, the potential force drops precipitously to values that oscillate around a zero mean value. The peak value of the potential force is small in relation to the total peak force during the inflation. Typically, the peak potential force achieved during the inflation was 7-9% of the peak opening force under the assumption that $kp = 1$.

The potential force was normalized to a potential force coefficient as

$$C_{F_p} = \frac{F_p}{q_o S_o}$$

4.7

which is plotted in Fig. 4.23. The data collapse to a single curve except for some scatter around $\tau \sim 0.7$. The solid line in Fig. 4.23 is the average of all three conditions. The peak value occurs at $\tau \sim 0.95$, just before the opening shock at $\tau = 1$.

The forces associated with the vorticity containing regions of the flow are calculated from the time derivative of the flow impulse. The relation for this calculation was given in Eq. 1.9 as

$$F_\omega = \frac{dI_z}{dt} = -\pi\rho\frac{d}{dt}\iint r^2\omega_\theta\,drdz. \qquad 4.8$$

The axial impulse was calculated for each test and then an ensemble average of the data was generated with the results presented in Section 4.2. The impulse was smoothed using a 5-point moving window average then the time derivative of the smoothed data was taken by a central differencing scheme. The results of the differentiation for each test condition is shown in Fig. 4.24. These plots show that prior to the flow separation at $t = t_2$, the vortical force rises slowly from a near zero value. Upon approaching the onset of stage II, the vortical force rapidly rises before reaching a maximum value at or near the opening time ($t = t_o$). Afterward, the vortical force declines from the maximum to a lower value. The peak vortical force was 50-60% of the total peak opening force. This clearly demonstrates that a large portion of the total opening force is directly attributable to the increase of impulse with time. As was discussed in section 1.4, the vortical force can be increased by moving the vorticity radially outward with time. Therefore, the force the canopy experiences is caused by the rapid movement of vorticity away from the centerline of the canopy while the separation point of the boundary layer moves upstream along the canopy surface. The amount of vorticity in the boundary layer does continue to

increase as seen in the increase of the circulation during the inflation. However, the bulk motion of the vorticity away from the canopy centerline is expected to be the primary factor in the increase of the force. Once the boundary is separated from the canopy at the skirt, the vorticity no longer moves rapidly outward from the canopy centerline, so the force decreases as the bulk of the vorticity stabilize at a particular location. The circulation still can increase and its general location might also move but only in a relatively minute way when compared to the bulk motion during the inflation process.

It is expected that the estimated vortical force inadequately predicts the actual value since the PIV measurements were done at a grid resolution which would under-resolve the boundary layer vorticity. The boundary layer of the canopy is confined to a very small region along the canopy surface, and in order to properly resolve the boundary layer, it would require the measurements to focus in on a limited portion of the canopy surface. This would preclude measuring the near wake region of the canopy and estimating the fluid impulse. However, it is felt that the measurements of the canopy wake performed are a reasonable estimate for the overall behavior of the inflating canopy. If the boundary layer vorticity is under-resolved, this would tend to under-predict the fluid impulse and the vortical force.

The vortical force was normalized as follows:

$$C_{F_\omega} = \frac{F_\omega}{q_o S_o} .$$

4.9

This is plotted in Fig. 4.25. The solid line in the figure represents the average of the three cases studied. It is clear that for each case, the inflation process follows a similar trend. However, there does seem to be some scatter among the three cases for $\tau \geq 1.0$.

87

The potential force and the vortical force were combined to obtain an estimate of the total aerodynamic force the canopy experiences during the inflation. The combined force estimate is plotted in Figs. 4.26- 4.28. Also plotted in the figures are the individual potential and vortical forces along with the measured total force. The combined force estimate exhibits a similar trend to that seen in the measured force. In each case, the combined force estimate predicts approximately 50-60% of the peak opening force. The combined force calculation over-estimates the opening force prior to the opening shock for the 15-cm canopy. The combined force estimates made with the smaller canopy tend to over-estimate the breadth of the opening shock as well. While the estimates for the larger canopy match the measured force well in terms of the breadth of the estimate of the opening shock. The prediction deficiencies are attributable to any possible three-dimensional effects, vorticity resolution issues, as well as neglecting the other terms in Eq. 1.5 of section 1.4.

The potential force only plays an important role during the early stages of inflation (up to $\tau \sim 0.5$) when the boundary layer remains attached to the canopy surface. Therefore, it is shown that the peak opening force during canopy inflation is primarily caused by the viscous wake effects. Traditional methods of modeling the opening force using a combination of an added mass term (*i.e.* the unsteady potential flow force) and a constant drag coefficient term, to account for the wake effects, are inadequate. The added mass effects account for less than 10% of the peak opening force. Afterwards, the primary force on the canopy comes from the wake formation. The behavior of the boundary layer during the inflation is the driving factor in the wake formation.

4.5 Decelerating Freestream

In order to simulate the inflation of a finite mass parachute system, the freestream velocity has to decelerate. To achieve a decelerating freestream, the tunnel speed controller was turned down. A linear decrease of the water tunnel velocity was achieved in a repeatable manner for the range of 18 – 8 cm/s over a 5 s time span. Figure 4.29 shows the freestream velocity decreasing linearly with time. The best-fit line to the data has a slope of 1.92 cm²/s, resulting in a normalized deceleration rate of

$$\dot{U}_{\infty} D_o / U_s^2 \cong 0.1.$$

Here, U_s is the freestream velocity at the time the canopy is extracted from the tube. In the experiments, U_s was approximately 17 cm/s. The normalized deceleration rate is comparable with that calculated with the mean deceleration rate of a full-scale parachute system. However, there is a difference between our constant deceleration experiments and those of finite mass parachutes. A full-scale parachute system with a fixed, finite mass would slow down over a range of deceleration rates due to the variations in the aerodynamic drag of the canopy. In the present experiments, the deceleration rate was held constant. Although the deceleration rate in the present experiments does not mimic that in finite mass inflations, it does allow for the examination of the fundamental effects of a varying freestream on the wake formation during the inflation period.

The 15-cm canopy model was tested with the constant deceleration freestream. The average opening time was 1.9 s (± 10%), which is approximately 30% longer than that for the constant freestream velocity. The increased opening time is not only due to the continuous deceleration, but also a lower initial velocity (17 vs. 20 cm/s). The opening force and the canopy diameter for a sample run are plotted in Fig. 4.30. The

entire inflation time took less than 3 s, including the over-expansion. Similar to a constant freestream inflation, drag rises very modestly during the initial second while the canopy diameter expands to about one-half of its steady state diameter. Then, the force increases rapidly to its peak while the canopy continues its expansion. Following the peak force, drag decreases immediately and then a second peak in force is observed. At the same time, the canopy over-expands to its maximum diameter. As time progresses, the canopy settles down to its steady breathing state. Throughout the inflation, the freestream velocity is decelerating at a constant rate. The canopy dynamics are quite similar to those for the constant freestream case, compare Fig. 4.30 with Fig. 4.2.

The velocity field in the near wake of the canopy was measured in a similar way as in the constant freestream cases described earlier. Fig. 4.31 shows the vorticity contours of the inflating canopy under constant deceleration for the run in Fig. 4.30. The time separation between the successive images is 0.33 s. Examination of these images reveals a trend nearly identical to that observed with the infinite mass cases discussed earlier (see Fig. 4.11). Initially, the boundary layer is attached to the canopy surface (Fig. 4.31 a). Subsequently, the separation begins from the apex region and travels upstream towards the canopy skirt. The peak opening force occurs during this period, and it is at the time corresponding to Fig. 4.31 c. The separated boundary layer subsequently rolls-up into a vortex ring Fig. 4.31 f-g. The unloading vortex, which draws out the canopy to its maximum diameter, convects downstream to form the open wake associated with the fully inflated bluff canopy.

From the vorticity field, the wake impulse was calculated for each instantaneous data field. The method developed for ensemble-averaging the constant freestream data

was used to compute an ensemble-averaged impulse time trace (see Fig. 4.32). The time has been normalized by the average opening time; $\tau = t / t_o$. The impulse rises slowly until $\tau \approx 0.8$, after which a rapid change in the impulse is observed. Again, the impulse time trace for the constant deceleration is qualitatively similar to the constant freestream case, compare Fig. 4.32 with Fig. 4.17a.

To examine whether the time rate of change of impulse, dI / dt, contributes to the total force experienced by the canopy, the measured force is compared with dI / dt in Fig. 4.33. Both parameters have been normalized with the freestream dynamic pressure and the constructed canopy area. The extraction velocity U_s of 17 cm/s has been used. The ensemble averaged impulse data in Fig. 4.32 was curve-fitted with a sigmoid and then differentiated. The peak opening force occurs slightly before the peak in the dI / dt curve. Moreover, the peak due to dI / dt is $\approx 40\%$ of the peak opening force. The dI / dt curve is broader than the narrow measured force spike, similar to the constant freestream peak force comparisons in Fig. 4.26. It is worthwhile to note that the peak in the dI / dt curve contributes to a smaller portion of the peak opening force ($\approx 40\%$) in the decelerating case than the constant freestream case (over 50%). The decelerating freestream experiments appears to indicate that the finite mass and infinite mass inflations have similar viscous wake development sequences and the conclusions drawn for the infinite mass case would be applicable to the finite mass case. However, the exact magnitude of parameters may be different between the two inflation scenarios.

91
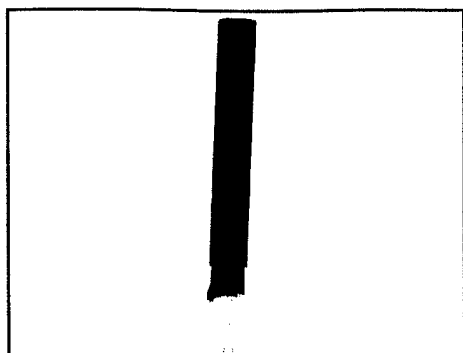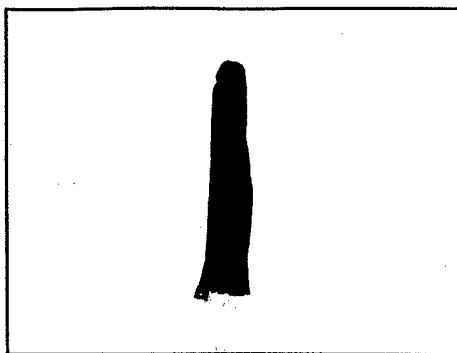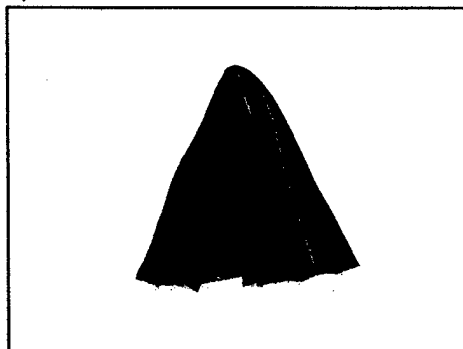
a) $t = 0.00$ s b) $t = 0.23$ s c) $t = 1.00$ s d) $t = 1.23$ s e) $t = 1.43$ s f) $t = 1.70$ s g) $t = 2.00$ s h) $t = 2.27$ s
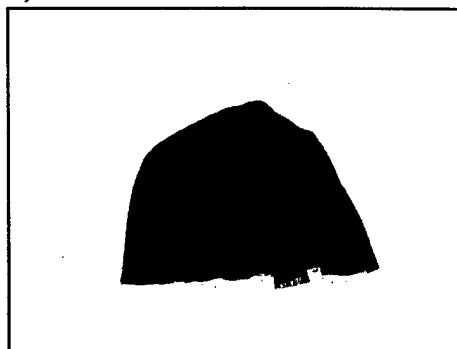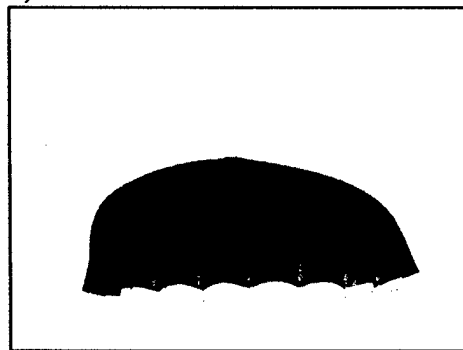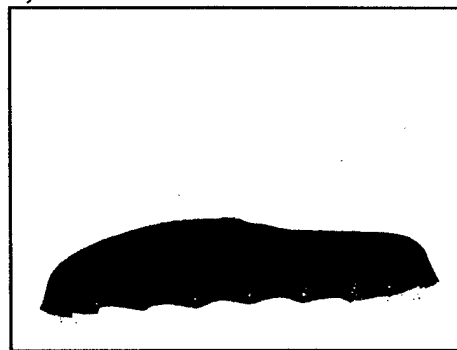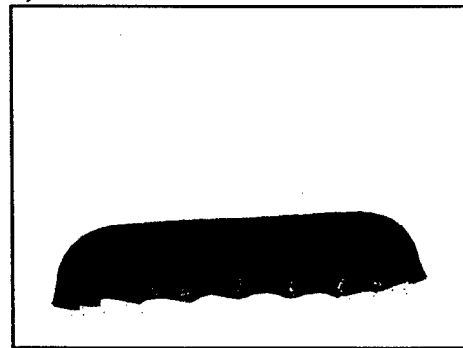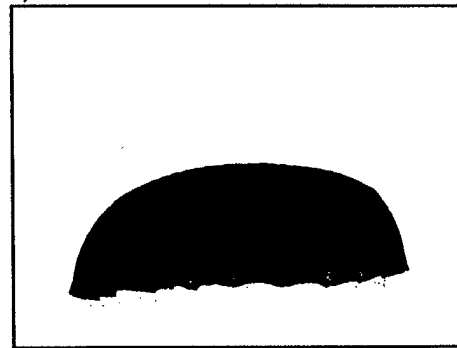
Figure 4.1. Images of a canopy inflation for a 15 cm canopy at a freestream velocity of 20 cm/s. Images correspond with labeled points in Fig. 4.2.
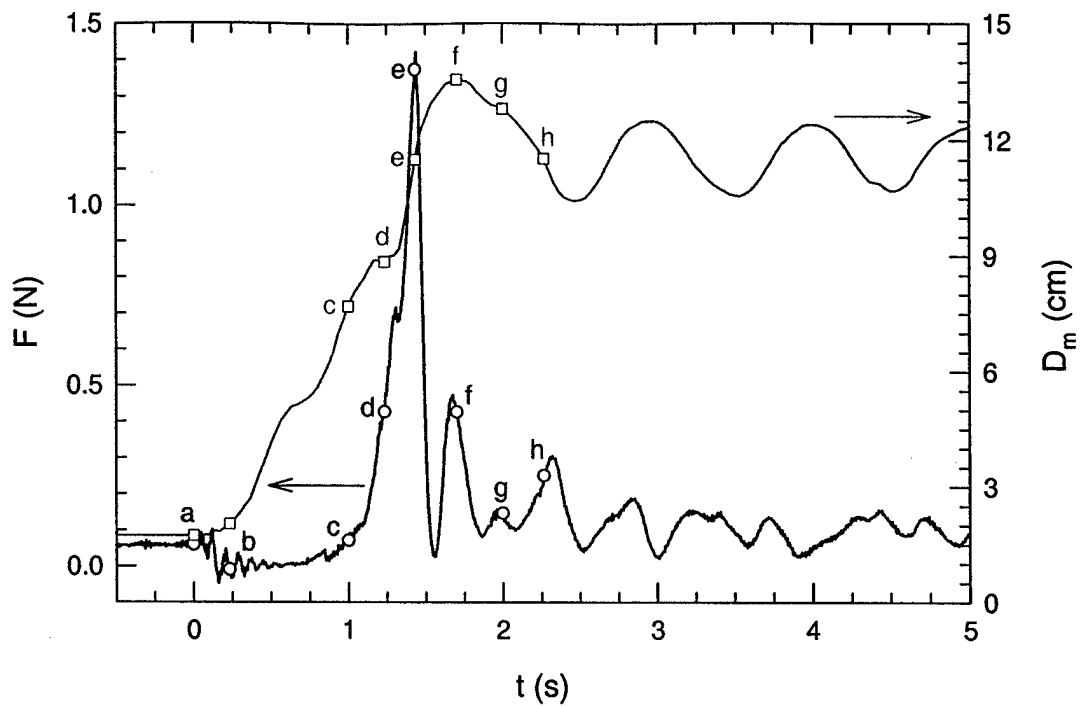
Figure 4.2. The opening force and diameter for a 15 cm canopy at a freestream velocity of 20 cm/s. Labeled points correspond with the images in Fig. 4.1.

93
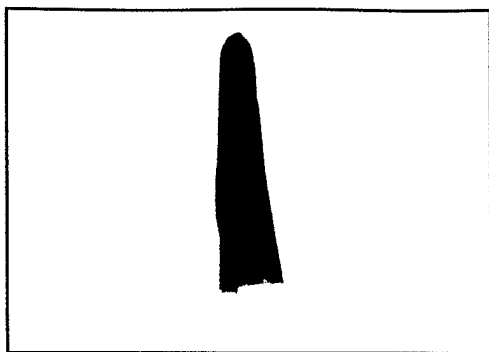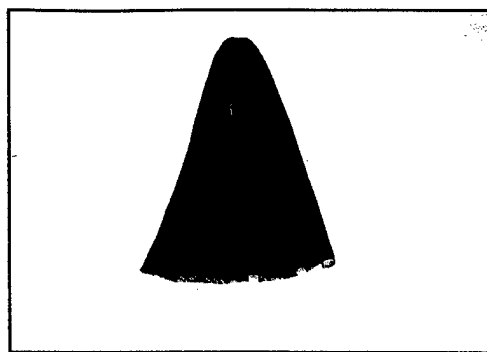
a) $t = 0.50$ s   b) $t = 1.50$ s
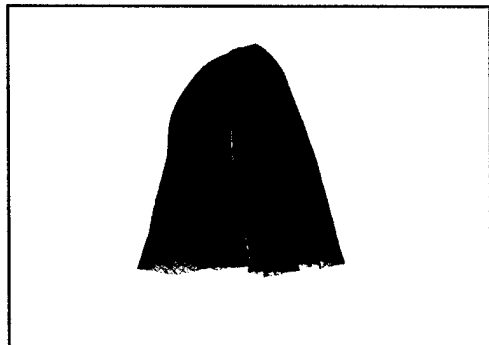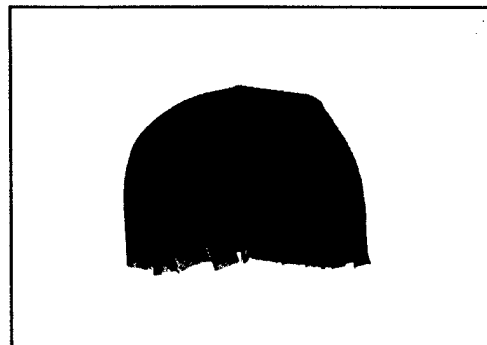
c) $t = 1.70$ s   d) $t = 2.10$ s
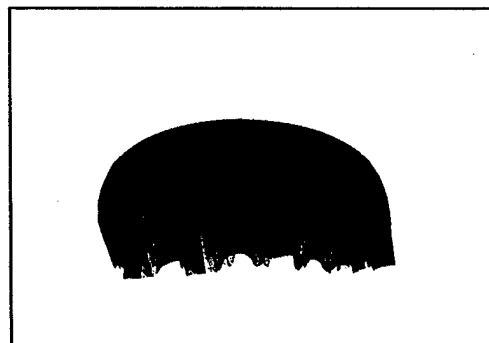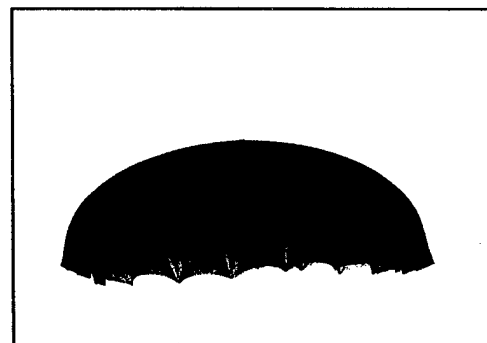
e) $t = 2.40$ s   f) $t = 2.63$ s
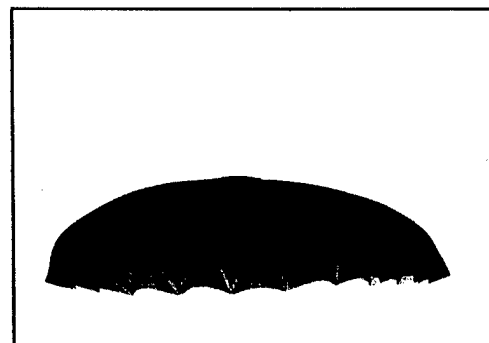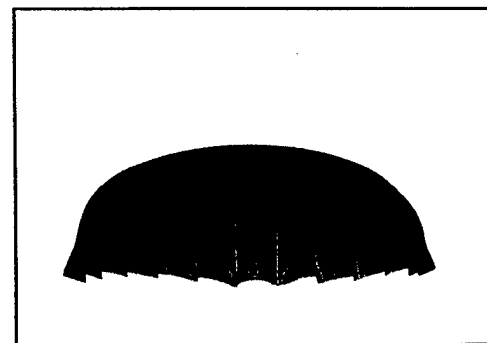
g) $t = 3.10$ s   h) $t = 4.10$ s

Figure 4.3. Images of a canopy inflation for a 30 cm canopy at a freestream velocity of 20 cm/s. Images correspond with labeled points in Fig. 4.4.

94
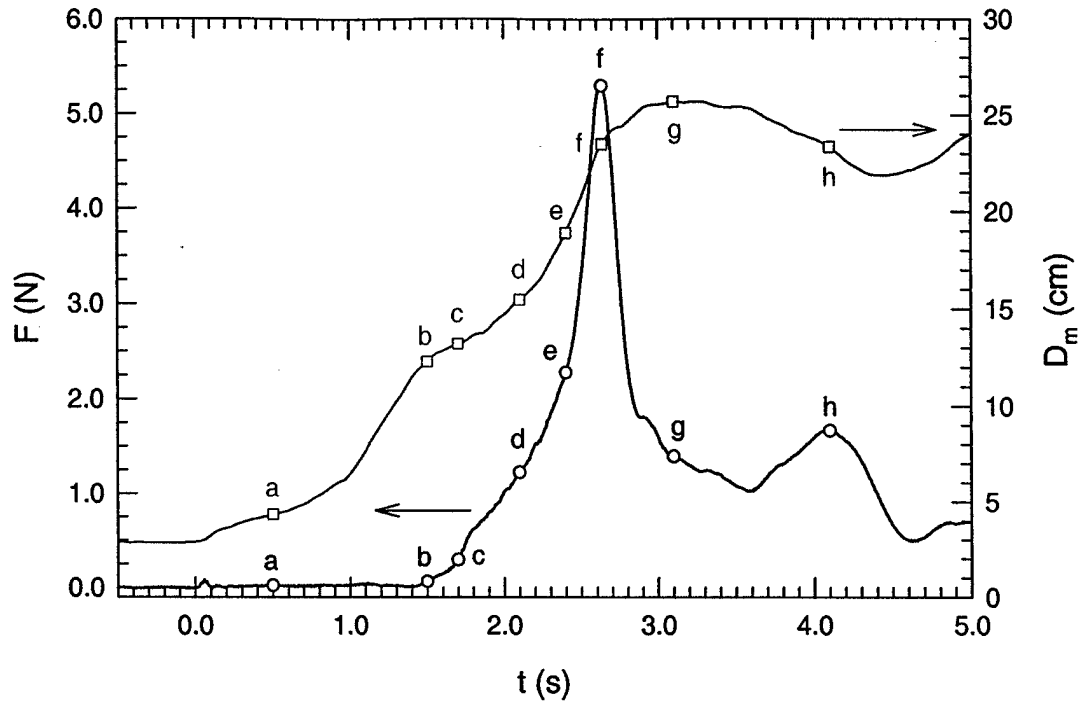
Figure 4.4. The opening force and diameter for a 30 cm canopy at a freestream velocity of 20 cm/s. Labeled points correspond with the images in Fig. 4.3.
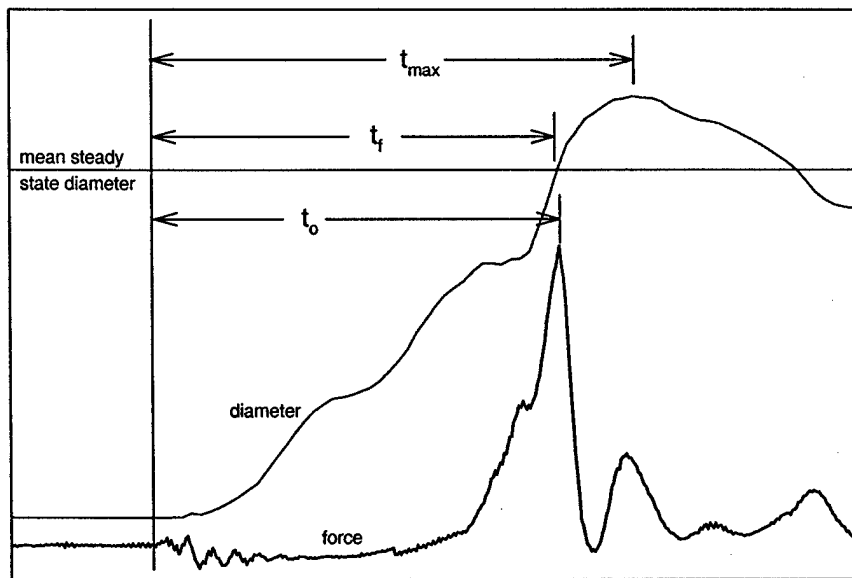
Figure 4.5. Definitions of characteristic times during canopy inflation.

95
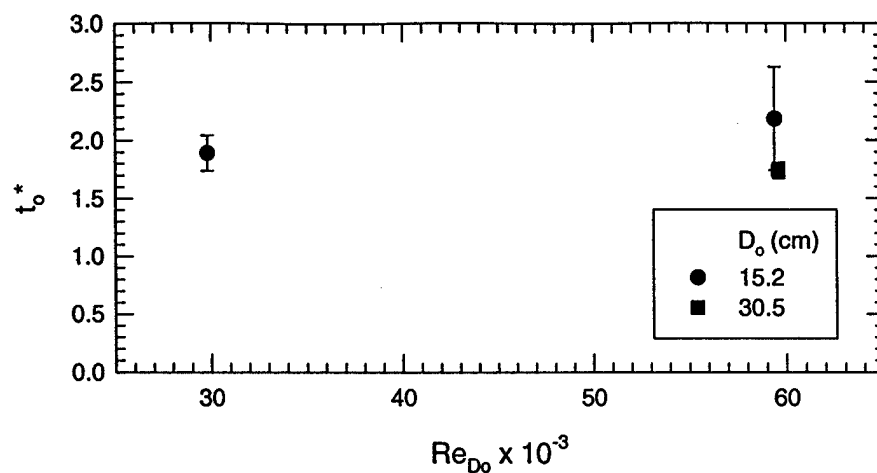
a)
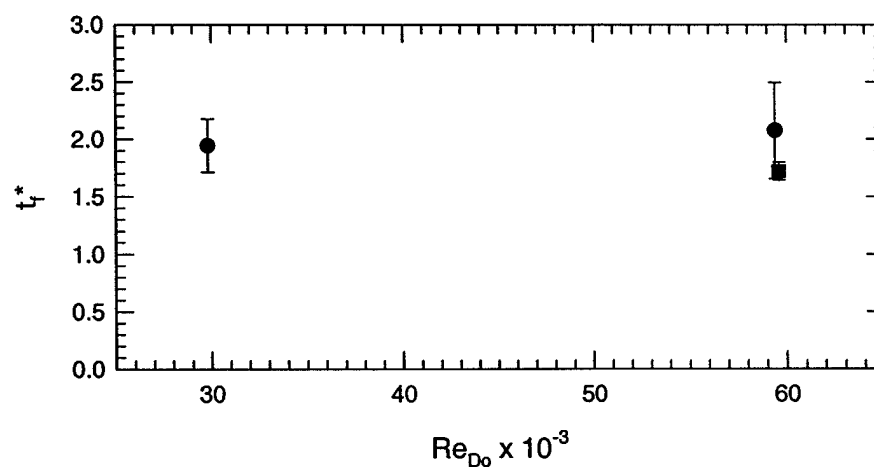
b)
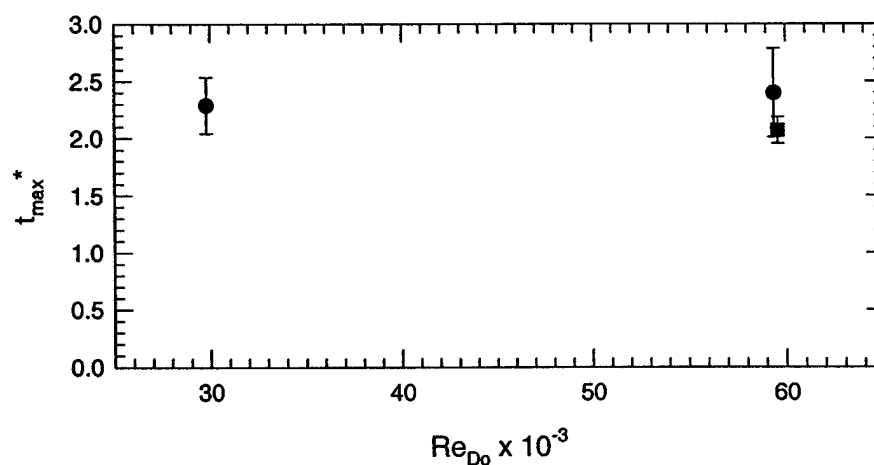
c)

Figure 4.6. Normalized characteristic times; a) opening time, b) filling time, c) maximum diameter time.
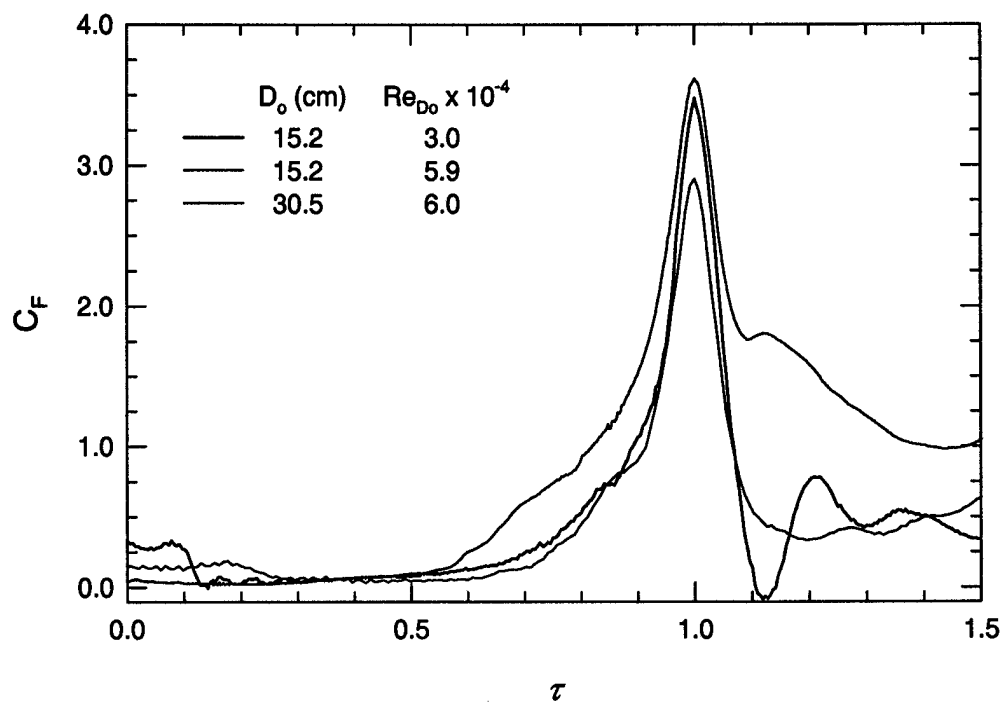
Figure 4.7. Ensemble-averaged force coefficient during canopy inflation of the three cases studied.
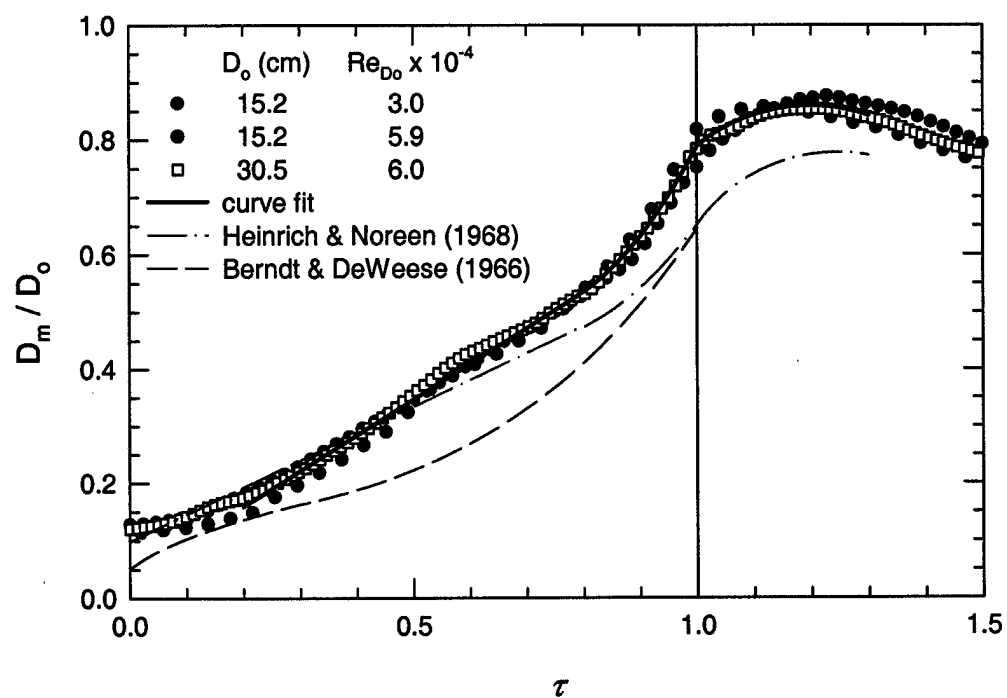
Figure 4.8. Normalized canopy diameter for the three cases studied and several empirical curve fits.
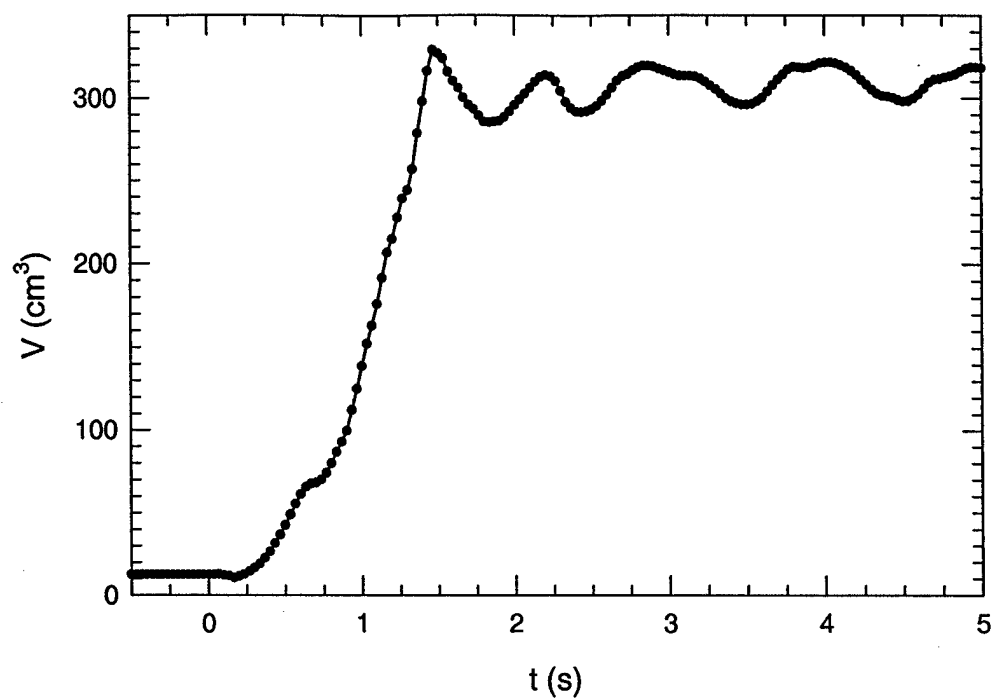
Figure 4.9. A sample of the volume enclosed by an inflating canopy with $D_o = 15.2$ cm and $Re_{Do} = 3.0 \times 10^4$.
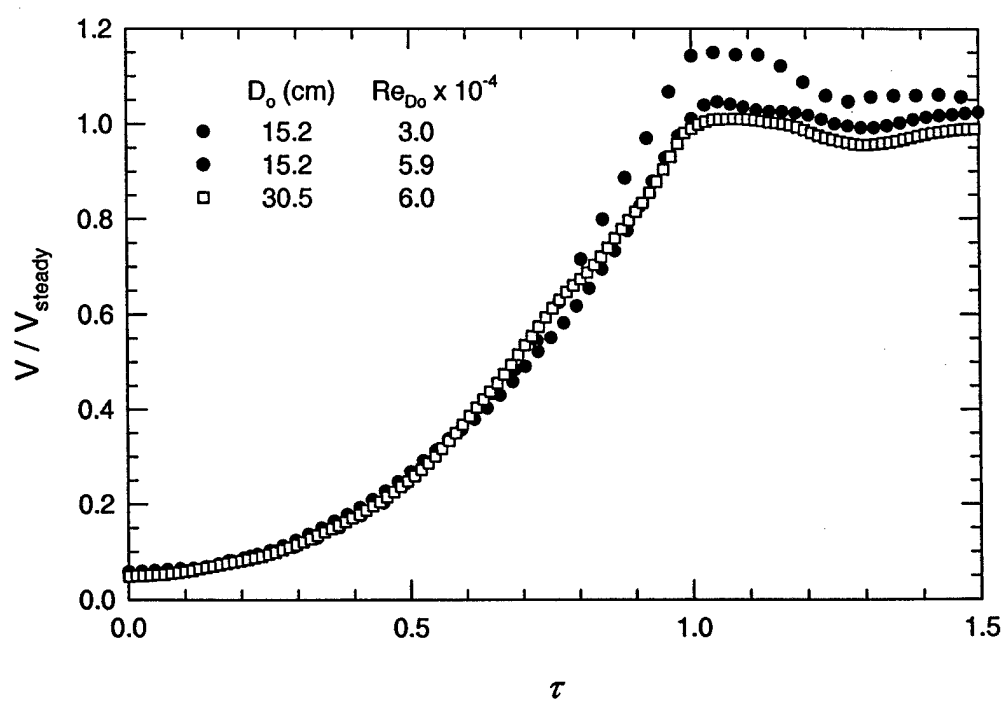
Figure 4.10. Ensemble-averaged enclosed canopy volume for the three cases studied.
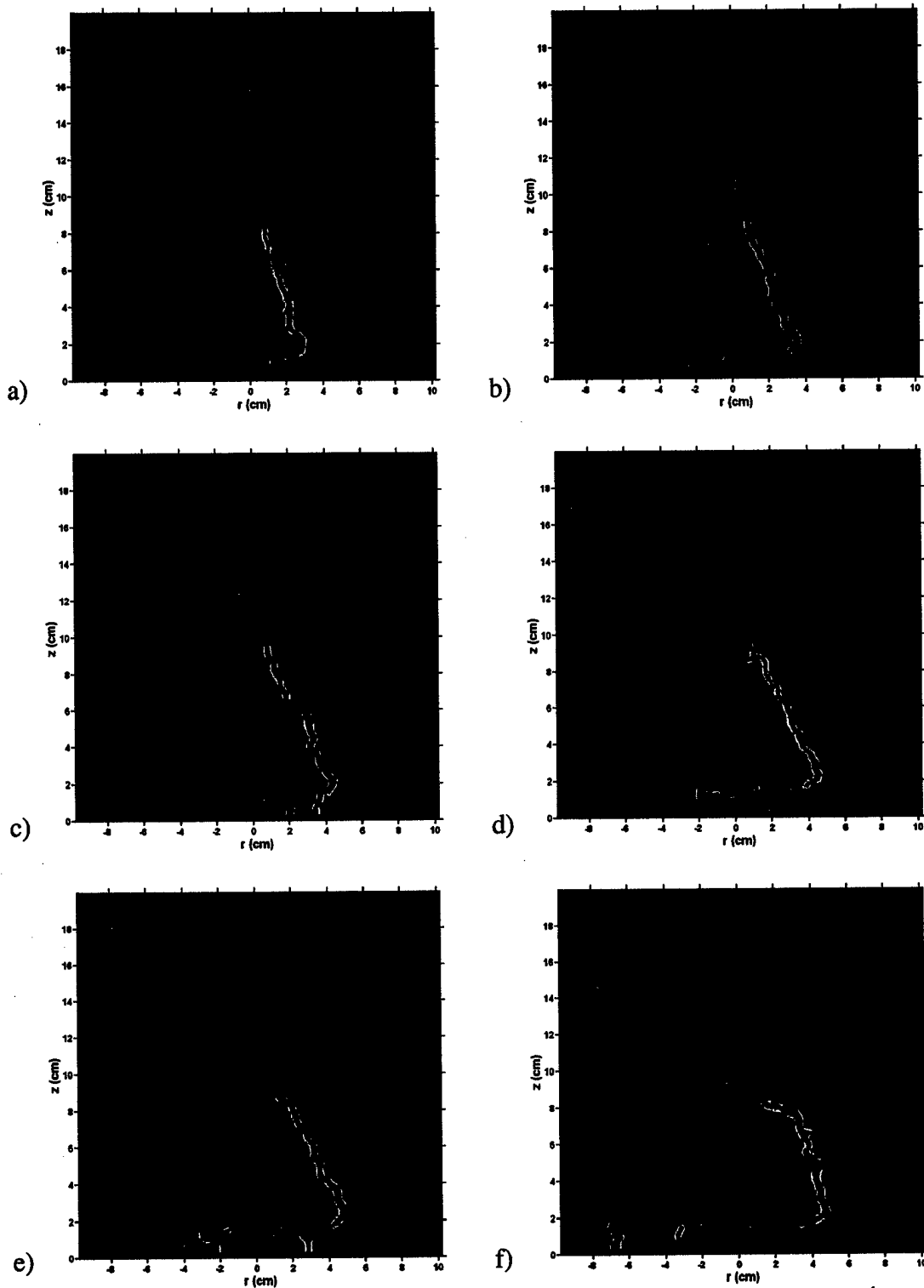
Figure 4.11. Vorticity field of an inflating 15 cm canopy at $Re_{Do} = 3.0 \times 10^4$. The positive vorticity levels are at $\bar{\omega} = 10 - 125$ s^{-1} with steps of 5 s^{-1}. The time for each image is a) $t = 0.40$ s, b) $t = 0.73$ s, c) $t = 0.93$ s, d) $t = 1.00$ s, e) $t = 1.07$ s, and f) $t = 1.13$ s. Stage II inflation ($t_2 = 1.10$ s) begins between images e and f.
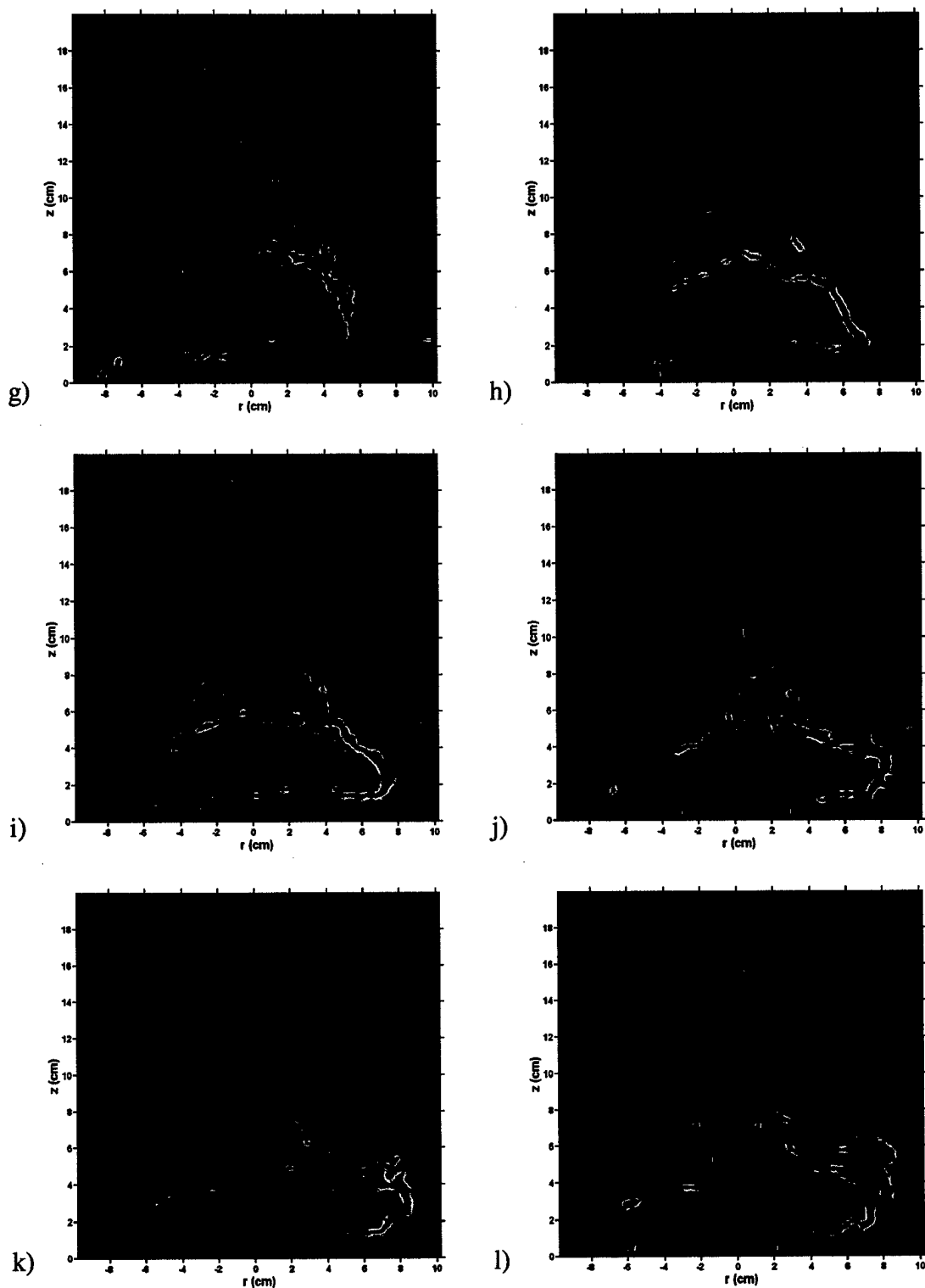
Figure 4.11, continued. The time for each image is g) $t = t_f = 1.27$ s, h) $t = t_o = 1.33$ s, i) $t = t_3 = 1.40$ s, j) $t = t_{max} = 1.53$ s, k) $t = 1.67$ s, and l) $t = 1.80$ s.

100
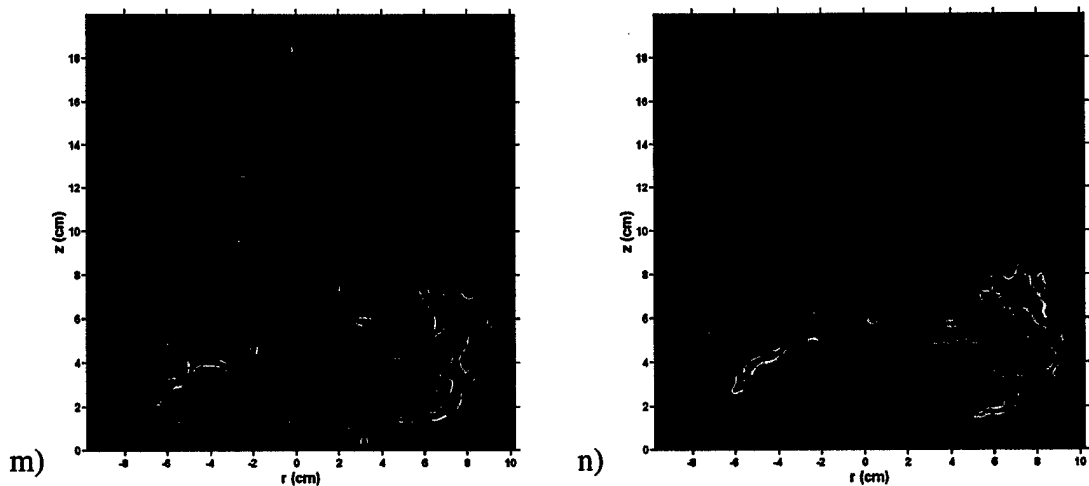
Figure 4.11, continued. The time for each image is m) $t = 1.93$ s and n) $t = 2.07$ s.
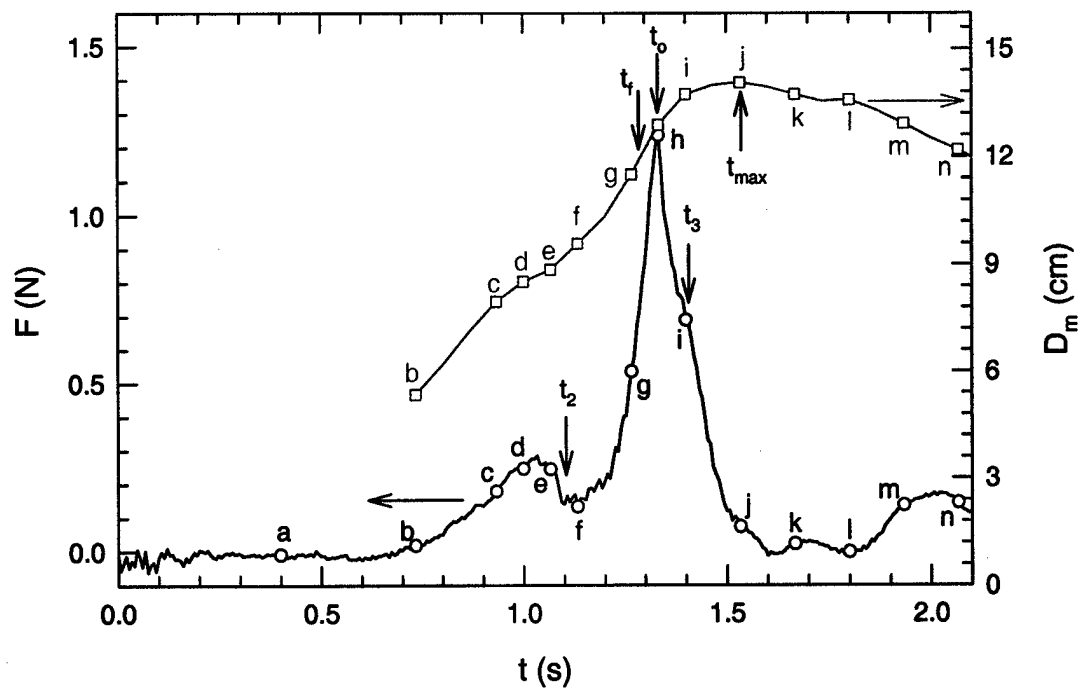
Figure 4.12. Force and diameter of canopy shown in Fig. 4.11. The letters correspond to the individual images in Fig. 4.11.
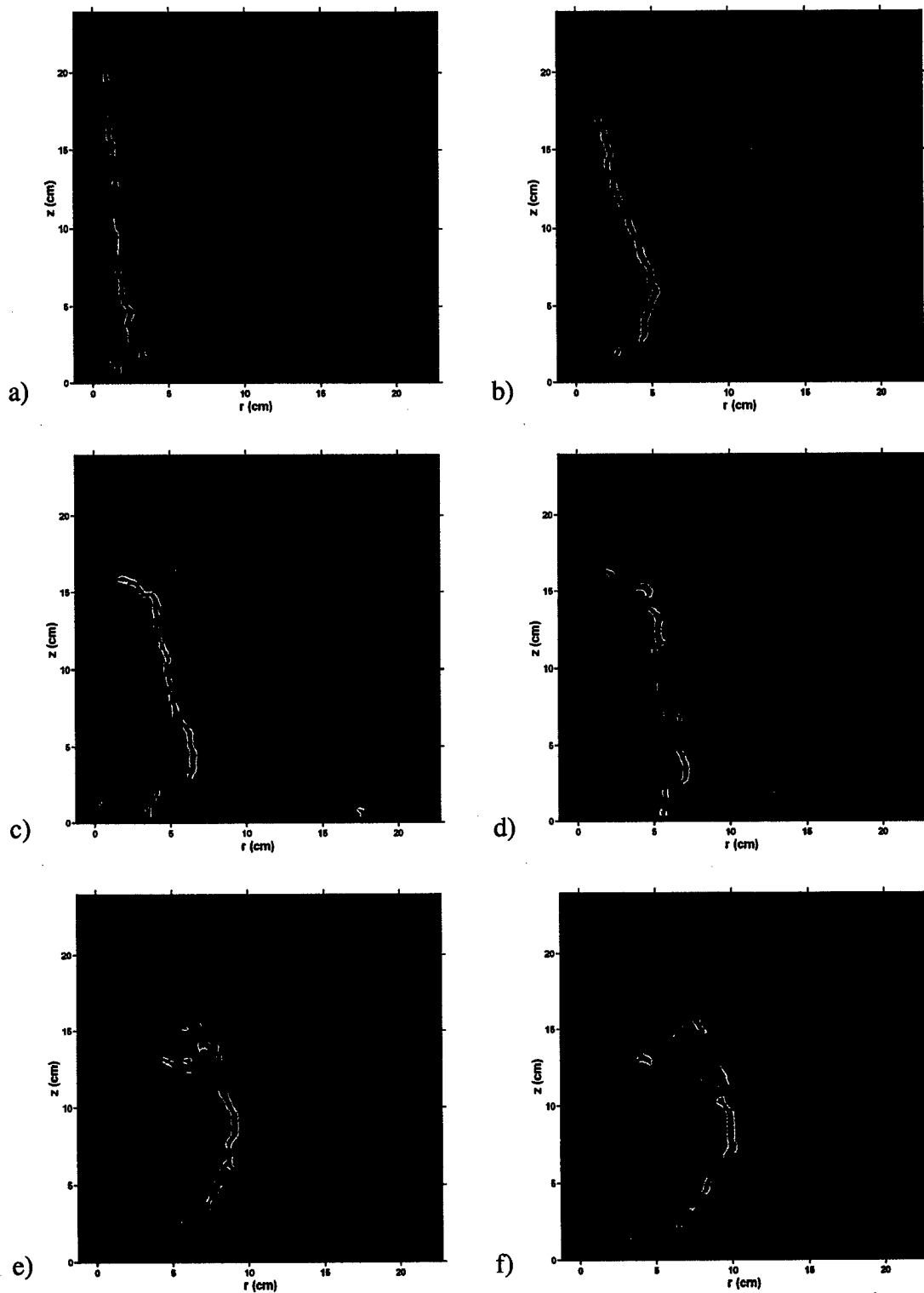
Figure 4.13. Vorticity field of an inflating 30 cm canopy at $Re_{Do} = 6.0 \times 10^4$. The positive vorticity levels are at $\vec{\omega} = 10 - 125$ s^{-1} with steps of 5 s^{-1}. The time for each image is a) $t = 0.40$ s, b) $t = 1.40$ s, c) $t = 2.13$ s, d) $t = t_2 = 2.27$ s, e) $t = 2.80$ s, and f) $t = 3.00$ s.

102
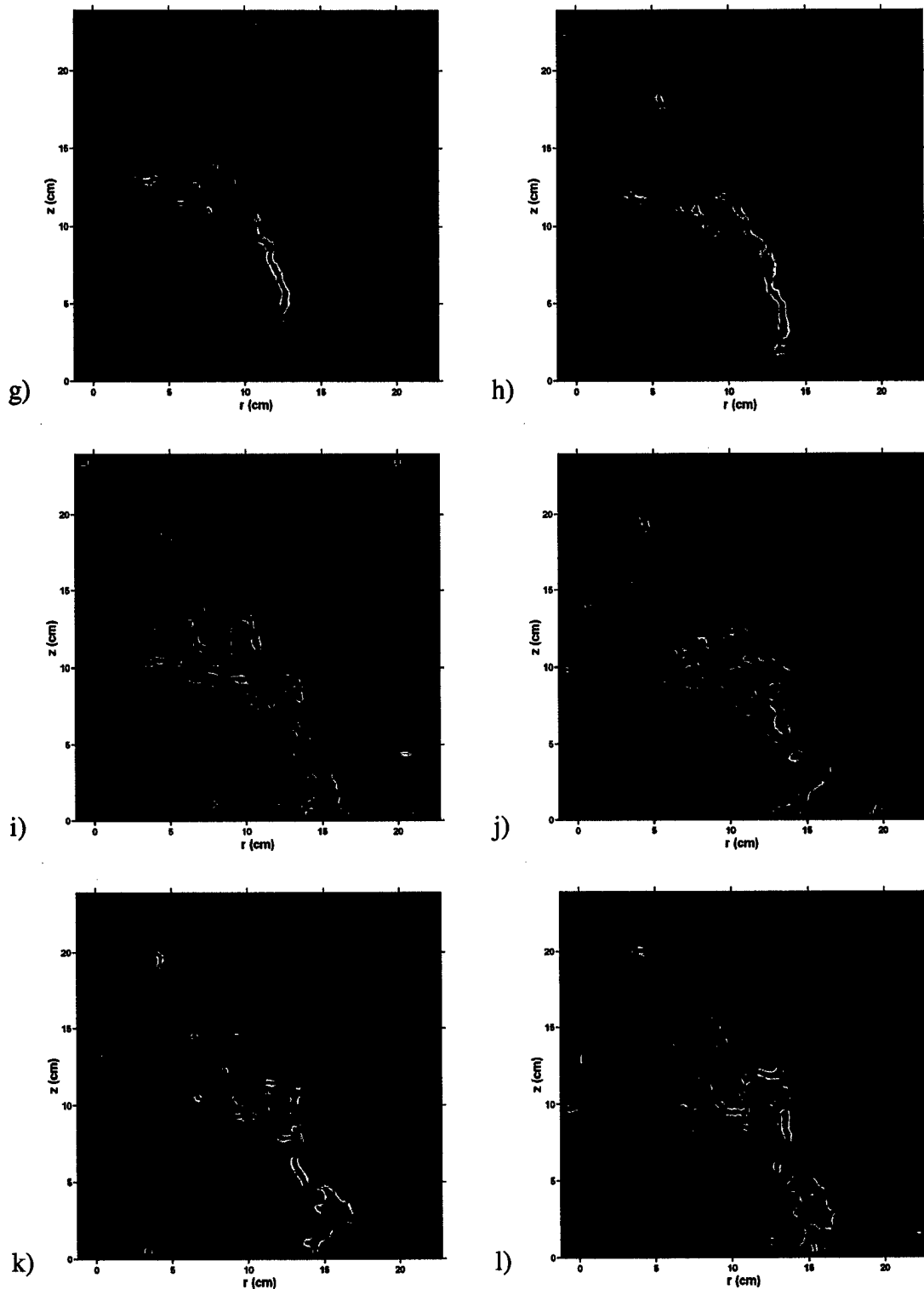
Figure 4.13, continued. The time for each image is g) $t = 3.33$ s, h) $t = 3.40$ s, i) $t = 3.53$ s, j) $t = 3.60$ s, k) $t = t_3 = 3.67$ s, and l) $t = t_{max} = 3.73$ s. The filling time ($t_f = 3.36$ s) occurs between images g and h. The opening time ($t_o = 3.55$ s) occurs between images i and j.
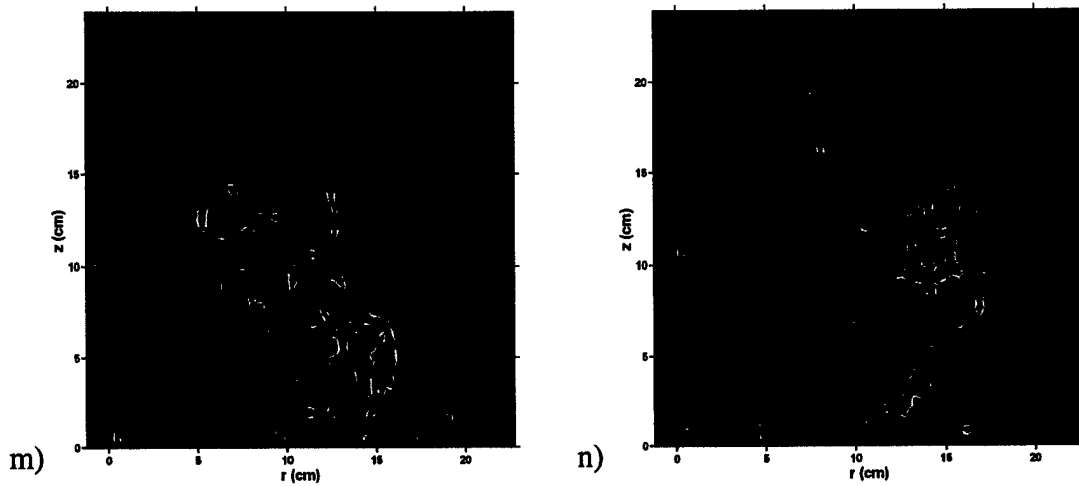
Figure 4.13, continued. The time for each image is m) $t = 4.00$ s and n) $t = 4.60$ s.
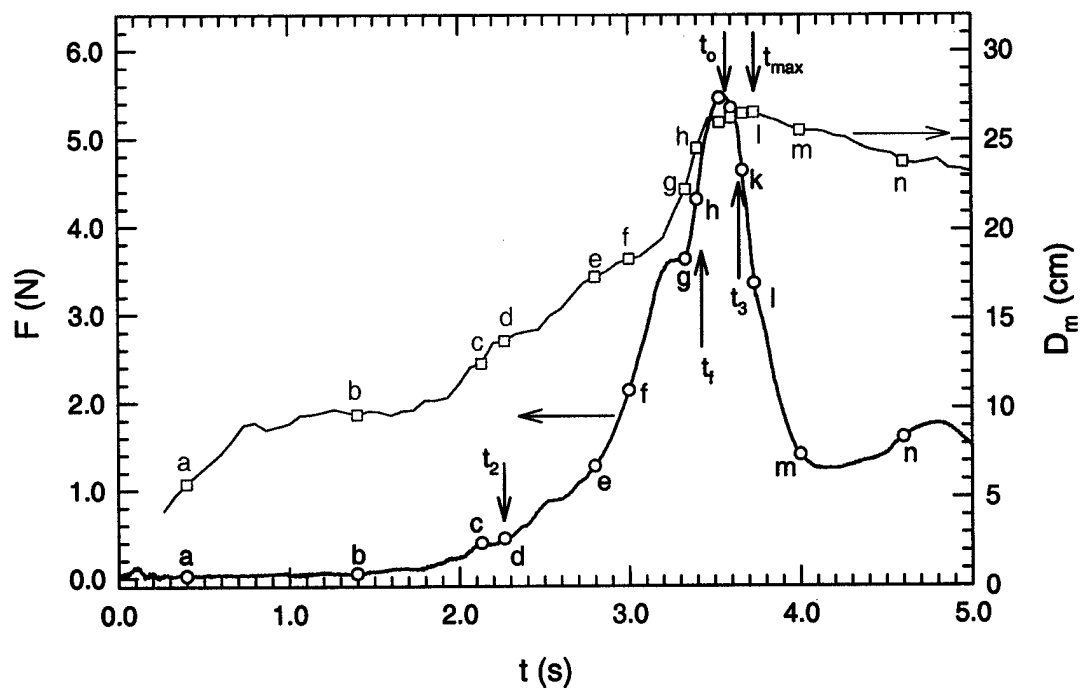
Figure 4.14. Force and diameter of canopy shown in Fig. 4.13. The letters correspond to the individual images in Fig. 4.13.
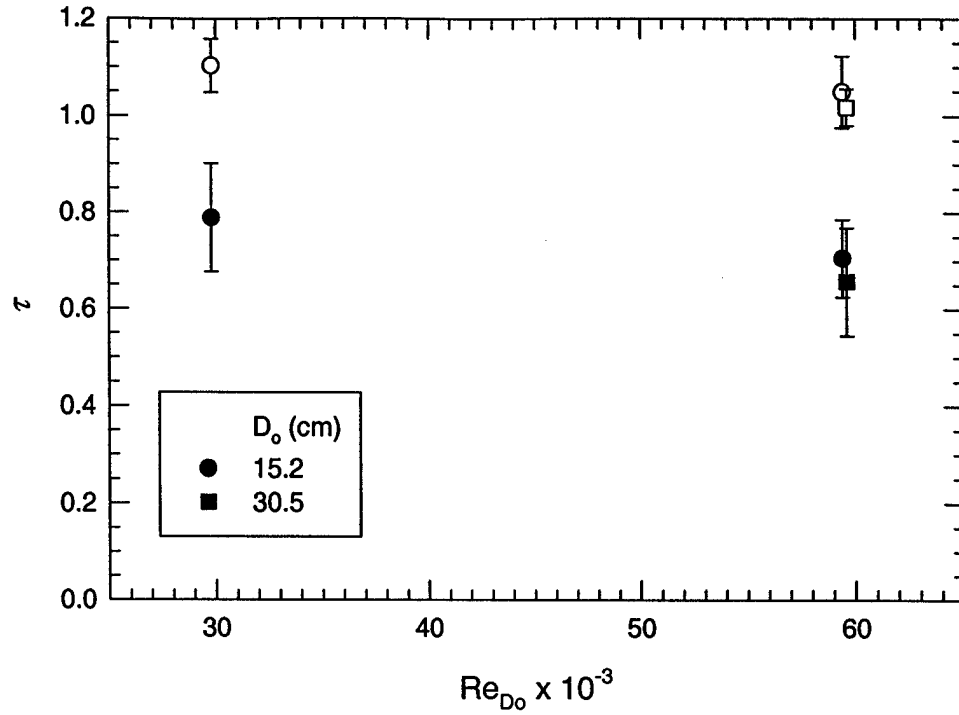
Figure 4.15. Normalized separation times. The solid symbols represent the onset of stage II, τ_2, and the open symbols represent the onset of stage III, τ_3.
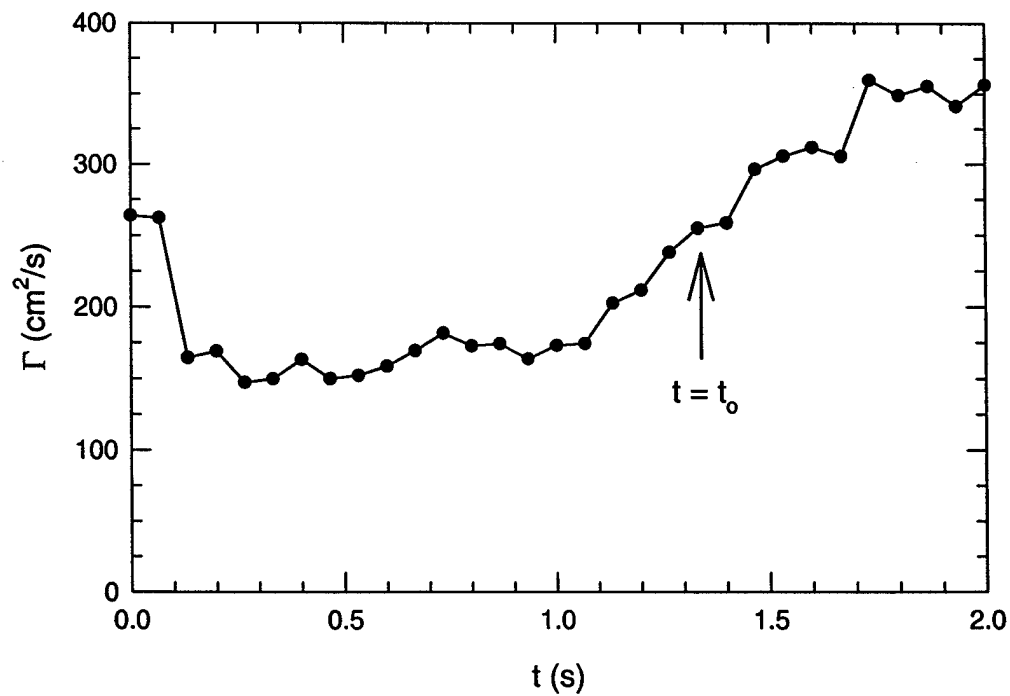
Figure 4.16. A sample of the circulation 15 cm canopy at $Re_{Do} = 3.0 \times 10^4$.

105
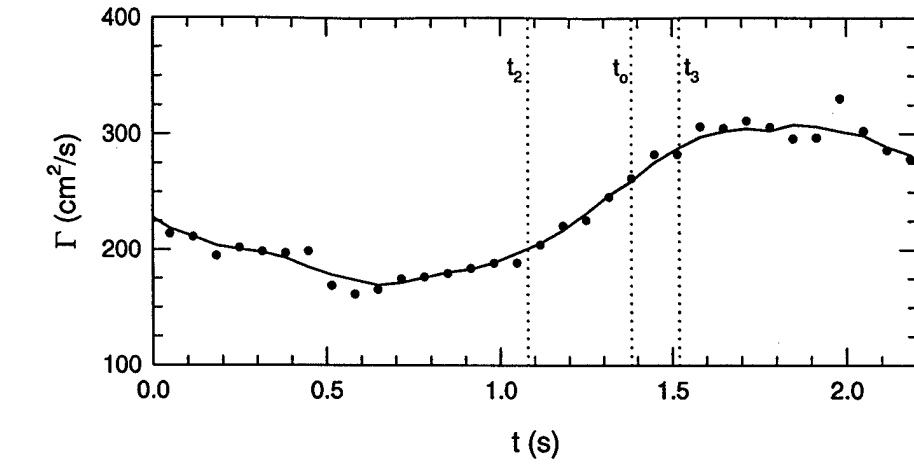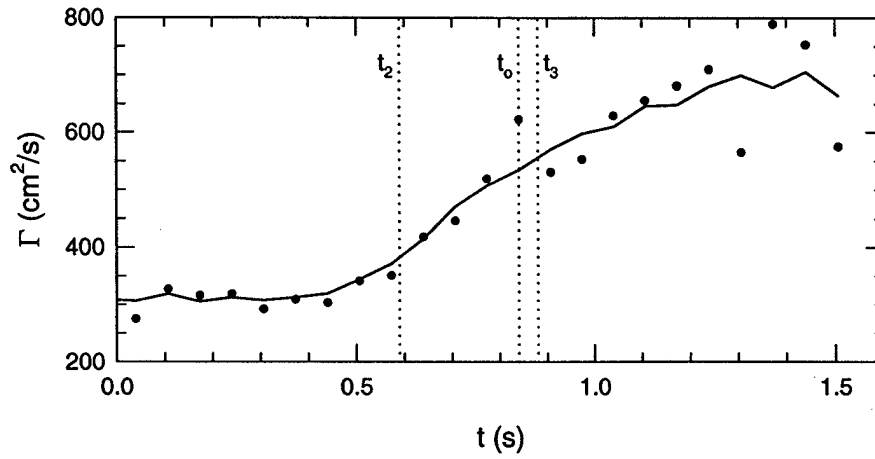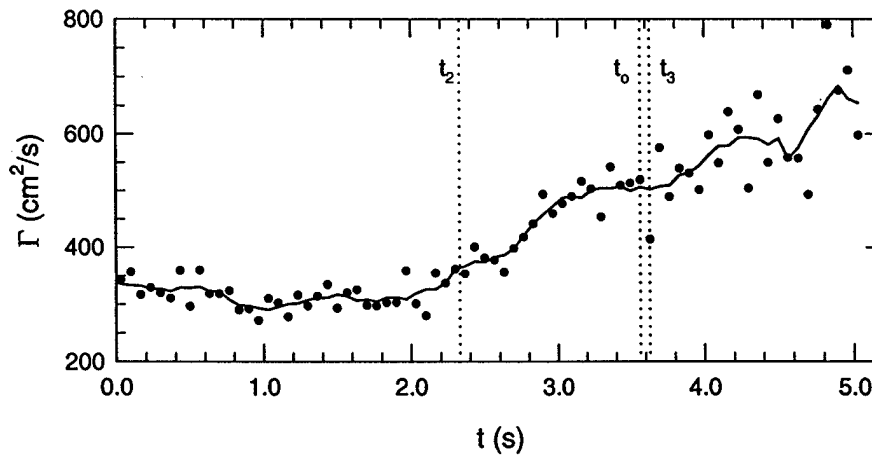
Figure 4.17. Average circulation of the canopy wake, a) 15 cm canopy at $Re_{Do} = 3.0 \times 10^4$; b) 15 cm canopy at $Re_{Do} = 5.9 \times 10^4$; c) 30 cm canopy at $Re_{Do} = 6.0 \times 10^4$. The solid line is a 5-point moving window average of the data and the vertical dotted lines are the noted times.

106
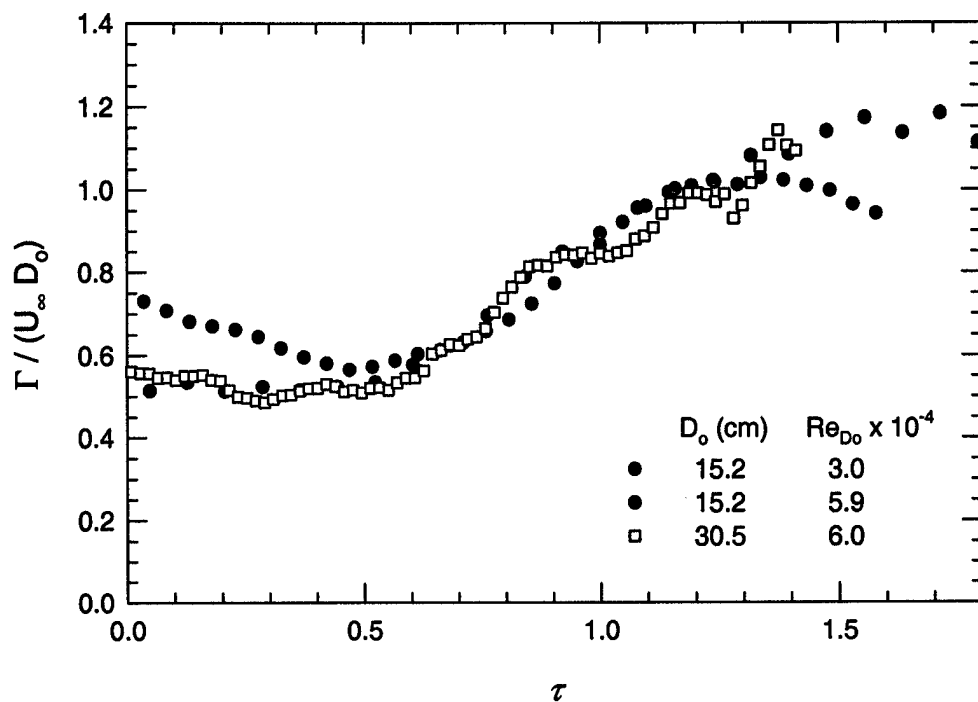
Figure 4.18. Normalized average circulation.
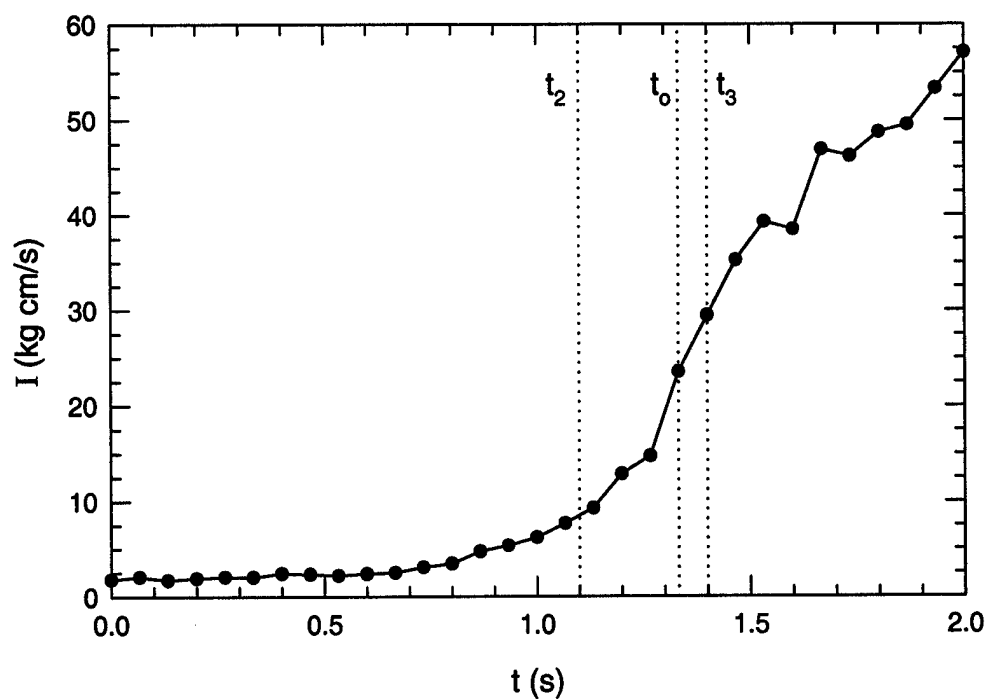
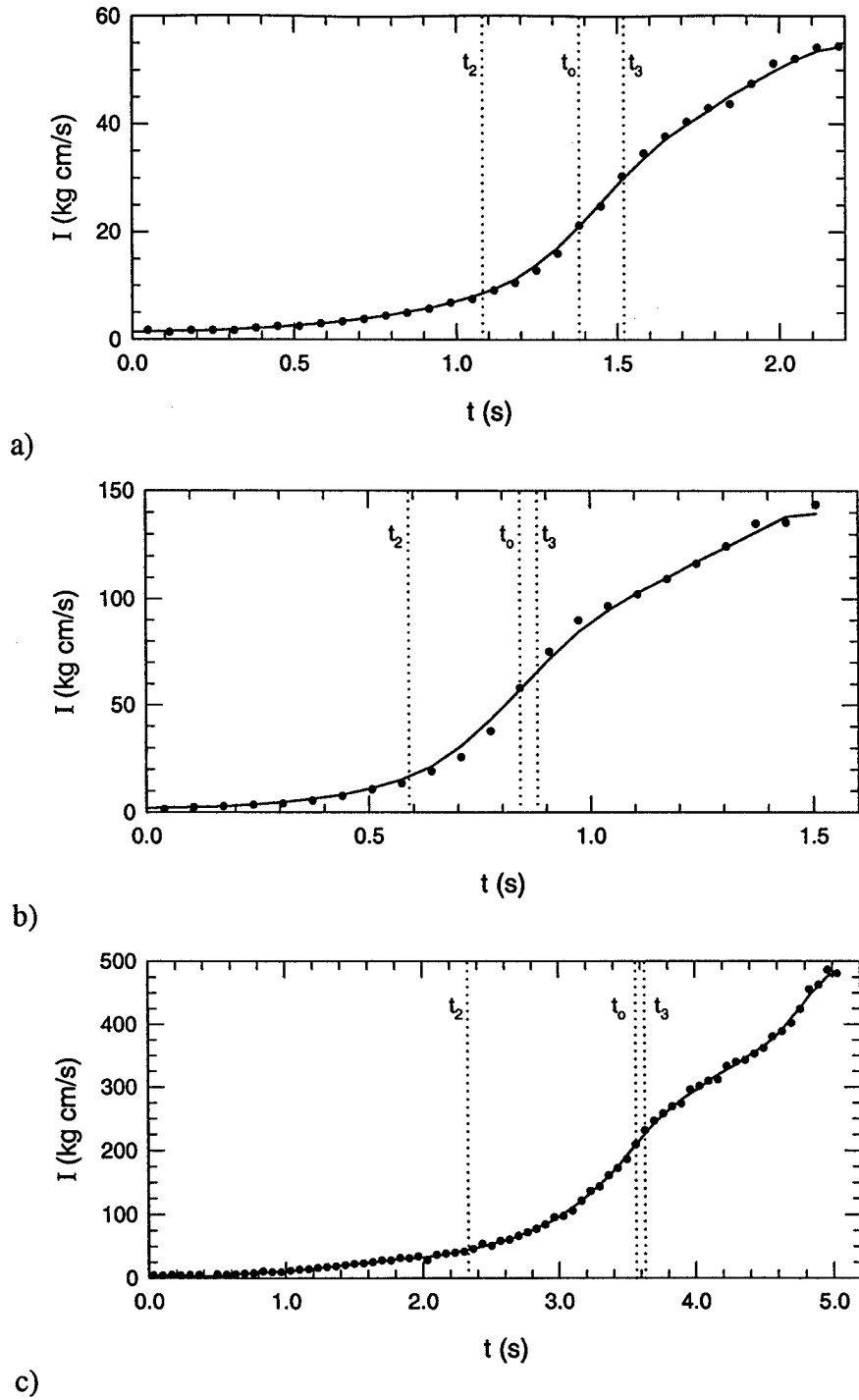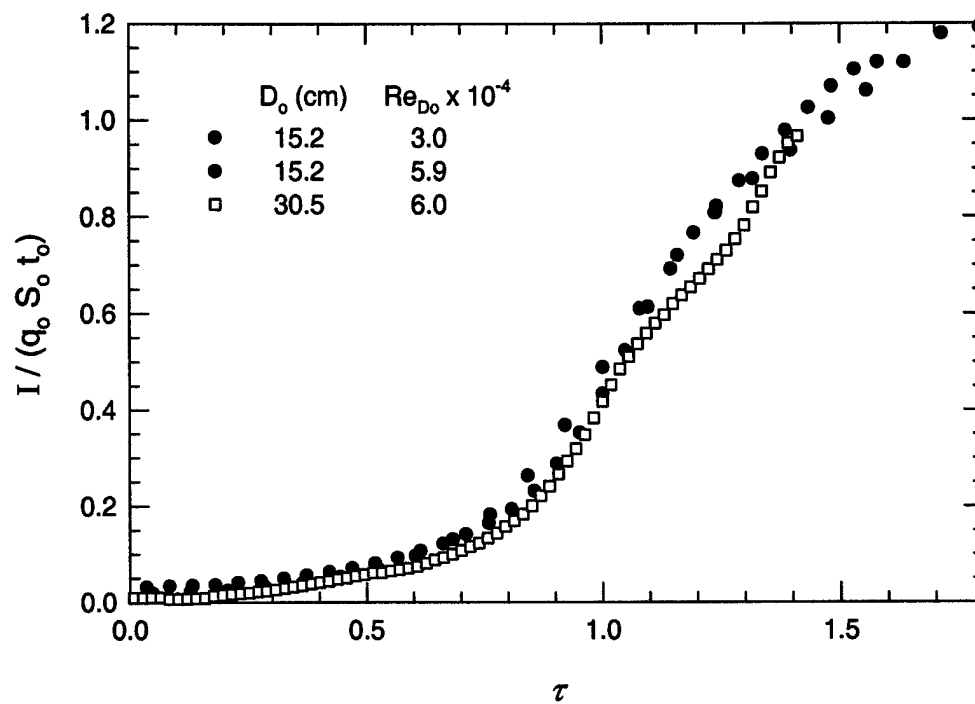Figure 4.19. A sample of the impulse for a 15 cm canopy at $Re_{Do} = 3.0 \times 10^4$.

107

a)

b)

c)

Figure 4.20. Average impulse of the canopy wake, a) 15 cm canopy at $Re_{Do} = 3.0 \times 10^4$; b) 15 cm canopy at $Re_{Do} = 5.9 \times 10^4$; c) 30 cm canopy at $Re_{Do} = 6.0 \times 10^4$. The solid line is a 5-point moving window average of the data and the vertical dotted lines are the noted times.
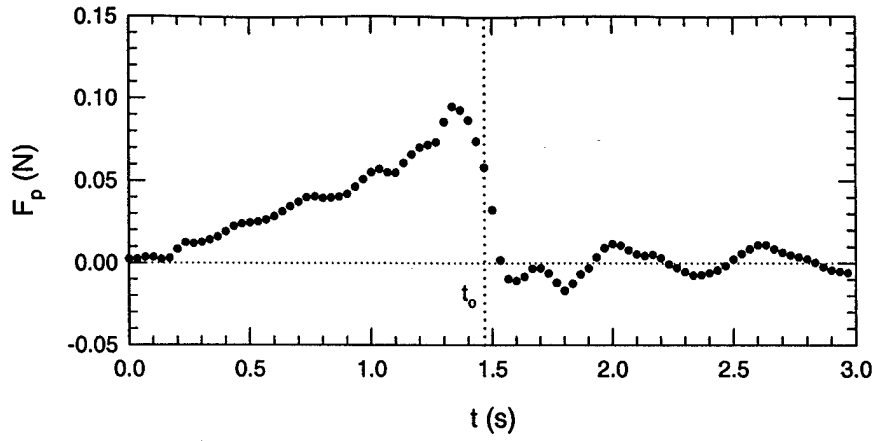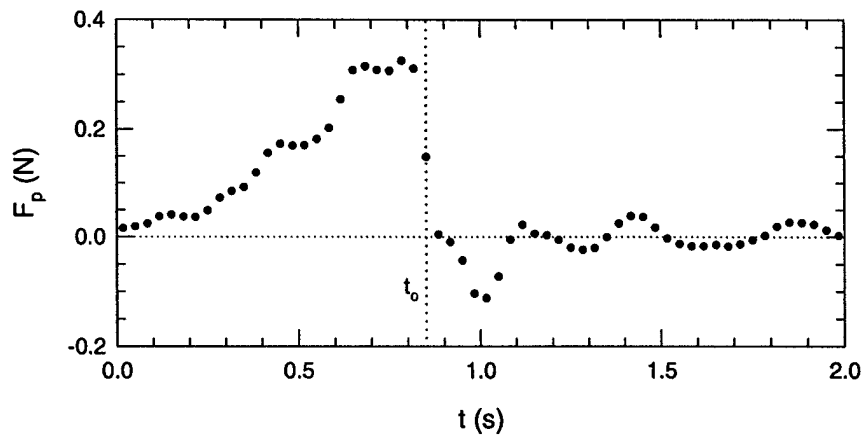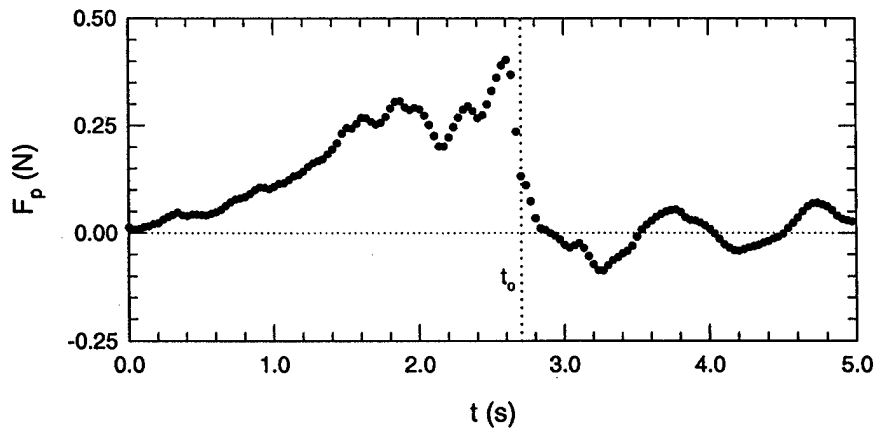
108

Figure 4.21. Normalized average impulse.

Figure 4.22. Average unsteady potential force, a) 15 cm canopy at $Re_{Do} = 3.0 \times 10^4$; b) 15 cm canopy at $Re_{Do} = 5.9 \times 10^4$; c) 30 cm canopy at $Re_{Do} = 6.0 \times 10^4$.
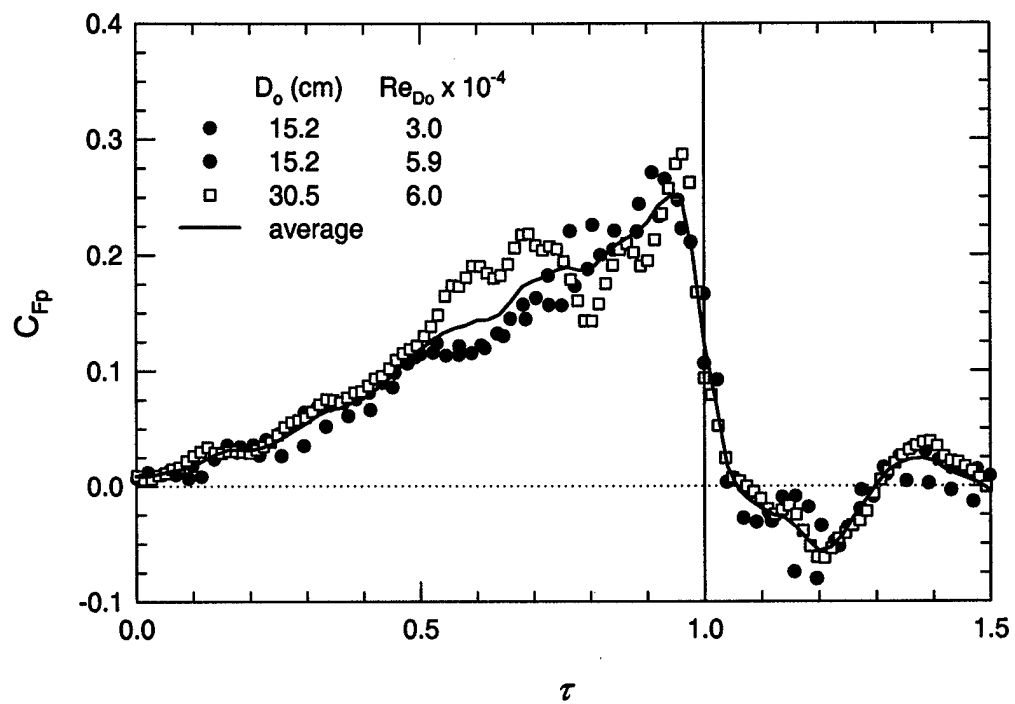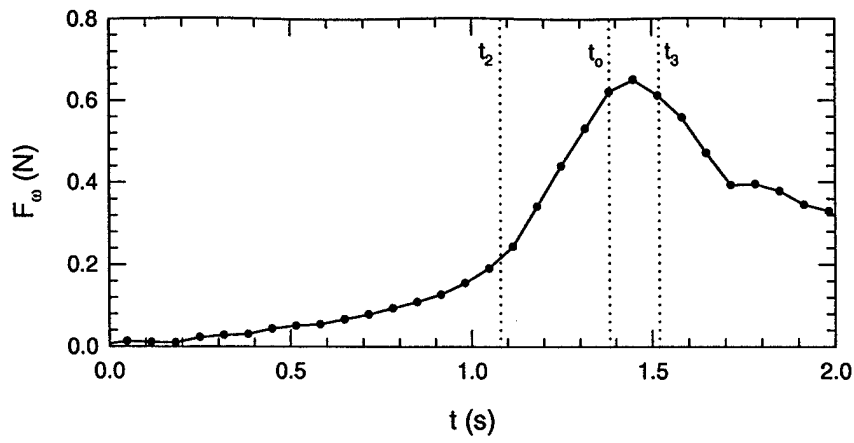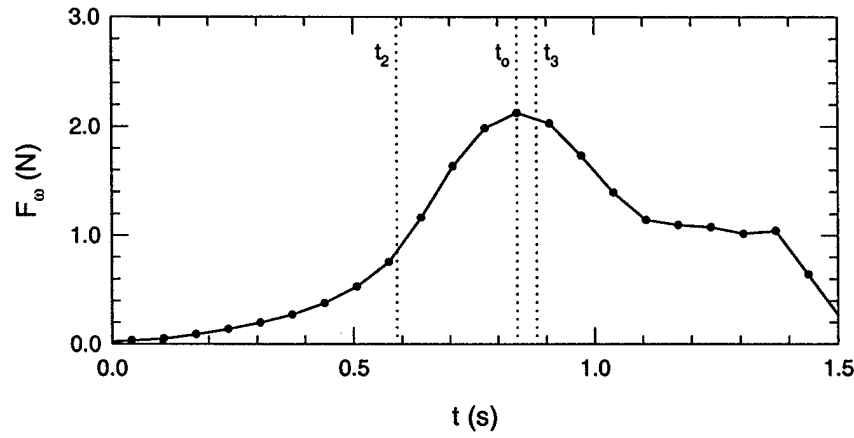
Figure 4.23. Unsteady potential force coefficient.

a)

b)

c)

Figure 4.24. Average force due to wake vorticity, a) 15 cm canopy at $Re_{Do} = 3.0 \times 10^4$; b) 15 cm canopy at $Re_{Do} = 5.9 \times 10^4$; c) 30 cm canopy at $Re_{Do} = 6.0 \times 10^4$.
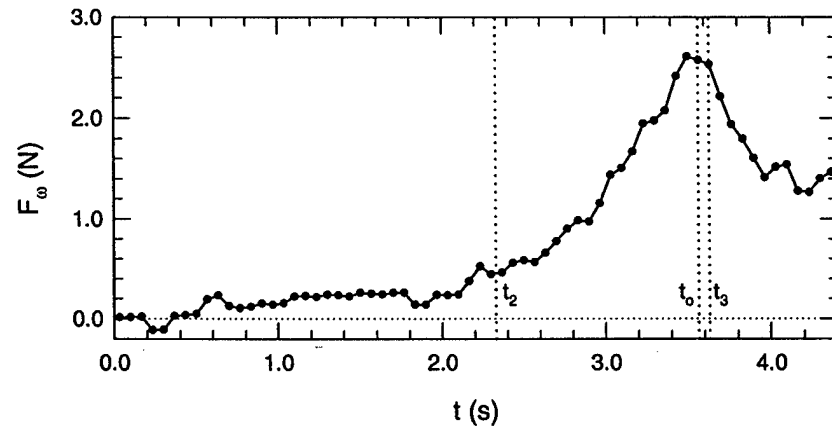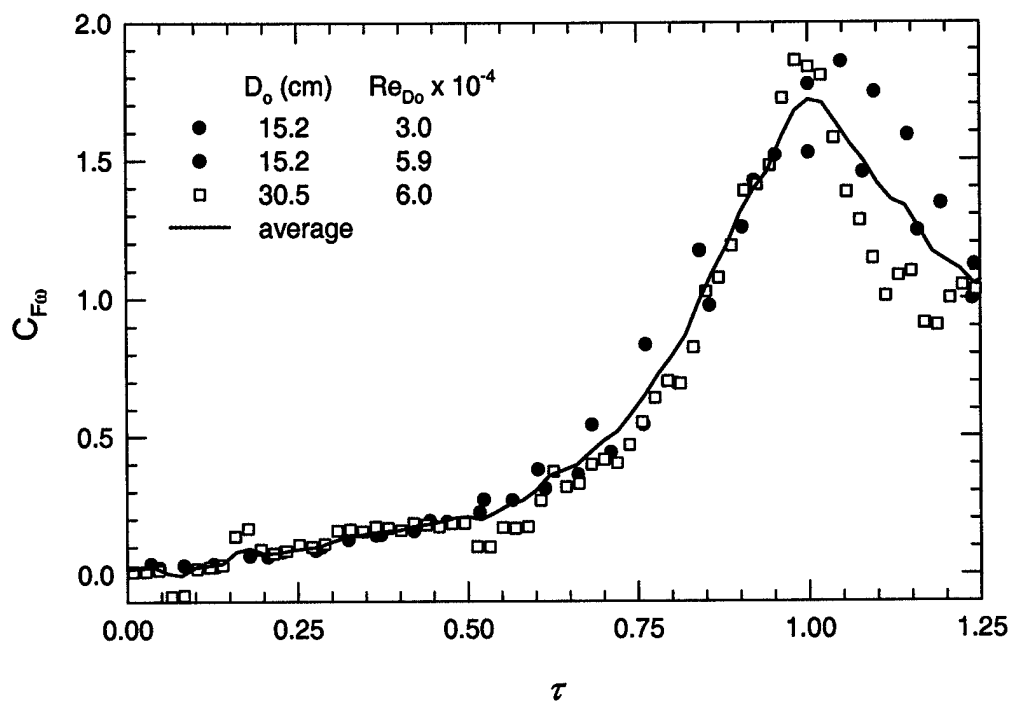
Figure 4.25. Force coefficient due to the impulse in the canopy wake.

Figure 4.26. Force coefficient estimates from the unsteady potential flow force and the force due to the vorticity in the wake for a 15 cm canopy at $Re_{Do} = 3.0 \times 10^4$.

113
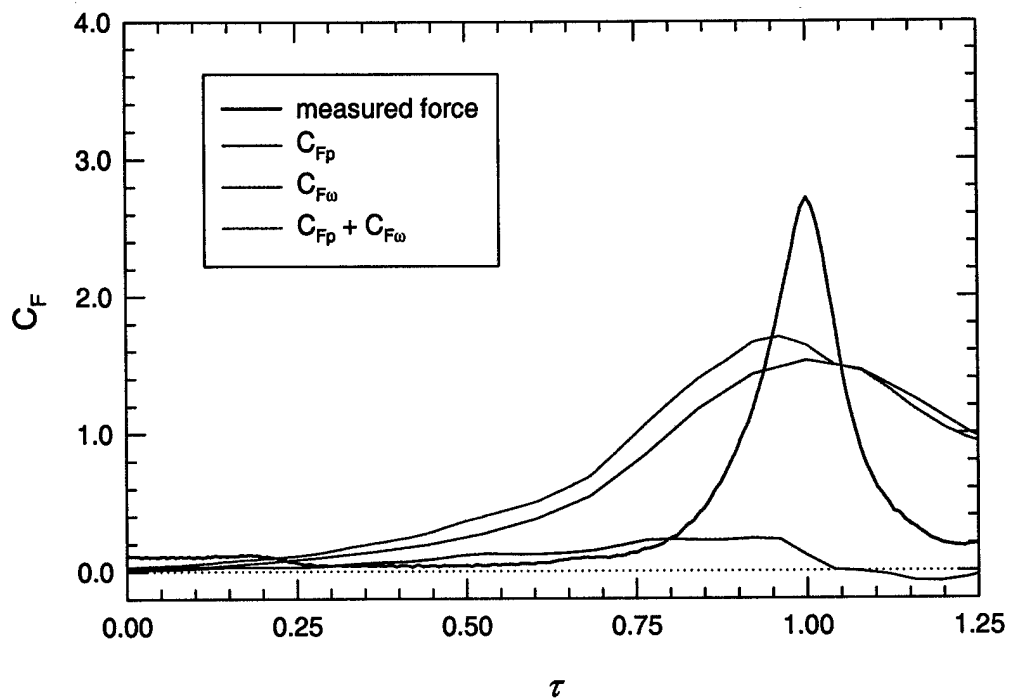
Figure 4.27. Force coefficient estimates from the unsteady potential flow force and the force due to the vorticity in the wake for a 15 cm canopy at $Re_{Do} = 5.9 \times 10^4$.
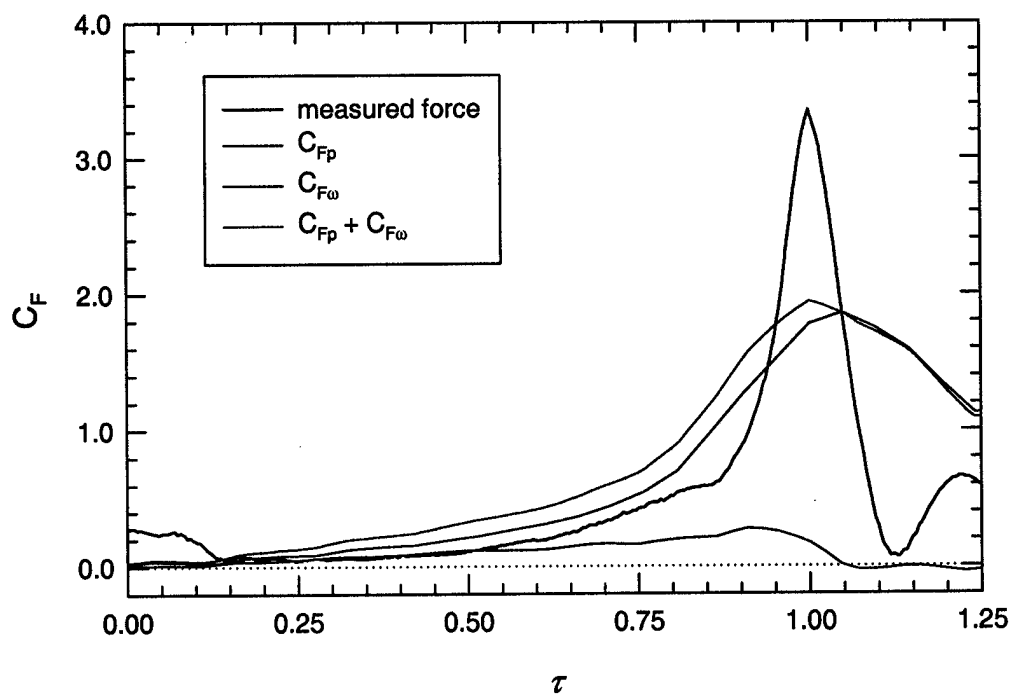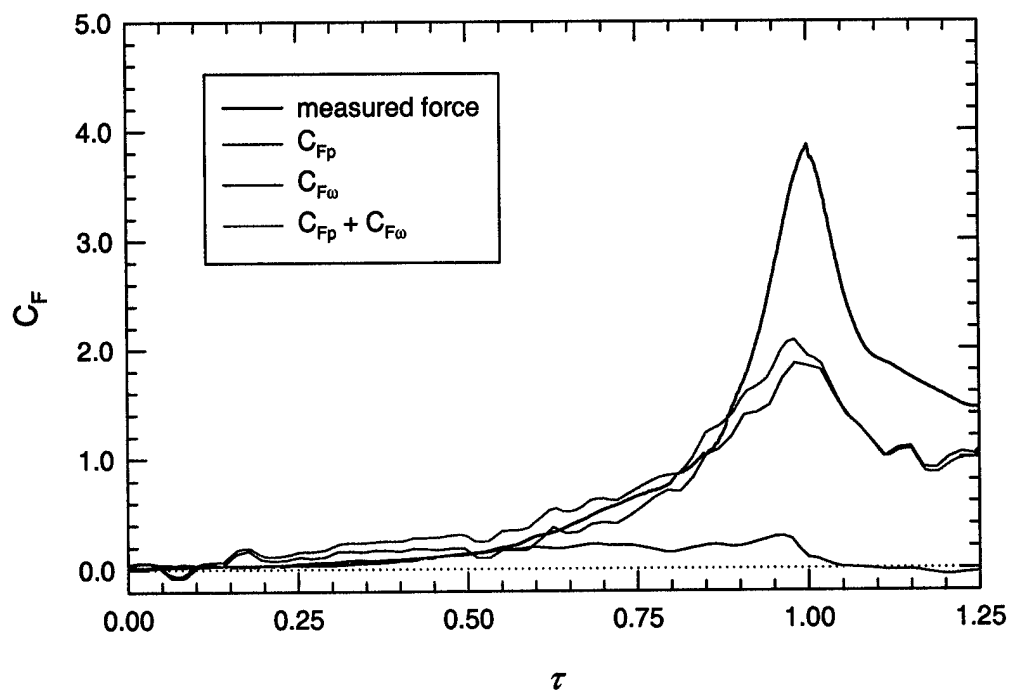

Figure 4.28. Force coefficient estimates from the unsteady potential flow force and the force due to the vorticity in the wake for a 30 cm canopy at $Re_{Do} = 6.0 \times 10^4$.

114
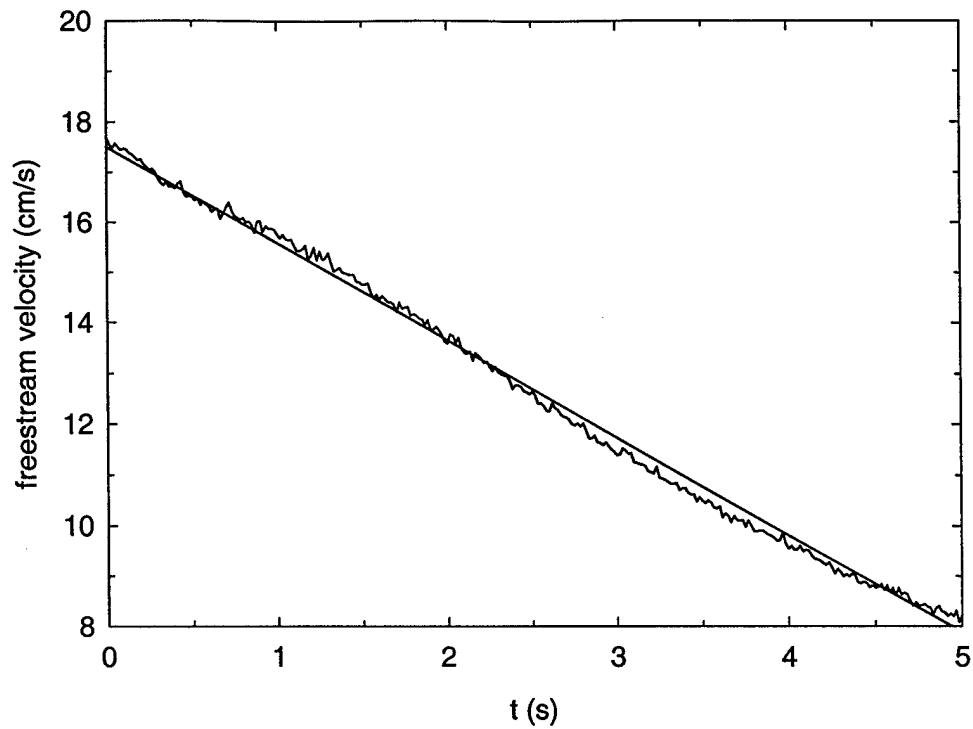
Figure 4.29. Freestream velocity in the water tunnel during a deceleration run.
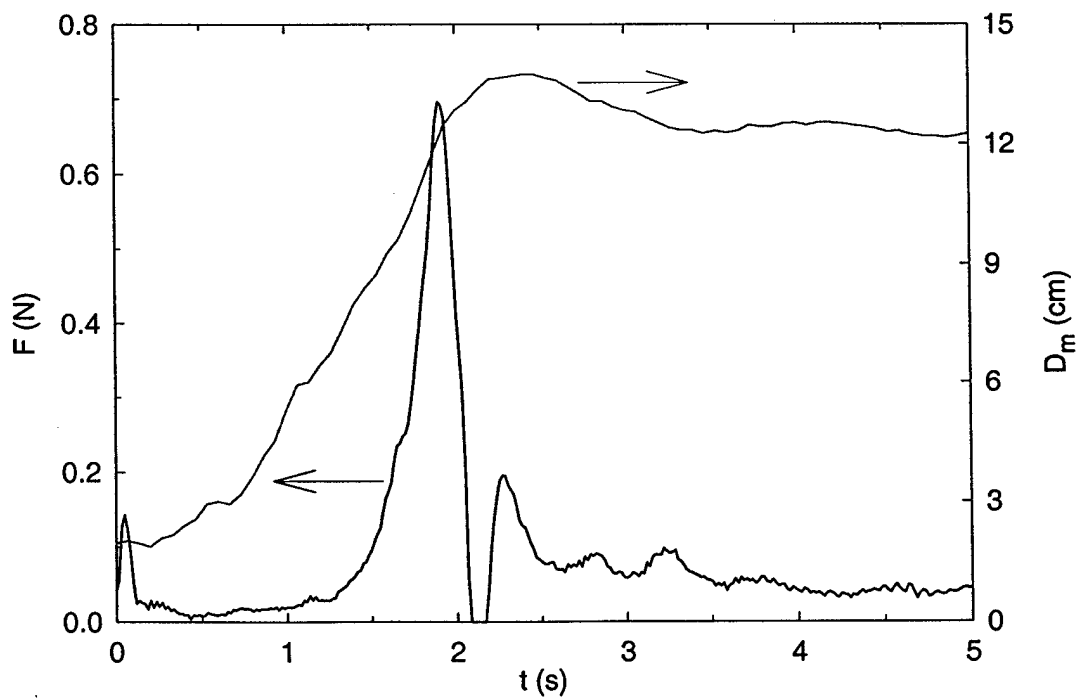
Figure 4.30. Diameter and drag for a canopy during a constant deceleration inflation.

115
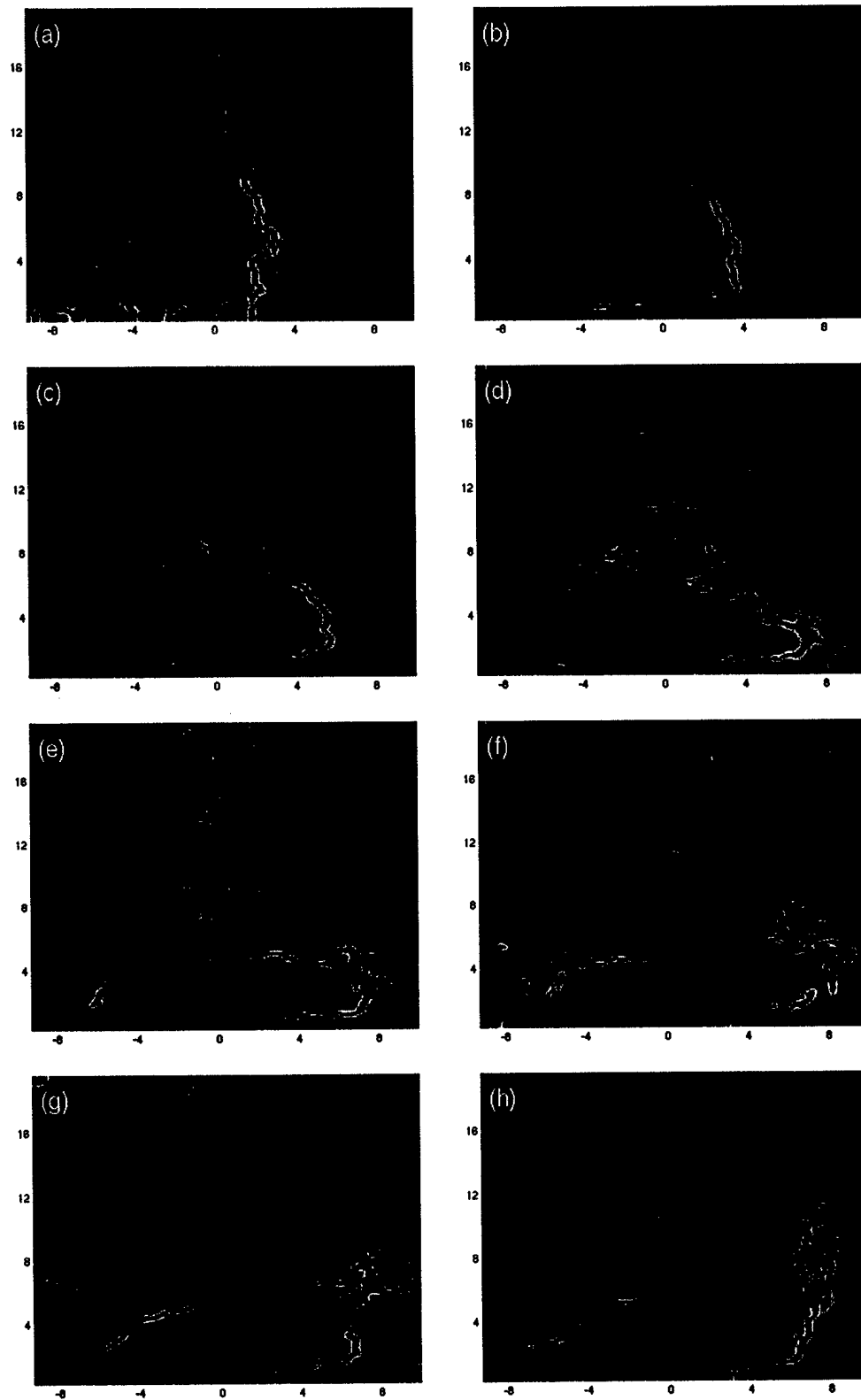
Figure 4.31. Vorticity contours for a constant deceleration inflation.

116
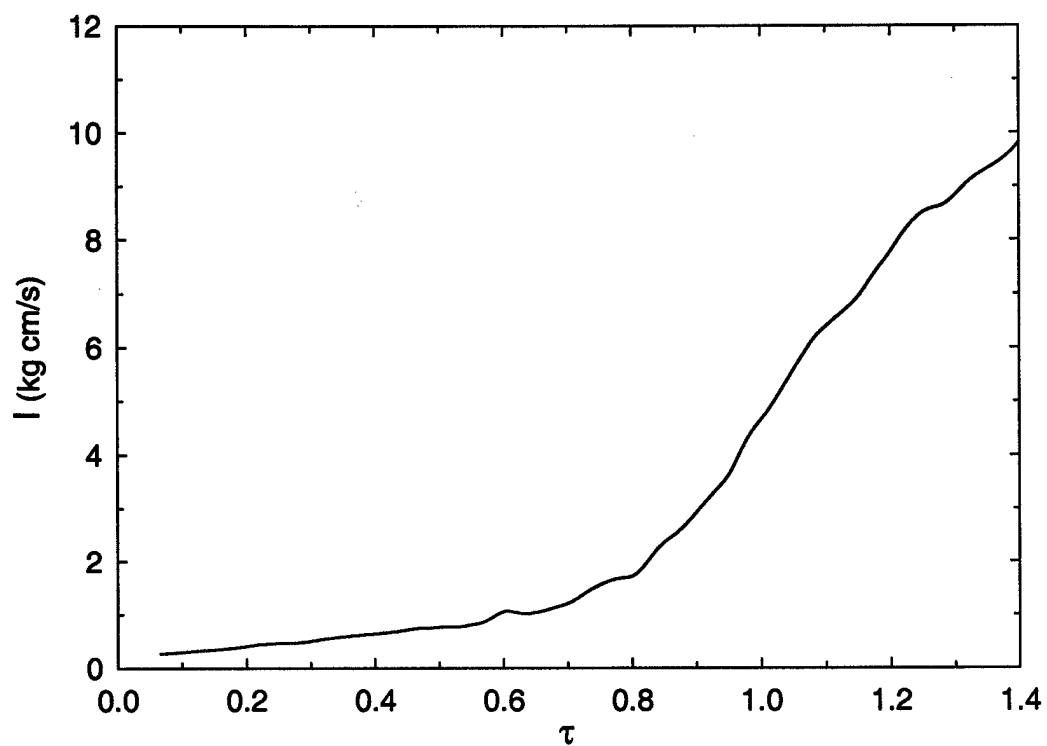
Figure 4.32. Ensemble averaged impulse as a function of time.
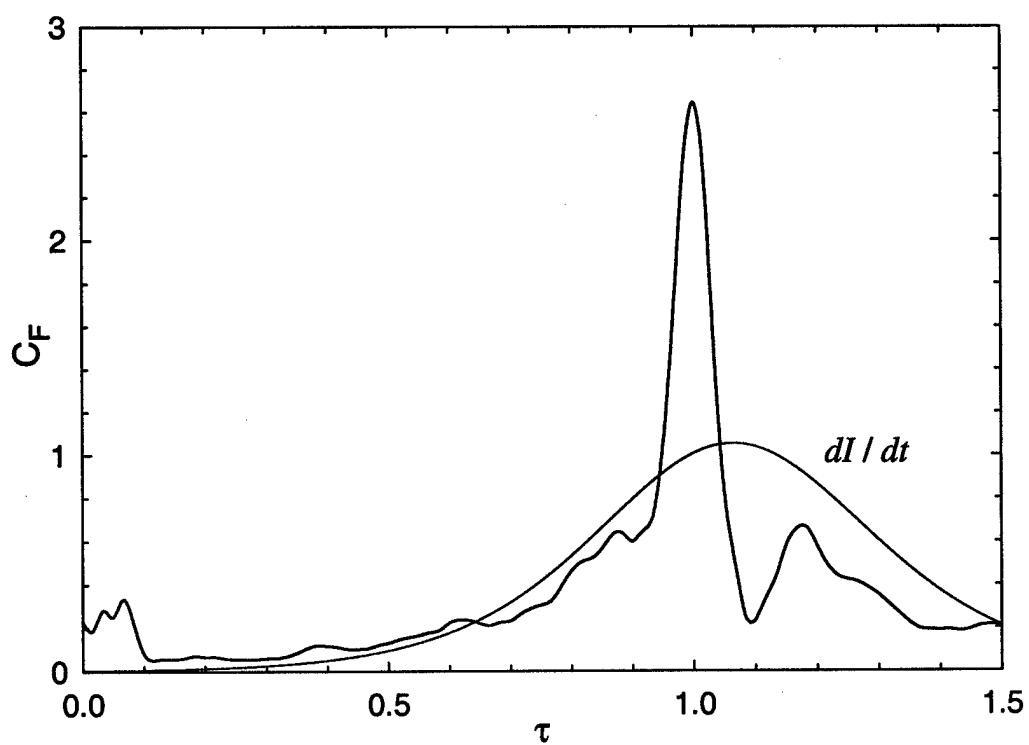
Figure 4.33. Measured force coefficient and the normalized time rate of change of impulse (red curve). The dynamic pressure is based on the initial velocity of 17 cm/s.

117

5. Conclusions

The flow field in the wake of a small-scale, flexible, generic, flat circular parachute canopy was investigated. The research focused on both the inflation phase and a fully inflated canopy. The canopy wake was measured by the PIV method in a diametrical plane. The vorticity field was computed from the velocity measurements. Simultaneous measurements of the drag force and the overall canopy geometry allowed for the correlation between the canopy dynamics and the near wake flow field.

The experiments were performed in a water tunnel to allow for longer canopy inflation times than would be present in a wind tunnel. The effects of Reynolds number and canopy size were examined by testing at three freestream velocities, which ranged from a nominal 20 cm/s to 40 cm/s, and two different canopy diameters (15.2 cm and 30.5 cm). The Reynolds number ranged from $3.0 - 6.0 \times 10^4$. A qualitative assessment of the canopy dynamics of the small-scale canopies showed characteristics similar to those of full-scale canopies, with the exception of the canopy dynamics during the early stages of inflation. These characteristics included a cyclic breathing for a fully inflated canopy, a large opening shock and the over-expansion of the canopy during the inflation. The geometric characteristics of the model in the early stage of the inflation process showed a marked difference from a full-scale inflation, a result of the higher stiffness of the canopy models.

Vortex shedding in the wake of the fully inflated canopy in a constant freestream was identified as the source of the cyclic expansion and contraction of the flexible canopy. This breathing motion, which has a normalized breathing frequency of 0.56 ± 0.03, to corresponds to the shedding of successive vortex rings into the wake. The

vortex shedding frequency was at a constant Strouhal number of 0.54 ± 0.04 over the studied Reynolds number range. The vortex shedding frequency was confirmed by two methods, namely by (*i*) spectral analysis of the radial velocity field in the near wake, and (*ii*) by tracking the position of the shed vortices in the wake. This shedding frequency has not been reported in past studies of disks or spheres. The flexible nature of the canopy structure may lend to the establishment of this shedding frequency. It was also observed that the vortex rings form symmetrically around the canopy at lower Reynolds numbers, and the ring formation becomes asymmetric with the vortex rings becoming twisted and distorted immediately as the Reynolds number approaches 6.0×10^4, the limit in our experiments. The fluctuating unsteady potential flow force of the fully inflated canopy is less than 20% of the *rms*-value of the drag force.

Examination of the near wake of an inflating canopy revealed that the kinematics of the flow field is an important element in the inflation process. During the early stages of the inflation, the boundary layer on the canopy surface remains attached to the canopy material and the wake of the canopy has minimal extent. This results in the canopy only experiencing a small amount of force from the fluid even though the canopy diameter has grown a substantial amount. Once the curvature of the canopy can no longer support an attached boundary layer, it begins to separate from the canopy surface near the apex region and the wake of the canopy increases in size with a corresponding increase in the force. At this point, the force rapidly increases to its maximum value as the separation point of the boundary layer moves upstream from the canopy apex region towards the canopy skirt. The force then plunges precipitously to levels observed in a fully inflated canopy in steady flow. Once the boundary layer gets separated at the canopy skirt, the

119

vorticity rolls-up into a vortex ring near the outer edges of the canopy. The canopy diameter is drawn out to its over-expanded state at this point and then proceeds to its cyclic breathing. The vortex ring is eventually shed from the canopy and is convected downstream where it initiates the establishment of an open wake.

The force on the canopy was estimated from an unsteady potential flow force and a force associated with the rate of change of the wake impulse. For a canopy in a constant freestream, the unsteady potential flow force can be estimated from the rate of change of the volume enclosed by the canopy. While the fluid impulse is a consequence of the vorticity containing portions of the flow. It was shown that the unsteady potential force contributed to no more than 10% of the measured peak opening force and only provided a significant portion of the opening force during the early stages of the inflation process. A large portion (~ 50%) of the total opening force was the result of the temporal rate of change of impulse. The formation of the wake behind the canopy during inflation results in the production of vorticity, and the bulk outward displacement of this vorticity causes the large opening shock force. Once the large amplitude displacement of the vorticity stops, the force approaches levels associated with a canopy in steady descent.

These conclusions show that the inflation process should not be exclusively modeled with an apparent mass term. Consideration of the temporal evolution of the vorticity generated during the inflation needs to be included in any modeling effort. Also, the data and knowledge obtained from this research should aid in the validation of the computational models now being developed.

120

6. References

Accorsi, M., Lu, K., Leonard, J., Benney, R., and Stein, K., "Issues in Parachute Structural Modeling: Damping and Wrinkling," 15th CEAS/AIAA Aerodynamic Deceleration Systems Technology Conference, Toulouse, France, June 8-11, 1999, AIAA Paper 99-1729.

Balligand, H. and Higuchi, H., "Experimental Investigation of the Wake Behind a Solid Disk," Sandia Report, SAND 90-7083, Dec., 1993.

Berndt, R.J. and DeWeese, J.H., "Filling Time Prediction Approach for Solid Cloth Type Parachute Canopies," Proceedings of AIAA 1st Aerodynamic Deceleration Systems Conference, Houston, TX, September 1966, pp. 17-32.

Berger, E., Scholz, D., and Schumm, M., "Coherent Vortex Structures in the Wake of a Sphere and a Circular Disk at Rest and Under Forced Vibrations," *Journal of Fluids and Structures*, Vol. 4, 1990, pp. 231-257.

Bigon, M. and Regazzoni, G., The Morrow Guide to Knots, trans. Piotrowska, M., Quill, 1982.

Bixby, H.W., Ewing, E.G., and Knacke, T.W., Recovery Systems Design Guide, U.S. Air Force, USAF Report AFFDL-TR-78-151, Dec. 1978.

Carrington, D., "Da Vinci's Parachute Flies," *BBC News Online*, June 27, 2000.

Cockrell, D.J., The Aerodynamics of Parachutes, AGARDograph No. 295, 1987.

DeSantis, G.C., "The Internal and External Flow Field Associated with Parachutes During Inflation," U.S. Army Natick Lab., Technical Report, 1970.

Eaton, J.A., "Added Fluid Mass and the Equations of Motion of a Parachute," *Aeronautical Quarterly*, Vol. 34, Aug. 1983, pp. 226-242.

French, K.E., "Inflation of a Parachute," *AIAA Journal*, Vol. 1, No. 11, 1963, pp. 2615-2617.

French, K.E., "Model Law for Parachute Opening Shock," *AIAA Journal*, Vol. 2, No. 12, 1964, pp. 2226-2228.

Fuchs, H.V., Mercker, E., and Michel, U., "Large-Scale Coherent Structures in the Wake of Axisymmetric Bodies," *Journal of Fluid Mechanics*, Vol. 93, Part 1, 1979, pp. 185-207.

Gharib, M., Rambod, E., and Shariff, K., "A Universal time scale for vortex ring formation," *Journal of Fluid Mechanics*, Vol. 360, 1998, pp. 121-140.

Heinrich, H.G. and Noreen, R.A., "Analysis of Parachute Opening Dynamics with Supporting Wind Tunnel Experiments," AIAA 2nd Aerodynamic Deceleration Systems Conference, El Centro, California, Sept. 23-25, 1968, AIAA Paper 68-924.

Heinrich, H.G., "Opening Time of Parachutes Under Infinite-Mass Conditions," *Journal of Aircraft*, Vol. 6, No. 3, May-June, 1969, pp. 268-272.

Heinrich, H.G. and Noreen, R.A., "Analysis of Parachute Opening Dynamics with Supporting Wind-Tunnel Experiments," *Journal of Aircraft*, Vol. 7, No. 4, 1970, pp. 341-347.

Heinrich, H.G. and Hektner, T.R., "Flexibility as a Model Parachute Performance Parameter," *Journal of Aircraft*, Vol. 8, No. 9, 1971, pp. 704-709.

Heinrich, H.G., "A Linearised Theory of Parachute Opening Dynamics," *Aeronautical Journal*, Dec. 1972, pp. 723-731.

Higuchi, H. and Takahashi, F., "Flow Past Two-Dimensional Ribbon Parachute Models," *Journal of Aircraft*, Vol. 26, No. 7, 1989, pp. 641-649.

Higuchi, H., "Visual Study on Wakes Behind Solid and Slotted Axisymmetric Bluff Bodies," *Journal of Aircraft*, Vol. 28, No. 7, 1991, pp. 427-430.

Higuchi, H., Anderson, R.W., and Zhang, J., "Three-Dimensional Wake Formations Behind a Family of Rectangular Polygonal Plates," *AIAA Journal*, Vol. 34, No. 6, 1996, pp. 1138-1145.

Higuchi, H., Balligand, H., and Strickland, J.H., "Numerical and Experimental Investigations of the Flow Over a Disk Undergoing Unsteady Motion," *Journal of Fluids and Structures*, Vol. 10, No. 7, 1996, pp. 705-719.

Ibrahim, S.K., "Potential Flowfield and Added Mass of the Idealized Hemispherical Parachute," *Journal of Aircraft*, Vol. 4, No. 2, 1967, pp. 96-100.

Johari, H. and Desabrais, K.J., "Scaling for Solid Cloth Parachutes," 16th AIAA Aerodynamic Deceleration Systems Technology Conference, Boston, Massachusetts, May 21-24, 2001, AIAA Paper 2001-2007.

Karamcheti, K., Principles of Ideal-Fluid Aerodynamics, Robert E. Krieger Publishing, 1980.

Klimas, P.C., "Internal Parachute Flow," *Journal of Aircraft*, Vol. 9, No. 4, 1972, pp. 313-314.

Klimas, P.C., "Helium Bubble Survey of An Opening Parachute Flowfield," *Journal of Aircraft*, Vol. 10, No. 9, 1973, pp. 567-569.

Klimas, P.C., "Fluid Mass Associated with an Axisymmetric Parachute Canopy," *Journal of Aircraft*, Vol. 14, No. 6, 1977, pp. 577-580.

Klimas, P.C. and Rogers, D.F., "Helium Bubble Survey of a Parachute-Opening Flowfield Using Computer Graphics Techniques," *Journal of Aircraft*, Vol. 14, No. 10, 1977, pp. 952-958.

Klimas, P.C., "Inflating Parachute Canopy Differential Pressures," *Journal of Aircraft*, Vol. 16, No. 12, 1979, pp. 861-862.

Knacke, T.W., Parachute Recovery Systems Design Manual, Para Publishing, 1992.

Lamberson, D., Higuchi, H., and van Rooij, M., "Characteristics of Flow within Concave-nosed Bodies," 15th CEAS/AIAA Aerodynamic Deceleration Systems Technology Conference, Toulouse, France, June 8-11, 1999, AIAA Paper 99-1738.

Lee, C.K., "Modeling of Parachute Opening: An Experimental Investigation," *Journal of Aircraft*, Vol. 26, No. 5, 1989, pp. 444-451

Lee, C.K, "Radial Reefing Method for Accelerated and Controlled Parachute Opening," *Journal of Aircraft*, Vol. 31, No. 5, 1994, pp. 1124-1129.

Lee, C.K., Natick Soldier Center, Private Communication, 1998.

Lighthill, J., "Fundamentals Concerning Wave Loading on Offshore Structures," *Journal of Fluid Mechanics*, Vol. 173, 1986, pp. 667-681.

Lingard, J.S., "The Aerodynamics of Parachutes During the Inflation Process," Ph.D. thesis, Department of Aeronautical Engineering, University of Bristol, England, October 1978.

Macha, J.M., and Buffington, R.J., "An Experimental Investigation of Wall-Interference Effects for Parachutes in Closed Wind Tunnels," Sandia Report, SAND89-1485, Sept., 1989.

McVey, D.F., and Wolf, D.F., "Analysis of Deployment and Inflation of Large Ribbon Parachutes," *Journal of Aircraft*, Vol. 11, No. 2, 1974, pp. 96-103.

Müller, W., "Parachutes for Aircraft," National Advisory Committee for Aeronautics, Technical Memorandums, No. 450, October 28, 1927.

Noca, F., "On the Evaluation of Instantaneous Fluid-Dynamic Forces on a Bluff Body," GALCIT Report FM96-5, Aug. 12, 1996.

Noca, F., Shiels, D., and Jeon, D., "A Comparison of Methods for Evaluating Time-Dependent Fluid Dynamic Forces on Bodies, Using Only Velocity Fields and Their Derivatives," *Journal of Fluids and Structures*, Vol. 13, 1999, pp. 551-578.

O'Hara, F., "Notes on the Opening Behavior and the Opening Forces of Parachutes," *Journal of the Royal Aeronautical Society*, Vol. 53, Nov. 1949, pp. 1053-1062.

Panton, R.L., Incompressible Flow, Wiley and Sons, 1996.

Payne, P.R., "A New Look at Parachute Opening Dynamics," *Aeronautical Journal*, Feb. 1973, pp. 85-93.

Pepper, W.B. and Reed, J.F., "Parametric Study of Parachute Pressure Distribution by Wind Tunnel Testing," *Journal of Aircraft*, Vol. 13, No. 11, 1976, pp. 895-900.

Peterson, C.W., Strickland, J.H., and Higuchi, H., "The Fluid Dynamics of Parachute Inflation," *Annual Review of Mechanics*, Vol. 28, pp. 361-387.

Purvis, J.W., "Theoretical Analysis of Parachute Inflation Including Fluid Kinetics," *Journal of Aircraft*, Vol. 19, No. 4, 1982, pp. 290-296.

Raffel, M., Willert, C.E., and Kompenhans, J., Particle Image Velocimetry – A Practical Guide, Springer, 1998.

Reddy, K.R., "Unsteady Vortex Flow Past an Inflating, Decelerating Wedge," *Journal of Aircraft*, Vol. 11, No. 7, July, 1974, pp. 427-429.

Roberts, B.W., "Aerodynamic Inflation of Shell Type, Parachute Structures," *Journal of Aircraft*, Vol. 11, No. 7, 1974, pp. 390-397.

Roberts, B.W., "Drag and Pressure Distribution on a Family of Porous, Slotted Disks," *Journal of Aircraft*, Vol. 17, No. 6, 1980, pp. 393-401.

Sahu, J., Edge, H., Heavey, K., Stein, K., and Benney, R., "Comparison of Numerical Flow Field Predictions for Army Airdrop Systems," 15th CEAS/AIAA Aerodynamic Deceleration Systems Technology Conference, Toulouse, France, June 8-11, 1999, AIAA Paper 99-1715.

Sarpkaya, T., "Methods of Analysis for Flow Around Parachute Canopies," 11th AIAA Aerodynamic Deceleration Systems Technology Conference, San Diego, California, Apr. 9-11, 1991, AIAA Paper 91-0825.

Stein, K.R., "Simulation and Modeling Techniques for Parachute Fluid-Structure Interactions," Ph.D. dissertation, Department of Aerospace Engineering, University of Minnesota, December 1999.

Stein, K., Benney, R., Tezduyar, T., Kalro, V., Leonard, J., and Accorsi, M., "3-D Computation of Parachute Fluid-Structure Interactions: Performance and Control," 15th CEAS/AIAA Aerodynamic Deceleration Systems Technology Conference, Toulouse, France, June 8-11, 1999, AIAA Paper 99-1714.

Stein, K., Benney, R., Kalro, V., Tezduyar, T.E., Leonard, J., and Accorsi, M., "Parachute Fluid-Structure Interactions: 3-D Computation," *Computer Methods in Applied Mechanics and Engineering*, Vol. 190, 2000, pp. 373-386.

Strickland, J.H., "Prediction Method for Unsteady Axisymmetric Flow Over Parachutes," Journal of Aircraft, Vol. 31, No. 3, 1994, pp. 637-643.

Taylor, G.I., "On the Shape of Parachutes," The Scientific Papers of Sir Geoffrey Ingram Taylor, Volume III, Aerodynamics and The Mechanics of Projectiles and Explosions, edit. Batchelor, G.K., 1963, pp. 26-37.

Taylor, J.R., An Introduction to Error Analysis, 2nd Ed., University Science Books, 1997.

Willert, C.E., and Gharib, M., "Digital Particle Image Velocimetry", *Experiments in Fluids*, Vol. 10, 1991, pp. 181-193.

Wolf, D., "A Simplified Dynamic Model of Parachute Inflation," *Journal of Aircraft*, Vol. 11, No. 1, 1974, pp. 28-33.

Wolf, D., "Parachute Opening Shock," 15th CEAS/AIAA Aerodynamic Deceleration Systems Technology Conference, Toulouse, France, June 8-11, 1999, AIAA Paper 99-1702.

Yavuz, T., "Determining and Accounting for a Parachute Virtual Mass," *Journal of Aircraft*, Vol. 26, No. 5, 1989, pp. 432-437.